Field Emission and Wettability Properties of Porous Silicon Nanowires and Its rGO Composites

A thesis submitted towards partial fulfillment of the requirements for the degree of

Master of Technology in Nanoscience and Technology

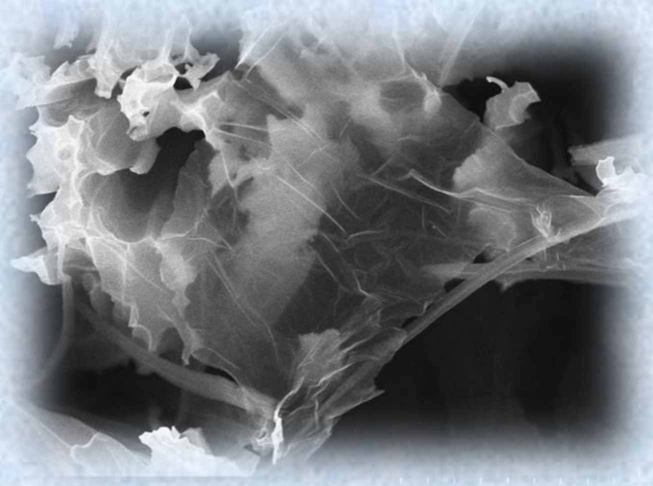

Submitted by

ANKITA CHANDRA
ROLL NO.: M4NST19006

Under the guidance of

Prof. Kalyan Kumar Chattopadhyay
SCHOOL OF MATERIALS SCIENCE AND NANOTECHNOLOGY
Jadavpur University

Course affiliated to

Faculty of Engineering and Technology
Jadavpur University
Kolkata-700032,
India
2019

M.Tech. (Nano Science and Technology)
course affiliated to
Faculty of Engineering and Technology
Jadavpur University
Kolkata, India

Certificate of Recommendation

This is to certify that the thesis entitled "**Field Emission and Wettability Properties of Silicon Nanowires and Its rGO Composites**" has been carried out under our guidance by **Ankita Chandra** during the academic session **2018–19** in partial fulfilment of requirement for the award of degree of **Master of Technology in Nano Science and Technology at School of Material Science and Nanotechnology**, Jadavpur University, Kolkata- 700032. In our opinion the work fulfils the requirement for which it is submitted.

It is further certified that the materials obtained from other sources have been acknowledged in the thesis.

THESIS ADVISOR
Prof. Kalyan Kumar Chattopadhyay
School of Materials Science and Nanotechnology
Jadavpur University,
Kolkata-700 032

DIRECTOR
School of Materials Science and Nanotechnology
Jadavpur University,
Kolkata-700 032

DEAN
Faculty Council of Interdisciplinary Studies, Law and Management
Jadavpur University,
Kolkata-700 032

M.Tech. (Nano Science and Technology)
course affiliated to
Faculty of Engineering and Technology
Jadavpur University
Kolkata, India

Certificate of Approval **

The forgoing thesis is hereby approved as credible study of an engineering subject carried out and represented in a manner satisfactorily to warrant its acceptance as a prerequisite to the degree for which it has been submitted.

It is to be understood that by this approval the undersigned does not necessarily endorse or approve any statement made, opinion expressed or conclusion drawn therein but approved the thesis only for the purpose for which it has been submitted.

Final Examiners for

Evaluation of thesis **Signature of the Examiners**

1.____________________________

2.____________________________

3.____________________________

Date _________________

** Only in case the thesis is approved.

DECLARATION OF ORIGINALITY AND COMPLIANCE OF ACADEMIC ETHICS

I hereby declare that this thesis contains literature survey and original research work by the undersigned candidate, as part of his **Master of Technology** (Nano Science and Technology) studies during academic session 2018-2019.

All information in this document has been obtained and presented in accordance with academic rules and ethical conduct.

I also declare that, as required by this rules and conduct, I have fully cited and referred all material and results that are not original to this work.

NAME:	ANKITA CHANDRA
ROLL NUMBER:	M4NST19006
THESIS TITLE:	**Field Emission and Wettability Properties of Porous Silicon Nanowires and Its rGO Composites**

Dedicated to my beloved Parents
for their endless love, support and
encouragement

Acknowledgement

The work described in this thesis entitled "**Field Emission and Wettability Properties of Porous Silicon Nanowires and Its rGO Composites**" was started in the Thin Film & Nanoscience Laboratory, Jadavpur University in June 2017 and would not have been what it is today without the support and advice of others. First of all I would like to take this oppurtunity to sincerely express my earnest gratitude to my thesis advisor, Prof. Kalyan Kumar Chattopadhyay for giving me the opportunity to work under his esteemed guidance leading to thesis submission and motivating me thoroughly throughout my scientific and research endeavours. I am grateful to you for guiding me during the entire course of research work with your valuable suggestions. Thank you also for the amicable environment conducive to extensive research work at Thin Film and Nanoscience Lab, in which you have welcomed me.

I am also indebted to Dr. C.K. Ghosh, Prof. G.C. Das, Dr. M.G. Chowdhury, and Dr. S. Sarkar for their valuable suggestions and constructive criticism during the course of my M. Tech program. Their enthusiasm provided me a helpful and effective way of learning which in turn inspired me to follow the research project with great vigour.

I extend my heartiest thanks to Biswajit Da, Supratim Da, Madhupriya Di, Antika Di ,Suvra Di, Souvik Da , Dimitra Di , Brahmi Di ,Karam Da ,Rituparna Di, Missi Di and Nripen Da for extending their helping hands to me and making my project a really fulfilling experience. I owe special gratitude to my parents, friends and laboratory peers Ankit, Pulok, Pratik, Sumit, Debnath and Sourav for their constant support.

Finally, I owe my heartiest gratitude to Shrabani Di, research fellow at Thin Film and Nanoscience Lab for providing me her immense support with rich scientific ideas and encouragement to work hard. All these provided me great support during my project, which I do not think I would have completed it otherwise.

Abstract

The work is on metal assisted chemically etched at 60 °C porous silicon nanowires. The etching time is varied accordingly. Important characterizations are carried out to confirm its phase and morphology. FESEM image signifies variation of length and diameter as the etching time increases. Field emission property is studied. It is observed that SiNW 60 is optimum one for good field emitter considering all properties. SiNW 80 gives good field emission current density at high applied field whereas turn on, enhancement factor are not improved. To enhance the field emission property of SiNW 80, rGO layer is deposited on SiNW 80. It improves the current density as well as turn on, threshold and enhancement factor etc. as rGO increases number of emitting edges. There are several factors can be responsible for such activity like surface roughness, enhancement of emitting edges, porosity etc. ANSYS Maxwell simulation is carried out which completely agrees with experimental results. Wettability properties are measured for all the samples which correlate with the field emission characteristics. As it is observed that CA increases in rGO-SiNW_H80 composite, there is increment of surface roughness as explained from Cassie-Baxter model which initiates to have more emitting edges for good field emission property. Heat treated porous nanowires' wettability is compared with room temperature synthesized nanowires'. There is a significant transformation from hydrophobic (room temp) to hydrophilic (heat treated). Porosity, length, sharp tip, bundling effect etc. are important factor for such change in properties.

Table of Contents

Chapter 1

Introduction

1.1 Introduction to Nanotechnology

The prefix ‘nano’ is derived from the Greek word for dwarf. One nanometre (nm) is equal to one-billionth of a metre, 10^{-9}m.[1] A human hair is approximately 80,000nm wide, and a red blood cell approximately 7000nm wide. Atoms are below a nanometre in size, whereas many molecules, including some proteins, range from a nanometre upwards.

Nanoscience and technology is the manipulation of the materials at the molecular or atomic level in order to produce the novel materials and devices with new enhanced and extraordinary properties. However, nanotechnology is not a new discipline. It is rather the merging of multiple scientific disciplines (biology, physics, chemistry, medicine and engineering) and the combination of knowledge to tailor materials at the nano scale approximately in the range of 1-100 nanometers (10^{-9} m).

The conceptual underpinnings of nanotechnologies were first laid out in 1959 by the physicist Richard Feynman, in his lecture ‘There’s plenty of room at the bottom’ (Feynman 1959). Feynman explored the possibility of manipulating material at the scale of individual atoms and molecules, imagining the whole of the Encyclopedia Britannica written on the head of a pin and foreseeing the increasing ability to examine and control matter at the nanoscale.[2]

The term ‘nanotechnology’ was not used until 1974, when Norio Taniguchi, a researcher at the University of Tokyo, Japan used it to refer to the ability to engineer materials precisely at the nanometer level.[3] The primary driving force for miniaturization at that time came from the electronics industry, which aimed to develop tools to create smaller (and therefore faster and more complex) electronic devices on silicon chips. Indeed, at IBM in the USA a technique called electron beam lithography was used to create nanostructures and devices as small as 40–70nm in the early 1970s.[4].

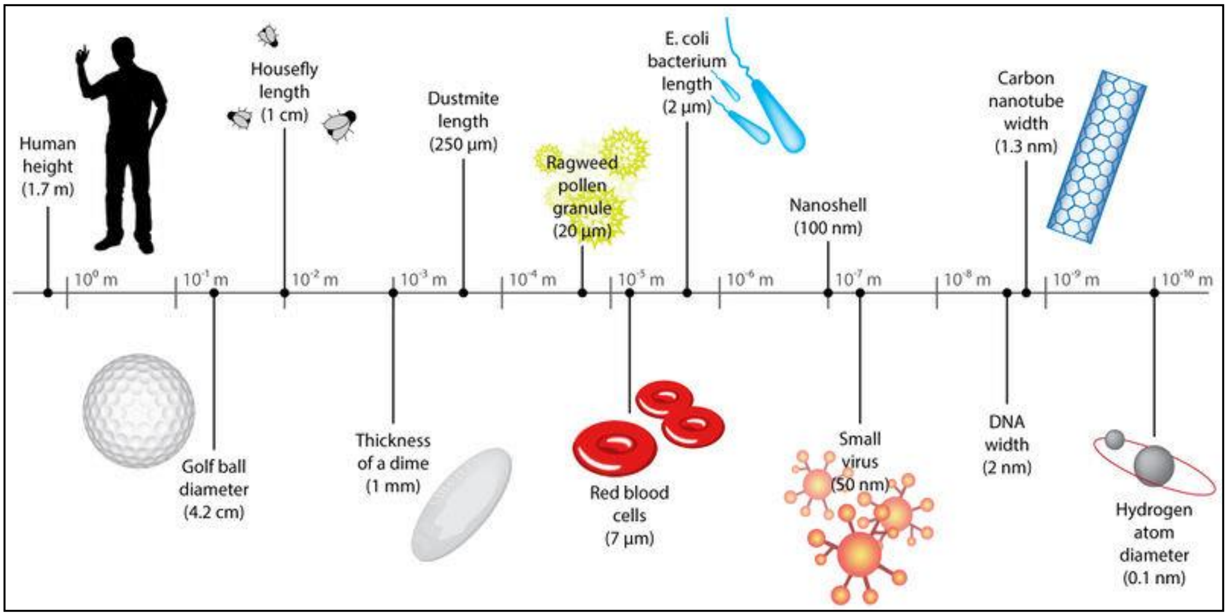

Figure 1. 1 Size comparison of materials from bulk to nanoscale

1.2 What makes ‘nano’ special?

There are various reasons why nanoscience and nanotechnologies are so promising in materials, engineering and related sciences. The overall behavior of bulk crystalline materials changes when the dimensions are reduced to the nanoscale.[5-6]

First, at the nanometre scale, the properties of matter change. This is a direct consequence of the small size of nanomaterials, physically explained as quantum effects. The consequence is that a material when in a nano-sized form can assume properties which are very different from those when the same material is in a bulk form. Bulk materials possess continuous (macroscopic) physical properties, the value of such properties which is obtained represents an average value based on the behavior of billions and billions of molecules. The same applies to micron-sized materials (e.g. a grain of sand). But when particles assume nanodimensions, the principles of classical physics are no longer capable of describing their behaviour at these dimensions, the principles of quantum mechanics are involved. The same material (e.g. gold) at the nanoscale can have properties (e.g. optical, mechanical and electrical) which are very different from (and even opposite to) the properties the material has at the macroscale (bulk). Properties like electrical conductivity, optical property, and mechanical strength change when the nanoscale level is reached: the same metal can become a semiconductor or an insulator at the nanoscale level. In other words, the properties of materials can be size-dependent.

Finally, when a bulk material is subdivided into an

ensemble of individual nanomaterials, the total volume remains the same, but the collective surface area is greatly increased. Nanomaterials have an increased surface-to-volume ratio compared to corresponding bulk materials. This has important consequences for all those processes that occur at the surface of a material, such as catalysis and detection.

1.3 History of Nanotechnology

Although nanotechnology is a relatively recent development in scientific research, the development of its central concepts happened over a longer period of time. Researchers have supported by the development of new instruments that allow the investigation of nanomaterial properties with an atomic level resolution and the time line of these inventions are listed below.[7]

1857	•Michael Faraday discovered **colloidal “ruby” gold**, demonstrating that nanostructured gold.
1936	•Erwin Müller, working at Siemens Research Laboratory, invented the **Field Emission Microscope.**
1950	•Victor La Mer and Robert Dinegar developed the **theory and a process for growing monodisperse colloidal materials**.
1951	•Erwin Müller pioneered the **field ion microscope**, a means to image the arrangement of atoms at the surface of a sharp metal tip
1956	•Arthur von Hippel introduced the term—**“molecular engineering”**.
1958	•Jack Kilby of Texas Instruments originated the concept of, designed, and built the first **integrated circuit**
1959	•Richard Feynman gave the first lecture on technology and engineering at the atomic scale, "**There's Plenty of Room at the Bottom**"
1965	•**Moore’s Law** was introduced.
1981	•Gerd Binnig and Heinrich Rohrer at IBM’s Zurich lab invented the **scanning tunneling microscope**
1985	•Discovery of **Buckminster fullerene**(C_{60}). •Louis Brus discovered **colloidal semiconductor nanocrystals (quantum dots)**
1986	•**Atomic Force Microscope** was discovered.
1991	•Sumio Iijima was credited with discovering the **carbon nanotube (CNT).**
1993	•A **method for controlled synthesis of nanocrystals** was discovered.

- **1998** The **Interagency Working Group on Nanotechnology** (IWGN) was formed.
- **1999** **Dip-pen nanolithography** was invented.
- **2000** The National Nanotechnology Initiative (NNI) was launched.
- **2005** Theories for **DNA-based computation** and "**algorithmic self-assembly**" in which computations are embedded in the process of nanocrystal growth was developed.
- **2007** Arthur von Hippel introduced the term—**"molecular engineering"**.
- **2008** The first official **NNI Strategy for Nanotechnology-Related Environmental, Health, and Safety (EHS) Research** was published.
- **2009** **DNA-like robotic nanoscale assembly devices** was created.
- **2010** **Graphene** was discovered.
- **2014** The NNI releases the **updated 2014 Strategic Plan.**

1.4 Synthesis of Nanomaterials

There are different ways of manipulating matter at the nanoscale. The two most are top-down and bottom-up methods. [8,9]

The top-down approach revolves around fabrication via etching away bulk material to achieve the required smaller structural architectures and this is generally achieved by lithographic processes . This process could be likened to sculpting a block of stone to the required image. In contrast, the bottom-up approach involves the structures being crafted atom by atom or molecule by molecule through covalent or supramolecular interactions in a similar manner to how a house is built brick by brick.

Both approaches play very important role in modern industry and most likely in nanotechnology as well. There are advantages and disadvantages in both approaches. Attrition or Milling is a typical top down method in making nano particles, whereas the colloidal dispersion is a good example of bottom up approach in the synthesis of nano particles.[10]

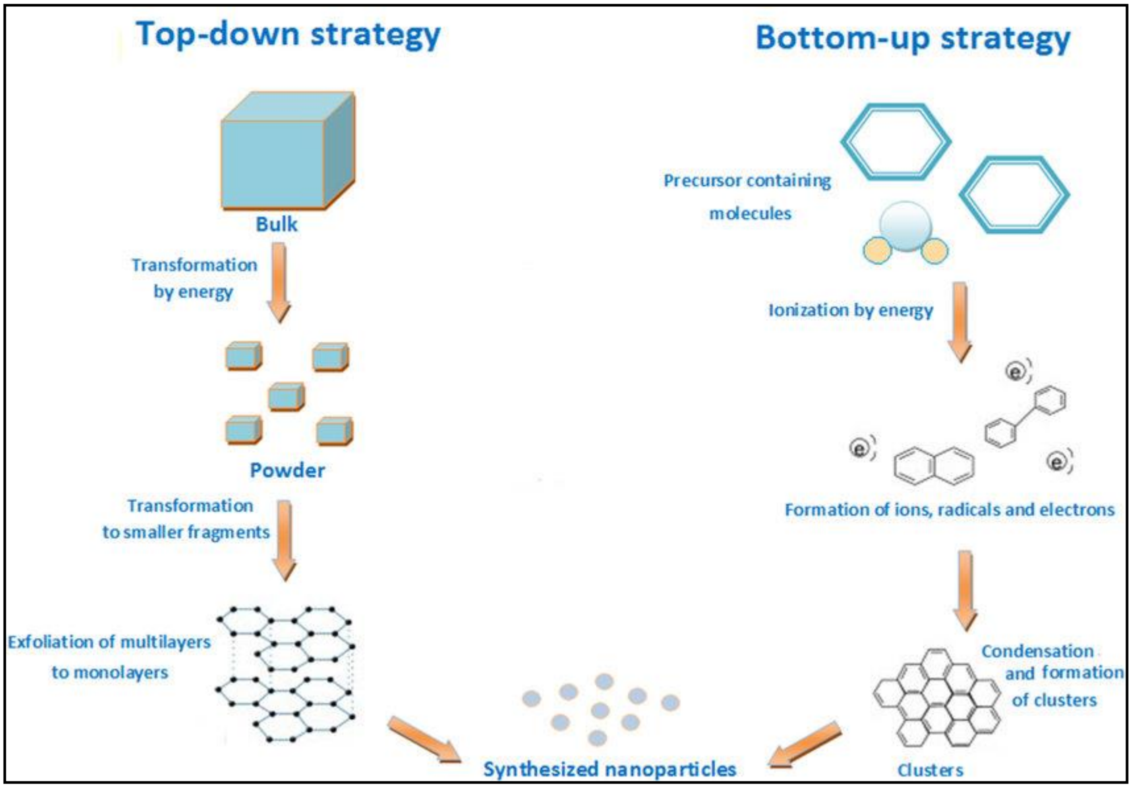

Figure1. 2 Top-Down and Bottom Up Approach

Self-assembly:

One bottom-up method is nature's way; “self-assembly”.[11] Self-organizing processes are common throughout nature and involve components from the molecular (e.g. protein folding) to the planetary scale (e.g. weather systems) and even beyond (e.g. galaxies). The key to using self-assembly as a controlled and directed fabrication process lies in designing the components that are required to self-assemble into desired patterns and functions. Self-assembly reflects information coded - as shape, surface properties, charge, polarizability, magnetic dipole, mass etc. in individual components; these characteristics determine the interactions among them.

1.5 Types of Nanomaterials

Nanomaterials are mostly classified based on five factors: nanoparticle geometry, morphology, composition, uniformity, and agglomeration. Based on nanoparticle geometry, nanomaterials are classified as 0D,1D, 2D, or 3D .[12,13]

- **0D nanomaterials** have all three dimensions of particulate in nanometer scale and are generally referred to as equiaxed nanoparticles, nanogranules, or nanocrystals. Fullerenes, dendrimers, and quantum dots are examples of 3D nanomaterials.
- **1D nanomaterials** have one dimension of particulate in the nanometer scale and are generally referred to as nanolayers, nanoclays, nanosheets, nanoflakes, or nanoplatelets. Graphite, clay, and silicate nanoplatelets are examples of 1D nanomaterials. Figure 1.2 shows some of the different kinds of nanomaterials and platelets.
- **2D nanomaterials** have two dimensions of particulate in the nanometer scale and a third dimension could be in micro- or macroscale. These materials form an elongated structure and are generally referred to as nanotubes, nanofibers, nanorods, or whiskers. CNTs and carbon nanofibers (CNFs) are good examples of 2D nanomaterials.
- **3D nanomaterials** are materials that are not confined to the nanoscale in any dimension. This class can contain bulk powders, dispersions of nanoparticles, bundles of nanowires, and nanotubes as well as multi-nanolayers.

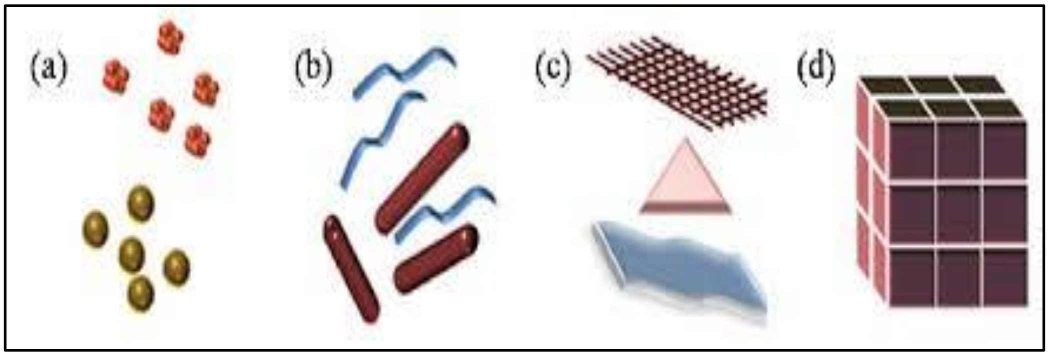

Figure 1. 3 : Classification of Nanomaterials (a) 0D spheres and clusters, (b) 1D nanofibers, wires, and rods, (c) 2D films, plates, and networks, (d) 3D nanomaterials.

1.6 Applications of Nanotechnology

The applications of nanotechnology are widespread and have far reaching impact. Nanotechnology will eventually provide us with the ability to design custom-made materials and products with new enhanced properties, new nanoelectronics components, new types of “smart” medicines and sensors, and even interfaces between electronics and biological systems.

On nanoscale, some physical and chemical material properties can differ significantly from those of the bulk structured materials of the same composition. A considerable increase in surface-to-volume ratio is associated with the reduction in material size to the nanoscale, often having a prominent effect on material properties and performance.

1.6.1 Electronics and IT application

Much of the miniaturization of computer chips to date has involved nanoscience and nanotechnologies, and this is expected to continue in the short and medium term. The storage of data, using optical or magnetic properties to create memory, will also depend on advances in nanoscience and nanotechnologies. [14-17]

- **Displays:** The huge market for large area, high brightness, flat-panel displays, as used in television screens and computer monitors, is driving the development of some nanomaterials. Nanocrystalline zinc selenide, zinc sulphide, cadmium sulphide and lead telluride synthesized by sol–gel techniques are candidates for the next generation of light-emitting phosphors. CNTs are being investigated for low voltage field-emission displays; their strength, sharpness, conductivity and inertness make them potentially very efficient and long-lasting emitters.
- **P-N junction diodes:** The most important application of thin film nanostructure materials is efficient diode formation of the p-n junction diode. The continued decrease in device dimensions has followed the well-known Moore's law predicted in 1965.
- **Memory Storage:** Electronic memory plans in the past have to a great extent depended on the arrangement of transistors. On the other hand, research into crossbar switch based gadgets have offered an option utilizing reconfigurable interconnections in the middle of vertical and flat wiring shows to make ultrahigh thickness memories
- **Optoelectronics:** The other crucial element of the IT revolution, optoelectronics, relates to devices that rely on converting electrical signals to and from light for data transmission, for displays for optical-based sensing and, in the future, for optical-based computing.
- **Nanosensors:** Nanotechnologies play several important roles in developing sensor technology. The ideal sensor will be minimally invasive and therefore as small as possible. This includes the power supply, the sensing action, whereby the detected property is converted into an electrical signal, and the transmission of the sensing signal to a remote detector. Combining these actions into a device that is smaller than 1mm2 will certainly require nanofabrication techniques, similar to those employed by the IT industry.

- **Quantum Computers:** It is a new approach in the industry of computer. It has quantum bit memory which is called qubit for several computations at the same time. It improves the facility of the older system. Quantum computing will start to provide solutions to complex problems that are difficult or impossible to solve by conventional computing.

1.6.2 In Medical Science:

It has several applications in biomedical nanotechnology, nano biotechnology, and nanomedicine. The size of the nanomaterial is similar to that of most biological molecules and structures, therefore nanomaterial can be useful in vivo and in vitro medical research and applications. The integration of nanotechnology with biology has resulted in development of diagnostic devices, contrast agents, analytical tools, physical therapy applications and drug delivery vehicles.[18-22]

- **Medical Imaging:** Non-invasive imaging techniques have had a major impact in medicine over the past 25 years or so. Nanotechnologies already afford the possibility of intracellular imaging through attachment of quantum dots or synthetic chromophores to selected molecules, for example proteins, or by the incorporation of naturally occurring fluorescent proteins which, with optical techniques such as confocal microscopy and correlation imaging, allow intracellular biochemical processes to be investigated directly.
- **Drug delivery:** There is enormous potential for nanotechnology to be applied to gene and drug delivery. The vehicle might be a functionalised nanoparticle capable of targeting specific diseased cells, which contains both therapeutic agents that are released into the cell and an on-board sensor that regulates the release.
- **Implants and prosthetics:** Some nanomaterials such as nanocrystalline ceramics have certain properties such as hardness, wear resistance and biocompatibility that may make them

of use as implants in the long term. The development of nanoelectronic systems with high detector densities and data processing capability might allow the development of an artificial retina or cochlea. Important progress is already being made in this area, but many issues must be resolved before they can become viable treatments. Similarly, the introduction of nanoelectronics will allow biological neural processing to be investigated at much enhanced spatial resolution.

1.6.3 Environment applications:

- **Catalysts:** In general, nanoparticles have a high surface area and hence provide higher catalytic activity. It is possible to synthesise metal nanoparticles in solution in the presence of a surfactant to form highly ordered monodisperse films of the catalyst nanoparticles on a surface. This allows more uniformity in the size and chemical structure of the catalyst, which in turn leads togreater catalytic activity and the production of fewer byproducts. This will be particularly beneficial if it reduces the demand for platinum-group metals, whose use in standard catalytic units is starting to emerge as a problem, given the limited availability of these metals.
- **Filtration:** Nano-engineered membranes could potentially lead to more energy-efficient water purification processes, notably in desalination by reverse osmosis. They would use fixed nanoparticles, and are therefore distinct from applications that propose to use free nanoparticles.

1.6.4 Energy Applications:

The most advanced nanotechnology tasks related to power are: storage, transformation, manufacturing developments by reducing materials and process rates, power saving (by better heat insulating material for example), and improved alternative power.[23-24]

- **Fuel Cells:** Engineered surfaces are essential in fuel cells, where the external surface properties and the pore structure affect performance. The hydrogen used as the immediate fuel in fuel cells may be generated from hydrocarbons by catalytic reforming, usually in a reactor module associated directly with the fuel cell. The potential use of nano-engineered membranes to intensify catalytic processes could enable higher-efficiency, small-scale fuel cells. These could act as distributed sources of electrical power. It may eventually be possible to produce hydrogen locally from sources other than hydrocarbons, which are the feedstocks of current attention.
- **Batteries:** With the growth in portable electronic equipment (mobile phones, navigation devices, laptop computers, remote sensors), there is great demand for lightweight, high-energy density batteries. Nanocrystalline materials synthesized by sol–gel techniques are candidates for separator plates in batteries because of their foam-like (aerogel) structure, which can hold considerably more energy than conventional ones. Nickel–metal hydride batteries made of nanocrystalline nickel and metal hydrides are envisioned to require less frequent recharging and to last longer because of their large grain boundary (surface) area.
- **Solar cell applications:** Most solar cells are now fabricated on Si wafers or glass substrates. The biggest issue for commercialized solar cells is their high price. In addition, due to their fabrication on the Si wafer, the cells are rigid and heavy while being fragile. While they are recognized as one of the most crucial alternative sources of energy, such limitations have prevented wider application of solar cells.

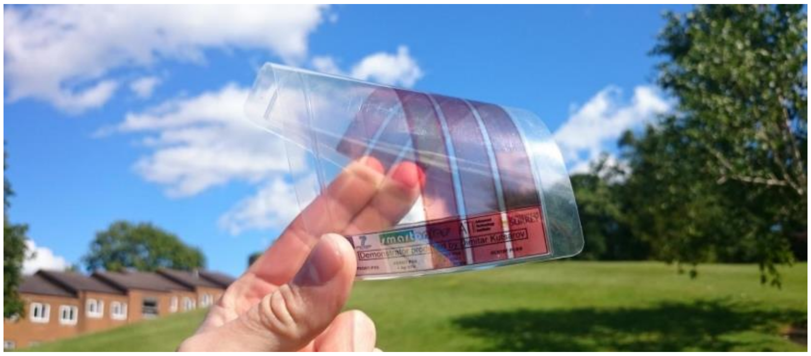

Figure1. 4 Flexible and Transparent Graphene Based Solar Cells

1.6.5 Consumer Goods:

Nanotechnology has a great impact in the field of consumer goods from easy to clean to scratch resistant surfaces. Modern textiles are wrinkle resistant and strain repellent. Clothes have become smart and embedded with wearable electronics. In the field of cosmetics also, nanotechnology has a huge effect.[25-26]

- **Foods:** Nanotechnology is having an impact on several aspects of food science, from how food is grown to how it is packaged. Companies are developing nanomaterials that will make a difference not only in the taste of food, but also in food safety, and the health benefits that food delivers.
- **Textiles:** The incorporation of engineered nano fiber in clothes makes the clothes water and strain repellent and wrinkle free. Nano technological finished textiles can be washed less frequently at lower temperatures.
- **Cosmetics:** Mainly sunscreen cosmetics are made of nanoparticles. Traditional chemicals used in sunscreens have poor long-term stability. Sunscreen based on mineral nanoparticles such as titanium oxide offers more UV protection.
- **Sports:** Nanotechnology has applications in the field of sports like soccer, football, baseball etc. Baseball bats are made of carbon nanotubes which reinforce the resin and also improve

its performance by making it lighter. Other items such as sport towels, yoga mats, exercise mats use antimicrobial nanotechnology to prevent illnesses caused by bacteria such as Methicillin-resistant Staphylococcus aureus (commonly known as MRSA).

- **Agriculture:** Applications of nanotechnology have the potential to change the entire agriculture sector and food industry from production to conservation, processing, packaging, transportation, and even waste treatment.

1.6.6 Heavy Industries:

- **Aerospace:** Nanotechnology may hold the key to making space-flight more practical. Advancements in nanomaterials make lightweight spacecraft and a cable for the space elevator possible. By significantly reducing the amount of rocket fuel required, these advances could lower the cost of reaching orbit and traveling in space.[27-28]
- **Construction:** Nanotechnology can possibly make development quicker, less expensive, more secure, and more changed. Computerization of nanotechnology development can take into account the formation of structures from cutting edge homes to enormous high rises substantially more rapidly and at much lower expense.
- **Vehicle manufacturers:** Much like aviation, lighter and stronger materials will be valuable for making vehicles that are both quicker and more secure. Burning motors will likewise profit from parts that are all the more hard-wearing and more high temperature safe.

References:

[1] Kai Nordlund , Introduction to Nanoscience, 2005.

[2] Richard P. Feynman, “There's plenty of room at the bottom,” California Institute of Technology Journal of Engineering and Science 4(2), 23–36 (1960).

[3] N. Taniguchi, “On the Basic Concept of ‘Nano-Technology’ ”, Proc. Intl. Conf. Prod. Eng. Tokyo, Part II, Japan Society of Precision Engineering, 1974.

[4] G. Binnig, H. Rohrer, C. Gerber, and E. Weibel, Phys. Rev. Lett., 1982, 49, 57.

[5] Charles P. Poole, Jr. and Frank J. Owens , Introduction To Nanotechnology

[6] Guozhong Cao, Nanostructures and Nanomaterials: Synthesis, Properties and Applications

[7] National Nanotechnology Initiative, Environmental, Health, and Safety Research Strategy, National Science and Technology Council Committee on Technology, 2011.

[8] Guozhong Cao, Ying Wang; Nanostructures and nanomaterials - synthesis, properties and applications, 2011.

[9] C.N. Chinthamani Nagesa Ramachandra Rao, P.john Thomas, G.U. kulkarni, Nano crystal: synthesis, properties and applications, 2007.

[10] Parvez Iqbal, Jon A. Preece, and Paula M. Mendes, Nanotechnology: “The Top-Down and Bottom-Up Approaches”, Supramolecular Chemistry: From Molecules to Nanomaterials, 2012

[11] Shimizu, T. ed., Self-assembled nanomaterials II: Nanotubes (Vol. 220). Springer.(2008)

[12] Jitendra N. Tiwari, Rajanish N. Tiwari, Kwang S. Kim, “Zero-dimensional, onedimensional, two-dimensional and three-dimensional nanostructured materials for advanced electrochemical energy devices”, Progress in Materials Science, Volume 57, Issue 4, (2012), 724-803.

[13] B. Bhushan, Springer Handbook of Nanotechnology, Springer-Verlag, Heidelberg, Germany, 2004.

[14] Xiang, Jie; Lu, Wei; Hu, Yongjie; Wu, Yue; Yan; Hao & Lieber, Charles M. (2006). “Ge/Si nanowire heterostructures as high performance field-effect transistors". Nature 441 (7092): (2006) 489–493.

[15] Jong-Hyun Ahn, Byung Hee Hong "Graphene for displays that bend" Nature Nanotechnology volume9 (2014), 737–738

[16] P. Zijlstra, J.W.M. Chon, and M. Gu, “Five-dimensional optical recording mediated by surface plasmons in gold nano-rods,” Nature 459, (2009) 410-413.

[17] Qing Hua Wang, Kourosh Kalantar-Zadeh, Andras Kis , Jonathan N. Coleman, Michael S. Strano "Electronics and optoelectronics of two-dimensional transition metal dichalcogenides", Nature Nanotechnology volume7, (2012) 699–712

[18] Frietas RA Jr, "Current status of nanomedicine and medical nanorobotics". J Comut Ther Nanosci.(2005);2:1–25.

[19] Boisseau P, Loubaton B "Nanomedicine, nanotechnology in medicine". Comptes Rendus Physique 12 (2011): 620-636.

[20] Minchin R "Nanomedicine: Sizing Up Targets With Nanoparticles". Nat Nanotechnology 3(2008): 12-13.

[21] Wang, Xu, et al. "Application of nanotechnology in cancer therapy and imaging." CA: a cancer journal for clinicians 58.2 (2008): 97-110.

[22] Nie S, Xing Y, Kim GJ, Simons JW "Nanotechnology applications in cancer." Annu Rev Biomed Eng 9(2007): 257-288.

[23] Lee G, Park J, Sung Y, Chung K, Cho W and Kim D "Enhanced cycling performance of an Fe0/Fe3O4 nanocomposite electrode for lithium-ion batteries" Nanotechnology Volume 20 (2009), 295205

[24] Nayfeh, “Enhancement of polycrystalline silicon solar cells using ultrathin films of silicon nanoparticle” Applied Physics, Volume 91,Issue 6, Article 063107, August 6, (2007).

[25] Duncan, Timothy V. "Applications of nanotechnology in food packaging and food safety: Barrier materials, antimicrobials and sensors." Journal Of Colloid And Interface Science 363.1 (2011): 1-24.

[26] Silpa Raj, Shoma Jose, U. S. Sumod, and M. Sabitha" Nanotechnology in cosmetics: Opportunities and challenges" J Pharm Bioallied Sci. 2012 Jul-Sep; 4(3): 186–193

[27] Zhu, W., P. J. M. Bartos, and A. Porro. "Application of nanotechnology in construction." Materials and Structures 37.9 (2004): 649-658

[28] Nassar, Nashaat N., Azfar Hassan, and Pedro Pereira-Almao. "Application of nanotechnology for heavy oil upgrading: Catalytic steam gasification/cracking of asphaltenes." Energy & Fuels 25.4 (2011): 1566-1570.

Chapter 2

Introduction to Silicon Nanowires, Field Emission and Wettability

2.1 Silicon Nanowire (SiNW)

Silicon nanowires, also referred to as SiNWs, are quasi one-dimensional (1D) structures with a diameter of less than 100nm. Silicon nanowires have very small diameter resulting in a large surface to volume ratio giving rise to many unique properties.[1]

Silicon nanowires are considered as one of the popular nanomaterials due to their exceptional electrical and mechanical properties.[2] They are semiconducting nanowires and their conductivity is controlled by the field-effect action .[3] For this reason, siliconnanowires can be used probably for the next generation of field-effect transistors and advanced sensors.

SiNWs have very small diameter which results in a large surface to volume ratio. Due to the high surface to volume silicon ratio and unique quasi one-dimensional electronic structure, silicon nanowire based devices have properties that can outperform their traditional counterparts in many ways. These properties of silicon nanowires have been exploited in many ways in electronic devices. Nanowires are an excellent choice for the ultimate silicon metal insulator semiconductor (MIS) devices because when a gate is wrapped around the nanowire, the optimum control of the nanowire potential by the gate potential is ensured.[4] The junctionless transistor and tunnel field effect transistors are two prominent examples where silicon nanowires are being implemented. Additionally, new types of functionalities can be exploited by making the devices reconfigurable. Also the field of energy generation and storage can benefit from the quasi 1D structure. In the solar cells the silicon nanowires allow to more efficiently collect the incoming solar radiation whereby in Li-ion batteries the structure allows for volume expansion. [5-6]

2.2 SiNWs Synthesis Techniques

A large number of techniques exist to fabricate silicon nanowires. These can be classified into bottom-up and top-down fabrication techniques. In top-down fabrication, lithography is used to define the fabricated structure that is then transferred from the photo-resist to the substrate by etching or a similar way of structuring the already available material. In the bottom-up approach, the material is added to the substrate in a self-organized way.

The bottom–up approach includes processes like vapor-liquid-solid (VLS) and oxide-assisted growth (OAG) and photolithography or e-beam lithography. The bottom–up method involves the synthesis of the SiNWs from a mass of silicon wafer with the reaction being metal catalyzed, while top–down technique begins from a bulk silicon wafer and trims down to the preferred and required size and shape of SiNWs through a lithographic mechanism.

2.2.1 Vapor Liquid Solid (VLS) Growth Mechanism.

The most prominent nanowire synthesis method is named the vapor liquid solid (VLS) growth mechanism. Silicon nanowire synthesis via VLS was first reported in 1964 using silicon substrate integrated with liquid Au droplet. In VLS, there is a deposition of metal-catalyzed (Au, Fe, Pt, Al, etc.) on the silicon wafer and then the SiNWs growth is augmented either by chemical vapor deposition (CVD) technique.[7] Essentially, silicon wafer coated with metal catalysts are positioned at the middle of a tube furnace and initiated with a silane (SiH_4) or tetrachlorosilane ($SiCl_4$) and passed above the metal catalyst accumulated on Si.

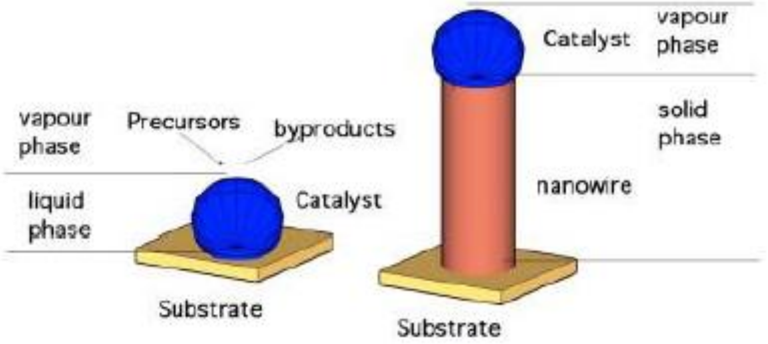

Figure 2: 1 Schematic diagram for VLS technique [8]

wafer in the chamber at above eutectic temperature. The SiH_4 gas serving as the source of silicon gas would be converted into silicon vapor and disperses through a metal catalyst to produce metal-silicon alloy droplets. As silicon diffuses across the metal nanoparticle catalyst leading to a supersaturated state of condition, the silicon will precipitate out from droplets of metal-Si forming silicon nanowires.

2.2.2 Laser Ablation

By laser ablation large quantities of ultrathin nanowires with high aspect ratios can easily be obtained. A high-power pulsed laser ablates material from a mixed Si–catalyst target, which is placed in a tube furnace held at high temperatures and purged with an inert gas. The silicon material ablated from the target cools by colliding with inert-gas molecules, and the atoms condense to liquid nanodroplets with the same composition as the target. The advantages of laser-ablated nanowire production are manifold. Firstly, there is no need for a substrate. Second, the composition of the resulting nanowires can be varied by changing the composition of the laser target.[9]

2.2.3 Oxide assisted growth (OAG)

By OAG method,which is a bottom up approach the growth of SiNWs was significantly improved using SiO as starting material to stimulate the nucleation and the growth of SiNWs without the use of catalyzed metal generating high purities SiNWs and free of metal impurities [10]. One of the features of the produced SiNWs via OAG method is it possesses at its outer layer, an oxide layer that is chemically inert. To efficiently improve the electrical and optical properties of the produced SiNWs, the outer layer covered by oxide layer should be removed by treating the oxide layer with hydrofluoric acid (HF). It should be noted that this method is more preferable to VLS as it enables to produce SiNWs with various morphologies in chains, rods, wires, ribbons, and coaxial structures and the use of silicon sources like silane (SiH4) or SiCl4 can be circumvented.

2.2.4 Molecular Beam Epitaxy (MBE)

In MBE, a solid high-purity silicon source is heated until Si starts to evaporate.A directional gaseous beam of silicon atoms is aimed at the substrate, on which the atoms adsorb and crystallize.To reduce contamination, the base pressure of an MBE system is usually kept at ultrahigh vacuum, allowing to monitor the growth using Reflection High-Energy Electron Diffraction (RHEED) or other surface sensitive examination methods. Similar to CVD, MBE was initially designed for epitaxial layer-by-layer deposition only. [11]

2.2.5 Metal-Assisted Chemical Etching

This is the most low-cost and simple method of synthesizing SiNWs [12]. Silicon can be etched in the presence of HF and an oxidative agent, catalyzed by noble metals, to form micro-/nano-structured surfaces with various morphologies. First step of silicon nanowire synthesis using this process is to deposit metal particle like Au, Ag or Cu on silicon substrate.

These noble metals would attract electrons from the silicon and facilitate Si oxidation. Si etching occurs rapidly when Si substrates covered with Ag/Au-nanoparticle films are immersed in HF as the metal nanoparticles acts as a catalyst.

The final reaction is composed of the following cathodic and anodic reactions:

Cathodic reaction: $Ag^+ + e^- (VB) = Ag(s)$

Anodic reaction: $Si(s) + 2H_2O = SiO^2 + 4H+ +4e^- (VB)$

$SiO_2(s) + 6HF = H_2SiF_6 + 2H_2O$

The whole reaction can be summed up as follows:

$$Si(s) + 4Ag^+ + 6HF^- \rightarrow 4Ag + H_2SiF_6 + 4H^+$$

When parameters like temperature, concentration and deposition time, and doping level are manipulated, diverse morphologies of SiNWs arrays could be produced by this mechanism. [13]

2.3 Properties

Silicon nanowires properties are:

2.3.1 Mechanical properties:
Mechanical properties of nanowires are of great importance in device processing since changes in temperature, induced strain and external stress can change the electrical conductivity of the nanowire due to internal dislocations.

2.3.2 Electrical properties:
It is important to understand the electrical properties of semiconducting nanowires because they determine the suitability of silicon nanowires to be used in electronics and sensor applications.

2.3.3 Chemical properties:
An important chemical reaction, which makes silicon nanowires very useful in sensor and transistor applications, is the natural oxidation.

2.3.4 Optical properties:
Outstandingly, SiNWs developed laterally and most of the crystallographic orientations have a direct band gap; as a result, both the maximum and minimum of the valence band and the conduction band respectively occur at a

similar point in k-space. This unique property has made SiNWs as effective optically active materials for photonics applications.

2.3.5 **Thermal properties:** Silicon nanowires, when used within applications or experiments, may have a curved like shape and not be straight. The phonon transport can be affected by their curvature and thus their thermal conductivity changes.

2.4 Applications

2.4.1 Field Emission (FE)

2.4.1.1 Introduction to Field Emission

Removal of a free electron from bound state in metal/semiconductor requires certain amount of external energy. The energy required to eject a bound electron to free state must exceed certain minimum energy level termed as work function, φ. It is the energy difference between the highest filled energy state, the Fermi level (EF) and the vacuum level. Depending upon the type of external applied energy, to eject the electrons; the emission can be classified as follows:

- Thermionic emission (TE): external applied energy is in the form of heat
- Photoemission(PE) : external applied energy is in the form of photons
- Secondary emission: primary incident particles with sufficient energy induce secondary particles emission.
- Field electron emission(FE)

The **Field electron emission** (FE) is ejection of electron by quantum mechanical tunneling from conducting/semiconducting emitters upon application of very high electric field (10^6V/cm). Thus, the field emission phenomenon is an experimental realization of electron tunneling effect explained in quantum mechanics.

PE relies on absorption of energy from a photon by an electron, exciting it to a higher state thereby allowing the electron to pass over the surface potential barrier with incident energy $h\nu \geq \phi$, where h is Planck's constant (6.63×10^{-34} Js), ν is the frequency of the wavelength of light and ϕ is the work function of the material.[14] Typically, to gain sufficient energy, the incident light must lie in the ultraviolet part of the electromagnetic spectrum. Whilst physically it is

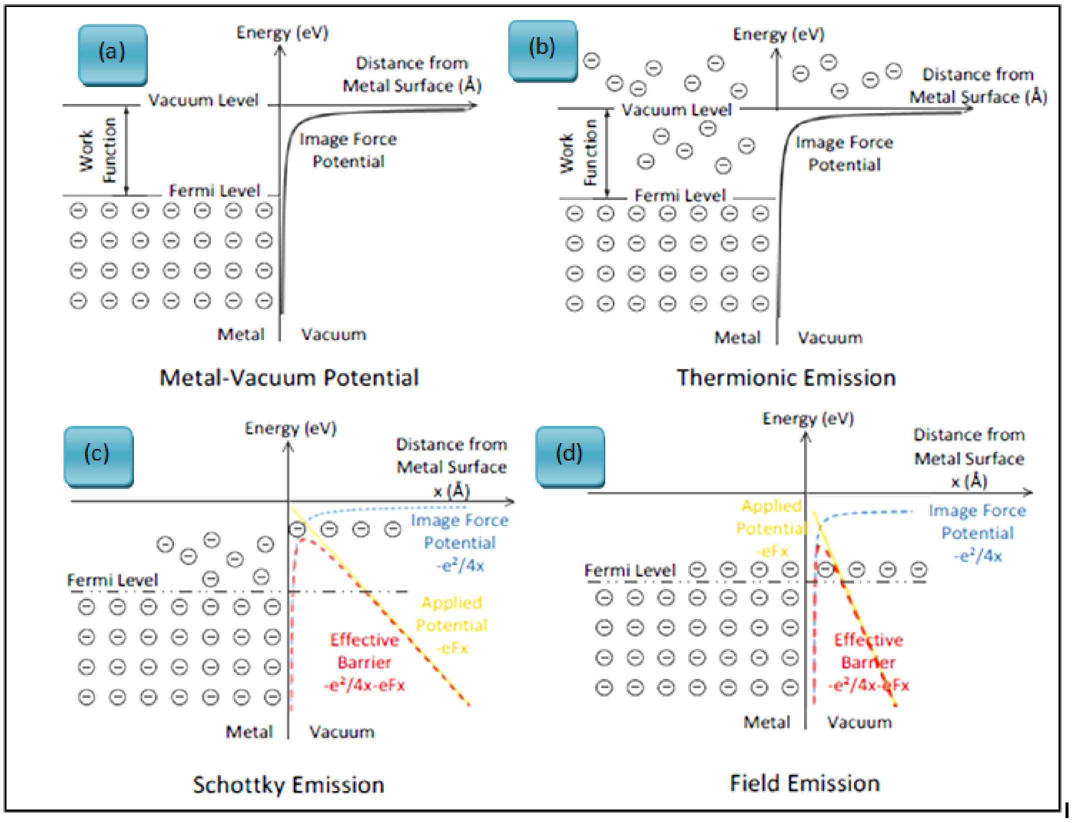

Figure 2: 2 Emission Mechanisms Schematic.(a)potential barrier on metal surface (b)thermionic emission over the classical electric field barrier (c) Shottky emission of electrons (negative circles) and the effective potential barrier seen in Shottky emission as a result of the triangular barrier and image potential. (d) Field emission at the Fermi energy

interesting, with fast response times down to nanoseconds, practically it is the least explored of the emission mechanisms and is not greatly relied upon for use in applications as achieving high currents is challenging.

TE, comparatively, is used extensively. To liberate electrons demands high temperatures (>1000K) in order that they acquire sufficient kinetic energy greater than the restraining surface potential barrier. The quantity of kinetic energy required is defined by work function, ϕ, of the material. Strictly speaking, ϕ is determined by the amount of energy an electron needs to overcome the ionisation potential. Factors that influence work function magnitude are the intrinsic partial free energy of electrons as well as surface electrostatic effects. In the presence of an electric field, the surface potential barrier required for electrons to emit lowers, whilst the shape of the potential barrier also changes from nominally quadrilateral to more triangular. When the principle emission method is thermionic, with electrons passing over the newly lowered barrier, this is termed Schottky emission.[15]

Both PE and TE entail classical physics principles of excitation to pass over a barrier, whereas FE enters the domain of quantum mechanics. FE of electrons necessitates an applied electric field only, without heating, and is accordingly termed cold emission. Electrons tunnel through the vacuum barrier potential at the Fermi energy, E_f, which is significantly narrowed in the presence of an electric field. the emission current is thus produced. With increasing fields, the barrier narrows further and emission current increases with an observed exponential relationship.[16] In semiconductors, electrons from the conduction band are promoted to the valence band by field induction.

The first observation of FE dates back to 1879 when R. W. Wood was working on certain discharge tube experiments.[17] However, the first attempt to explain the mechanism of electron emission was made by W. Schottky in 1923. He explained the field electron emission phenomenon as a reduction in potential barrier at the Fermi level. The phenomenon of reduction in potential barrier is termed as Schottky Effect. Latter on it was proposed by Gossling, that the field emission mechanism is temperature independent almost up to 1500K. The emission mechanism was then explained by R. H. Fowler and L. Nordheim based on quantum mechanical electron tunneling effect. They presented the mathematical formulation of the mechanism in 1928.[18-19]

2.4.1.2 Electron field emission from metals

Electrons in the conduction band of a metal can move freely. However, these electrons cannot leave the metal because of a potential barrier at the surface to vacuum. This potential barrier arises from the electrostatic interaction between adjacent electrons. Regarding electrostatic attraction and repulsion the lowest potential energy of an electron is given by the equilibrium of these two forces.

An electron that leaves the bulk causes a surplus of positive charges in the solid. As a result of this surplus the electron is pulled back. In a classical consideration an electron that wants to leave the solid into vacuum needs enough thermionic energy to get from the Fermi level E_F to the vacuum level E_{Vac} . That amount of work is called the work function ϕ.[20]

Quantum mechanics allow a short term stay of an electron in the forbidden area below the potential barrier. An electron, in that case, has the chance to tunnel through the potential barrier. The chance for tunneling depends on the height and width of the potential barrier. These two parameters can be modified by an external electric field .An external electric field shapes the potential barrier triangularly due to the potential energy of an electron in the electric field:

$$\mathbf{E_{Field} = -q \cdot F \cdot x}$$

with the external electric field F, the charge q and the distance from the surface x.

In addition to the deformation the potential barrier is lowered due to the image charge . This charge originates from the remaining positive charges when an electron has left the solid. With an external electric field the total potential energy results in:

$$E_{pot}(x) = -\frac{e^2}{16 \cdot \pi \cdot \epsilon_o \cdot x} - q \cdot F \cdot x$$

The maximum of $E_{pot}(x)$ gives the lowering of the potential barrier:

$$\Delta\emptyset = \sqrt{\frac{e^3 \cdot F}{4 \cdot \pi \cdot \epsilon_0}}$$

The first satisfactory description of the generated tunneling current has been given by Fowler and Nordheim [18]. The emitted electron current can be described by the following equation:

$$J_x = \int_0^\infty N(Ex)D(Ex)dEx$$

where $N(Ex)dEx$ is the electron supply function, giving the number of electrons crossing the barrier in a direction parallel to the substrate plane (from emitter bulk); and $D(Ex)$ gives the transmission coefficient or tunnelling probability.

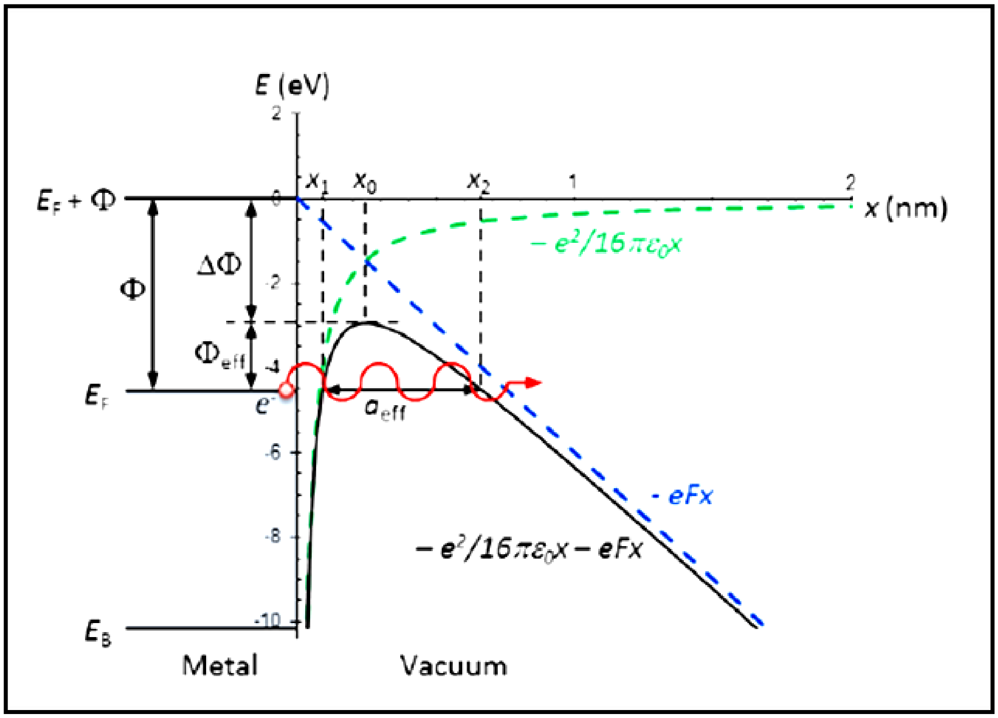

Figure 2: 3 schematic of the potential barrier induced by an electric field including Shottky corrections and image potential.

To calculate (Ex), the Wentzel-Kramers-Brouillon, WKB, approximation is used. Tunnelling occurs when the barrier is significantly thinned by the electric field to less than a few nanometers, with a relationship between increasing emitted electrons and decreasing barrier thickness. For metals, the emission tip is modelled as a semi-infinite quantum well with work function, ϕ, and local electric field, F, approximated as a linear potential. Application of the Fermi-Dirac distribution, which assumes electrons follow the free electron model and hence obey the Pauli Exclusion Principle, and WKB approximation, gives the FN equation, as:

$$J = A_{FN}\frac{F^2}{\phi}\exp\left(-\frac{B_{FN}\,F}{\phi^{3/2}}\right)$$

where the constant A_{FN} is derived from the supply function $N(E_x)dE_x = dE_x\int_{E_x}^{\infty} n(E, E_x)dE_x$ according to the free electron model and B_{FN} from the transmission coefficient $D(E_x) = D_F \exp\left(\frac{E_x - E_F}{dF}\right)$ of the barrier using the solution to the Schrödinger equation and WKB approximation:

$$A_{FN} = \frac{e^3}{16\pi 2\hbar} = 1.54 \times 10^{-6}\,\mathrm{A\,eV\,V^{-2}}$$

$$B_{FN} = \frac{e^3}{16\pi 2\hbar} = 6.83 \times 10^{9}\,\mathrm{eV^{3/2}\,V\,m^{-2}}$$

where e is the electron charge, m_e is the mass of an electron and ħ is Planck's constant h/2π.

A reduced version of the standard FN equation, commonly used in calculations with experimental data, is given by:

$$J = \frac{I}{A} = \left(\frac{A_{FN}\beta^2 E^2}{\phi}\right)\exp\left(-\frac{B_{FN}\phi^{3/2}}{\beta E}\right)$$

where I is the total emission current, A is the effective area of emission, defined by the effective area from which electron liberation occurs from the cathode, which is somewhat dubious and difficult to measure and is commonly mistaken as the area of the substrate onto which the field emitting materials are deposited, E is the local electric field, and β is the field enhancement factor relating to an increase in the observed local field around sharp tips. E can be approximated using the anode-cathode voltage, V, and inter-electrode separation, d, by $E=(V/d)$, where β is a proxy metric for AR or tip sharpness. The quantities I and A can be directly measured under experimental conditions, and give rise to the calculation of factors such as β and, of course, J. According to the general WKB approximation and subsequent transmission models, low ϕ and high β typically manifest as high maximum current density. The reduced FN equation is commonly used to calculate FN behaviours from a nanomaterial emitter. A linear fit to a plot of ln (J/E^2) (y-axis) against 1/E (x-axis), typically called an FN plot, indicates that a material follows Fowler-Nordheim theory well. A linear rearrangement here gives:

$$\ln\left(\frac{J}{E^2}\right) = \left(-\frac{B_{FN}\phi^{3/2}}{\beta}\right)\frac{1}{E} + \ln\left(\frac{A_{FN}\beta^2}{\phi}\right)$$

The local field enhancement factor, β, is related, in part, to the emitter geometry, with high aspect ratio materials, such as CNTs, proving to be excellent candidates by exhibiting very large values. The value of β is measured by inference of known quantities including J, E and ϕ. Due to complexities arising in accurately assessing E and indeed ϕ, however, calculated values of β are wildly disparate with values from 1 to 10,000, although it should be noted that emitter morphology can also vary wildly within a sample and is of high influence in defining β.

Experimentally, the gradient, s, from a Fowler Nordheim plot ($\ln(J/E^2)$ against 1/E) is commonly used to derive the local field enhancement factor, β, when ϕ is known, given by:

$$\beta = -\frac{B_{FN}\phi^{3/2}}{s}$$

Therefore, the field enhancement factor β can be calculated as long as work function is known.

2.4.1.3 Electron field emission from semiconductors

The Fermi level in metals lies within the conduction band and metals have a huge amount of free charge carriers due to metallic bonding. Semiconductors, on the contrary, have their Fermi level in the forbidden area between the valence band and the conduction band. The amount of free charge carriers is adjusted by doping the semiconductor with foreign atoms (acceptor or donator). This leads to a smaller amount of effectively free charge carriers in a semiconductor compared to a metal. Due to this difference arise for the theory of field emission for semiconductors.

Undoped silicon (Si) has a band gap of 1.12 eV and belongs to the group of the semiconductors. When doped with phosphor, Si becomes a n-type semiconductor with a donor level 44 meV below the conduction band [20]. P-type silicon has an acceptor level 45 meV above the valence band and is fabricated by doping silicon with e.g. boron. For electron field emission devices based on silicon, highly doped silicon is usually used.

The carrier concentrations of an intrinsic, an n-type, and a p-type semiconductor along with the simplified band diagram, density of state, and Fermi-Dirac distribution function are shown in Fig. 2.4. The figure shows that, unlike in a metal, the Fermi level is observed to shift in a semiconductor from its intrinsic position of the middle of the bandgap to adjust itself to preserve charge neutrality when donor (of concentration N_D) or acceptor (of concentration N_A) are introduced into the semiconductor. For an n-type semiconductor, the Fermi level shifts towards the conduction band shifting the Fermi-Dirac distribution function with it resulting in a higher electron concentration in the conduction band than that from the intrinsic case at thermal equilibrium at a temperature higher than 0 K. Whereas, for the analogous situation in a p-type semiconductor, the Fermi level shifts towards the valence band and results lower, but not zero, electron concentration in the conduction band. Free electrons for tunneling under high electric fields are, therefore, available in the conduction band in all three types of semiconductors at non-absolute-zero temperature.

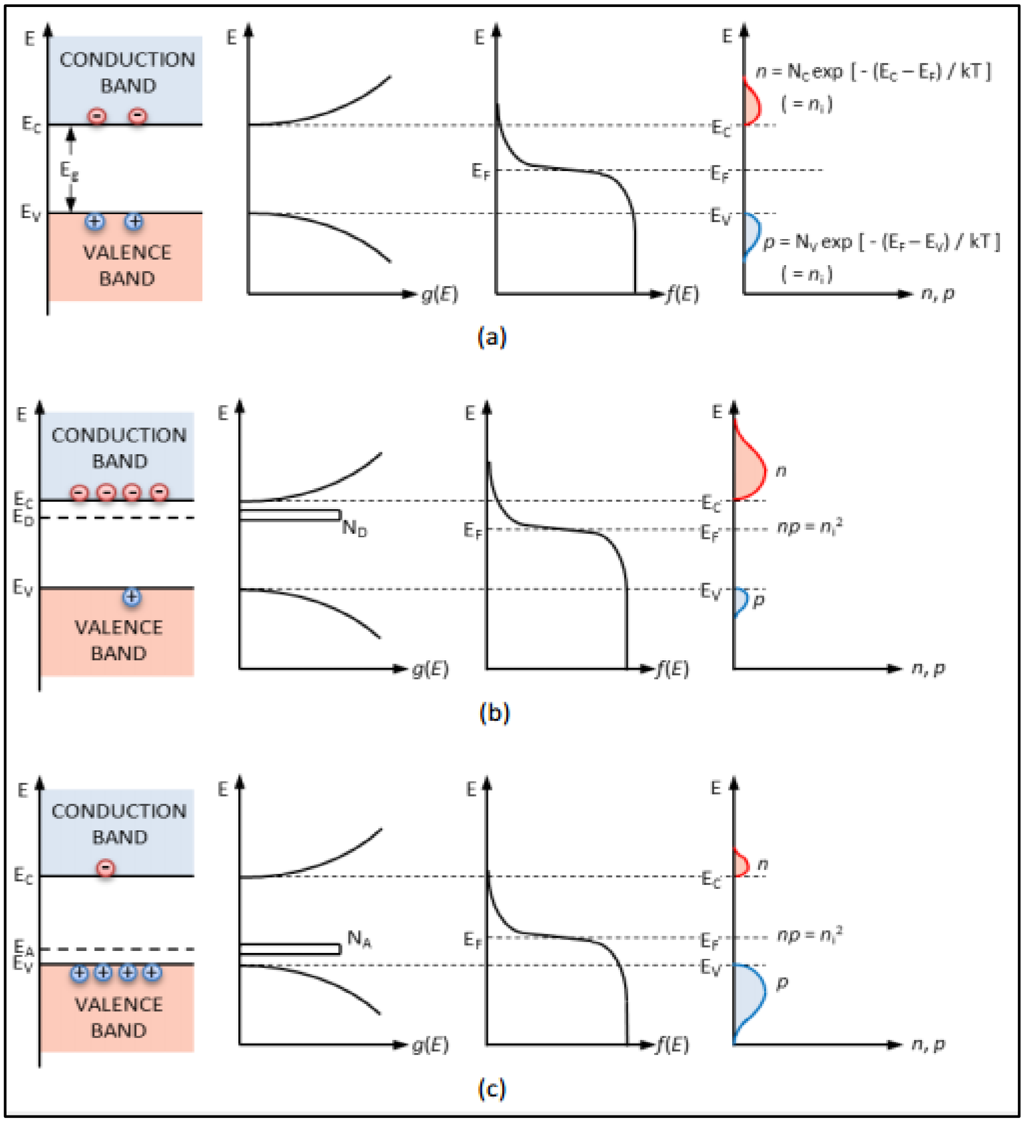

Figure 2: 4(From left) Schematic band diagram, density of states, Fermi-Dirac distribution function, and the carrier concentrations for (a) intrinsic, (b) n-type, and (c) p-type semiconductors at thermal equilibrium at T, where $T \neq 0$ K. N_D, N_A are the donor and acceptor impurities concentrations.

In its simplest form, therefore, a parallel can be drawn between field emission from metals and semiconductors noting that the surface potential barrier height from the bottom of the conduction band is the electron affinity χ for emission from conduction band, and from the top of the valence band it is $\chi + E_g$ for emission from valence band. E_g is the bandgap that separates the conduction band from the valence band. This simple model of electron emission from a semiconductor is illustrated in Fig. 2.5. The corresponding Fowler-Nordheim current from semiconductor conduction and valence band will be given with χ and $\chi + E_g$ respectively replacing ϕ.

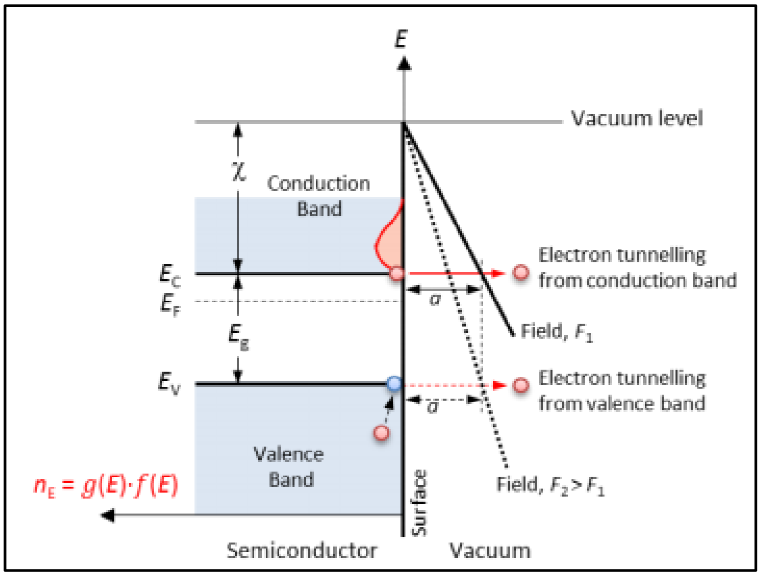

Figure 2: 5 Schematic of the simplest model of field emission from an n-type semiconductor. The model is same for p-type semiconductor too.

The simple model of field emission is not critically realistic as the external electric field penetrates into the semiconductor and both the conduction and valence bands bend at the surface, as shown in Fig. 2.6.[21] Two cases can arise at the conduction band:

- If the conduction band is bent by an energy V_0 not sufficient to bring it below the Fermi level as presented in Fig. 2.6(a), the electrons at the bottom of the conduction band encounters a barrier of height χ as before the field penetration being considered. However, the Fowler-Nordheim current density would require to be multiplied by a factor $e^{-V_0/KT}$ representing the increased electron concentration at them bottom of the bent conduction band. This situation can arise in an intrinsic semiconductor where Fermi level is in the middle of the bandgap or in a lightly doped n-type semiconductor where it is a considerable distance away from the conduction band edge.

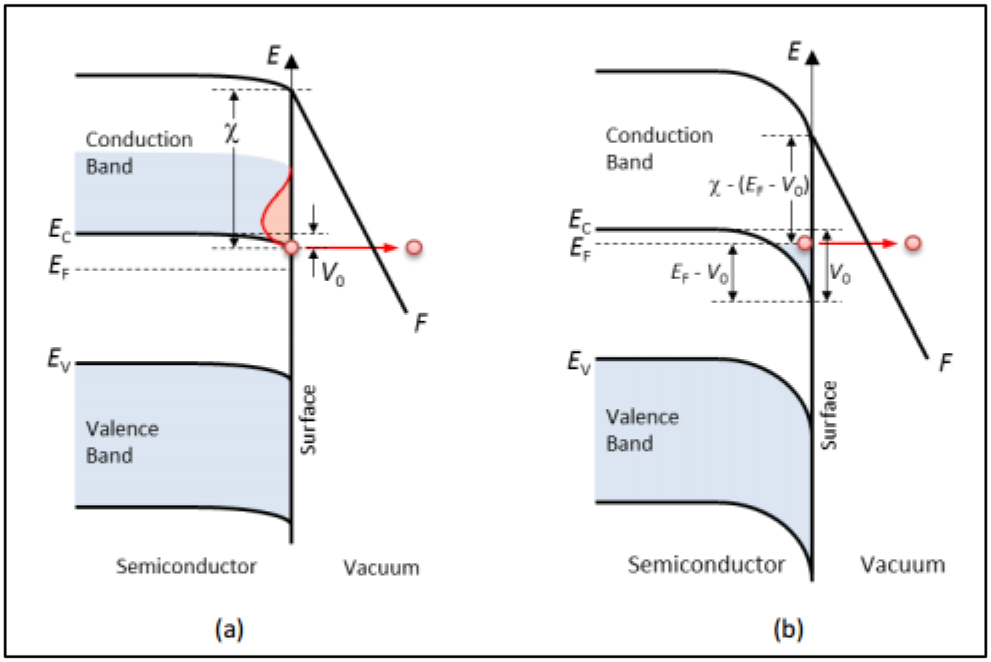

Figure 2: 6 Field emission from the conduction band of an n-type semiconductor with field penetration. The conduction band has bent but (a) has not dipped below the Fermi level, and (b) has dipped below the Fermi level near the semiconductor surface.

- If at high field, V_0 is sufficient to bring the bottom of the conduction band below the Fermi level, as in a moderately to highly doped n-type semiconductor where Fermi level lies close to the conduction band, electrons collect in the dip as depicted in Fig. 2.6(b). It is evident that the highest filled level of the collection coincides with the Fermi level, which remains constant throughout the semiconductor. In this case, the barrier height is reduced by an amount and the effective barrier height for the Fowler-Nordheim equation is given by

$$\phi_{\mathrm{eff}} = \chi - \left(E - V_0 \right)$$

The field penetration has no effect in emission from semiconductor valence band as barrier height χ + Eg remains unchanged at the semiconductor surface even with the bent valence band.

2.4.1.4 Nanowires as field emitters

Nanowires of different materials are of immense interest due to their one-dimensional structures showing quantum confinement effects. Nanowires also possess high surface to volume ratio. Nanowires possess axial geometry and such nanorods like structures can be grown vertically on flat substrate with desirable density of wires per unit area. In particular, nanowires with low threshold and low operating voltage have become potential candidates for application in flat panel display technology as well as in the cold cathode technology. This is because the conventional thermionic emission devices are accompanied with high power dissipation due to high cathode temperature. Aligned nanowires with a high packing density can significantly enhance the field emission behavior.

2.4.2 Wettability

2.4.2.1 Wetting of a solid surface

Wettability of a solid surface is quantitatively measured in terms of contact angle. The contact angle is the angle at which the liquid-vapor interface meets solid-surface interface. As the tendency of a liquid drop is to spread out over a flat, solid surface increases, contact angle decreases. Thus, the contact angle provides a direct measurement of wettability. A contact angle less than 90° usually indicate wetting of the surface is very favorable, and the liquid will spread over a large area of the surface. Contact angles greater than 90° generally mean that wetting of the surface is unfavorable so the fluid will minimize contact with the surface and form compact liquid droplet. The solid surfaces are broadly classified as hydrophobic or hydrophilic depending upon the extent to which the wetting of the surface is facilitated. Hydrophilic surface as the name itself implies, means surfaces having affinity to water. Since the contact angle formed is less than 90°, the exposed area of liquid to air is less. Water spreads very well on these surfaces. Glass is an example of this type of surfaces. On the other hand, on hydrophobic surfaces, water does not spread well. The water drops formed on these surfaces have higher surface energy forming the contact angle always more than 90°.

2.4.2.2 Contact angle and Young's equation

Contact angle measurements are widely used for the evaluation of macroscopic surface characteristics such as wettability, hydrophobicity, adhesion, and the surface tension of solids. When an interface exists between a liquid and a solid, the angle between the surface of the liquid and the outline of the contact surface is described as the contact angle θ. The contact angle (wetting angle) is a measure of the wettability of a solid by a liquid. In the case of complete wetting (spreading), the contact angle is 0°. Between 0° and 90°, the solid is wettable and above 90° it is not wettable. In the case of ultra-hydrophobic materials with the so-called lotus effect, the contact angle approaches the theoretical limit of 180°.

The theoretical description of contact arises from the consideration of a thermodynamic equilibrium between the three phases: the liquid, solid and the gas/vapor phases. It is convenient to frame the discussion in terms of the interfacial energies. According to Young's equation,[22] there is a relationship between the contact angle θ, the surface tension of the liquid σ_{ls}, the interfacial tension σ_{sl} between liquid and solid and the surface free energy σ_{sg} of the solid:

$$\sigma_L \cos \theta_c = \sigma_s - \sigma_{SL}$$

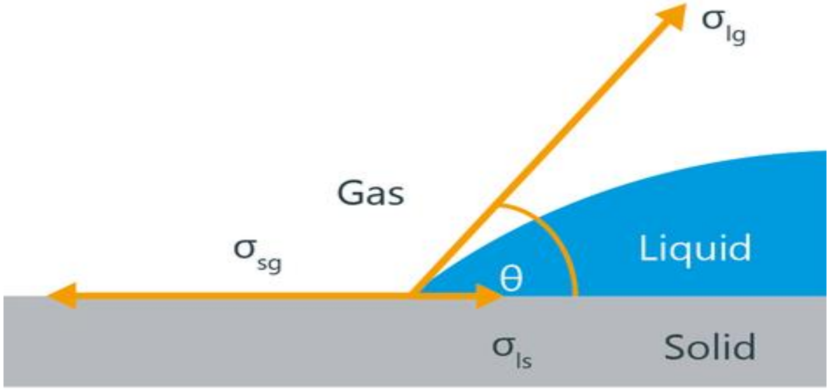

Figure 2: 7 Schematic of Contact Angles

2.4.2.3 Types of Surfaces

- **Hydrophilic Surface:**

Whenever we dissolve compounds or molecules into water, we are taking advantage of the fact that these chemicals are hydrophilic. If a compound is hydrophilic (or 'water loving'), then this means the compound readily dissolves in water or a watery solvent.

Water is a polar molecule. Polar molecules are molecules that have partial charges due to uneven bonding. The oxygen atom in a water molecule is highly electronegative, which means that it will pull the electrons in a bond closer to it. This in turn, makes oxygen partially negative, and hydrogen partially positive.

Since water has these partial charges, it can attract other chemicals that also have partial charges. Therefore, hydrophilic molecules must have a charged portion in order to dissolve in water. Hydrophilicity is an important quality of many essential materials in nature and in the human body.

Consider a liquid drop on a solid surface. If the liquid is very strongly attracted to the solid surface (for example water on a strongly hydrophilic solid) the droplet will completely spread out on the solid surface and the contact angle will be close to 0°. Less strongly hydrophilic solids will have a contact angle up to 90°. On many highly hydrophilic surfaces, water droplets will exhibit contact angles of 0° to 30°. A membrane being hydrophilic means it has the tendency to allow liquid to enter the pores. This condition reflects better wetting, better adhesiveness, and higher surface energy.

Hydrophilic solids are often hygroscopic and pick up water from the air. Taking simple examples from the kitchen, both salt (sodium chloride; electrolyte) and sugar (sucrose; nonelectrolyte) easily dissolve in water, in large quantities, and both of these substances are therefore hydrophilic, as per this general definition. Since surfaces of salt and sugar crystals are chemically identical to the composition of bulk of the crystals, they must be hydrophilic as well.

e.g. glass, rusted materials

- **Hydrophobic Surface:**

Hydrophobic surface has the property of repelling water, i.e., they do not easily become wetted in contact with water. The phenomenon is due to unbalanced molecular forces at the water/solids interface causing surface tension. Water is a polar molecule, which means that it carries a partial charge between its atoms. Oxygen, as an electronegative atom, draws the electrons of each bond closer to its core, thus creating a more negative charge. Therefore, any materials with a charge, whether it is negative or positive, will be able to interact with water molecules to dissolve. (Think of how salt dissolves in water. This is due to the charges of the ions sodium and chlorine). So essentially, hydrophobic molecules are molecules that do not have a charge, meaning they are non-polar. If the surface is hydrophobic, contact angles will be greater than 90° (high contact angle), generally means that wetting of the surface is unfavorable, so the fluid will minimize contact with the surface and form a compact liquid droplet. e.g.: Teflon, Oily surface .

- **Super Hydrophobic Surface:**

The contact angles of a water droplet on an ultra-hydrophobic material exceed 150°. This is also referred to as the lotus effect, after the super hydrophobic leaves of the lotus plant. A droplet impacting on these kinds of surfaces can fully rebound like an elastic ball. Super hydrophobic surface is a hydrophobic surface having nano-scale roughness.

For nano scale roughness water-solid contact area is lowered and water perched on hydrophobic posts containing trapped air.

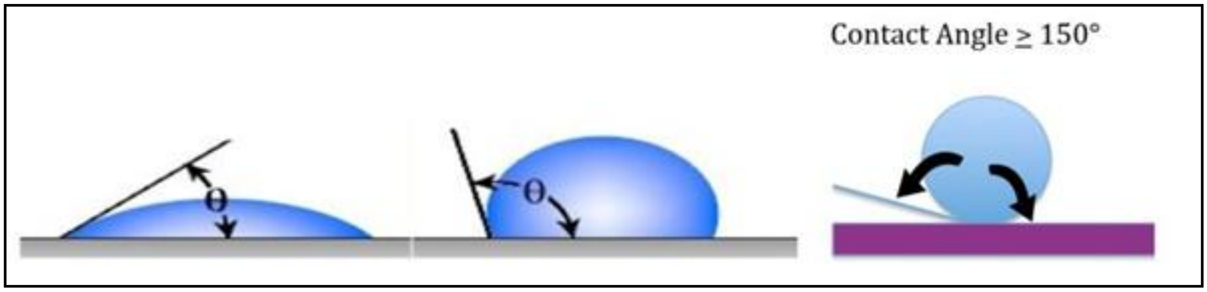

Figure 2: 8 Schematic of Contact Angles

Surface Wettability relation with Surface Energy

A high wetting surface has a surface energy that creates a strong attractive force to pull the liquid droplet down, causing it to spread out. This is known as wettability.

This surface energy is stronger than the surface tension of the liquid's molecules that would normally keep it in droplet form. The surface tension of the liquid doesn't change, but rather the surface energy of the solid is stronger than the liquid's surface tension and overpowers it, causing the liquid to spread out over the solid surface.

Low contact angle = high surface energy and high interfacial tension.

For a low wetting surface, the surface energy is weaker than the surface tension of the liquid, meaning that the liquid can better keep its droplet shape. The interfacial tension between the solid and liquid is low because the interaction between the two is not as strong.

High contact angle = low surface energy and low interfacial tension.

Surface energy and surface tension result from non-symmetric bonding of the surface atoms/molecules in contact with a vapour are measured as energy per unit area. Surface tension is often used to define fluid surfaces while surface energy is used to define solid surfaces. Surface energy is an important indicator of surface contamination and the composition of a polymer surface. Surfaces with a high surface energy will try to lower their energy by adsorbing low energy materials such as hydrocarbons.

2.4.2.4 Effect of Surface Roughness on wettability

Superhydrophobic surfaces are so hydrophobic that it becomes extremely difficult to wet. They are usually referred to have contact angles exceeding 150° and the roll-off angles less than 5°. Since chemically modifying the surface alone can typically lead to contact angles of up to 120°, but not more, superhydrophobicity is known to be an enhanced effect of surface roughness - the Lotus' effect. The basic wetting state of droplets on a rough substrate is either in Wenzel's[23] or Cassie-Baxter's[24]. Usually, only one of these states is stable while the other is metastable , depending on both the surface chemistry and roughness.

Surface roughness has a strong effect on the contact angle and wettability of a surface. The effect of roughness depends on if the droplet will wet the surface grooves or if air pockets will be left between the droplet and the surface.

If the surface is wetted homogeneously, the droplet is in Wenzel state. In Wenzel state, adding surface roughness will enhance the wettability caused by the chemistry of the surface.

$$\cos\theta^* = r\cos\theta$$

If the surface is wetted heterogeneously, the droplet is in Cassie-Baxter state. The most stable contact angle can be connected to the Young contact angle. The contact angles calculated from the Wenzel and Cassie-Baxter equations have been found to be good approximations of the most stable contact angle.

$$\cos\theta^* = r_f f\cos\theta - (1 - f)$$

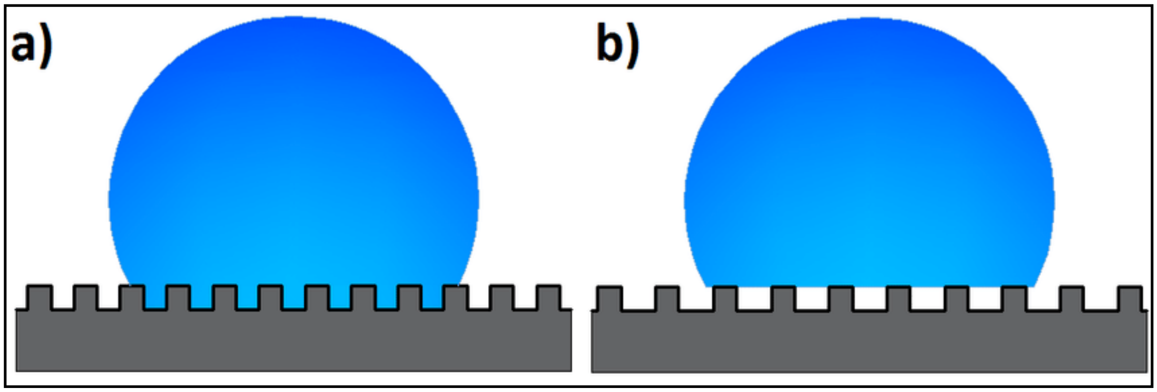

Figure 2: 9 Representations of (a) Wenzel and (b) Cassie-Baxter models.

Where, the parameter *r* is the ratio of the wet surface area to its projection on the apparent solid plane, and *f* is the area fraction of the wet part of the solid. The Wenzel and Cassie-Baxter relations have classically been used to characterize the apparent contact angles with remarkable success. The latter reveals that θ * comes near 180° as the area fraction *f* approaches to zero. Wetting in the Cassie-Baxter's state, rather than in the Wenzel state, is generally a requirement for achieving superhydrophobicity.

2.5 Objective

The following are the mains objectives undertaken in this project:

- To synthesize silicon nanowires (SiNW) by metal assisted chemical etching (MaCE) process and to investigate the change in morphology, band gap and field emission parameters for different time duration for synthesis i.e. 40, 60 and 80 minutes of etching in 60°C.

- To further enhance the field emission properties of the silicon nanowires etched at 80 minutes thin rGO(Reduced Graphene Oxide) layer is deposited on it to synthesize rGO-SiNW composite.

- To investigate the change in wettability properties of silicon nanowires etched in both room temperature and 60°C for time periods of 40, 60 and 80 minutes and also the wettability of rGO-SiNW composite.

- To investigate the effect of wettability properties in the field emission characteristics of the nanowires and its composite.

References:

[1] T. Mikolajick, A. Heinzig, J. Trommer, S. Pregl, M. Grube, G. Cuniberti, W.M. Weber, "Silicon nanowires—a versatile technology platform." Phys. Status Solidi Rapid Res. Lett. 7,793–799 (2013).

[2] Liu, L.C.; Huang, M.J.; Yang, R.; Jeng, M.S. and Yang, C.C. ‘Curvature effect on the phonon thermal conductivity of dielectric nanowires’, Journal of Applied Physics, 105(10), (2009).

[3] Bjork, M.T.; Schmid, H.; Knoch, J.; Riel, H. and Riess, W. (2009) ‘Donor deactivation in silicon nanostructures’, Nature Nanotechnology, 4(2), pp.103-107

[4] N. Singh, K.D. Buddharaju, A. Agarwal, S.C. Rustagi, C.Q. Lo, N. Balasubramanian, D.L.Kwong, “Fully gate-all-around silicon nanowire CMOS devices.” Solid State Tech. 51, 34 (2008)

[5] M.D. Kelzenberg, S.W. Boettcher, J.A. Petykiewicz, D.B. Turner-Evans, M.C. Putnam, E.L. Warren, J.M. Spurgeon, R.M. Briggs, N.S. Lewis, H.A. Atwater, “Enhanced absorption and carrier collection in Si wire arrays for photovoltaic applications.” Nat. Mater. 9, 239–244 (2010)

[6] K.-Q. Peng, X. Wang, L. Li, Y. Hu, S.-T. Lee, “Silicon nanowires for advanced energy conversion and storage.” Nano Today 8, 75–97 (2013)

[7] Suzuki H, Araki H, Tosa M, Noda T. “Formation of silicon nanowires by CVD using gold catalysts at low temperatures.” Mater Trans. 2007;48:2202–2206.

[8] E. Comini, C. Baratto, G. Faglia, M. Ferroni, A. Vomiero, and G. Sberveglieri, “Quasi-one dimensional metal oxide semiconductors: Preparation, characterization and application as chemical sensors,” Prog. Mater. Sci., vol. 54, no. 1, pp. 1–67, Jan. 2009.

[9] Zhang YF, Tang YH, Wang N, Yu DP, Lee CS, Bello I, Lee ST “Silicon nanowires prepared by laser ablation at high temperature.” Appl Phys Lett (1998) 72:1835–1837

[10] Shao M-W, Zhang N-BW M-L, et al. “Ag-modified silicon nanowires substrate for ultrasensitive surface-enhanced raman spectroscopy.” Appl Phys Lett. 2008;93:233118.

[11] Werner P, Zakharov ND, Gerth G, Schubert L, Go¨sele U “On the formation of Si nanowires by molecular beam epitaxy.” Int J Mater Res 97(2006):1008–1015

[12] Huang Z, Geyer N, Werner P, de Boor J, Gösele U Metal-assisted chemical etching of silicon: a review. Adv Mater. 2011 Jan 11; 23(2):285-308.

[13] Zhang ML, Peng KQ, Fan X, Jie JS, Zhang RQ, Lee ST, Wong NB. Preparation of large-area uniform silicon nanowires arrays through metal-assisted chemical etching. J Phys Chem C. 2008

[14] Collins, C. M., Parmee, R. J., Milne, W. I. & Cole, M. T. “High Performance Field Emitters.” Advanced Science 3 (2015).

[15] Baca-A, R., Paredes-R, G. R., Pena-Sierra, R. & Ieee. “Study of materials to synthesize vacuum electron nanoemitters.” (2006).

[16] Zhao, Z. G., Liu, S. H., Liu, C., Bai, J. B. & Cheng, H. M. “A comparison between field-emission properties of three one-dimensional carbon materials.” Physica B-Condensed Matter 396, 44-48 (2007).

[17] Wood, R. W. A New Form of Cathode Discharge and the Production of X -Rays, together with Some Notes on Diffraction. Preliminary Communication. Phys. Rev. (Series I) **5,** 1–10 (1897).

[18] R. H. Fowler and L. Nordheim, “Electron Emission in Intense Electric Fields,” Proceedings of the Royal Society of London, Math. Phys. Eng. Sci. 119, 173–181 (1928).

[19] Stern, T. E., Gossling, B. S. & Fowler, R. H. Further Studies in the Emission of Electrons from Cold Metals. Proc. R. Soc. A Math. Phys. Eng. Sci. 124, 699–723 (1929).

[20] G. Fursey, Field Emission in Microelectronics, I. Brodie, Ed. Kluwer Academics/Plenum Publishers, 2005.

[21] Tsong, T. T. Field penetration and band bending for semiconductor of simple geometries in high electric fields. Surf. Sci. **85,** 1–18 (1979).

[22] Young T. An essay on the cohesion of fluids. Phil. Trans. R. Soc. Lond. 1805;95:65-87.

[23] Wenzel RN. "Resistance of solid surfaces to wetting by water." Ind. Eng. Chem. 1936;28(8):988-994.

[24] Cassie ABD, Baxter S." Wettability of porous surfaces". Trans. Faraday Soc. 1944;40:546-551.

Chapter 3

Literature Review

3.1 Review of Past Work

Silicon nanowires, also referred to as SiNWs, have unique quasi one-dimensional electronic structure and high surface to volume silicon ratio. Therefore , silicon nanowire based devices have properties that can outperform their traditional counterparts in many ways. SiNWs are expected to play a key role in applications such as solar cells, sensors, lithium batteries, and catalysts with regard to their surface-dependent properties.

- The synthesis of silicon nanowires are to be discussed first. R.S.Wagner and W.C.Ellis reported the synthesis of silicon nanowires (SiNWs) for the very first time in **1964** via vapour–liquid–solid (VLS) growth by using gaseous silane (SiH_4) as precursor and gold (Au) nanoparticles as catalysts.[1]

- In **1997**, Dimova-Malinovska et al. reported that thin porous silicon layers (1000Å) were fabricated by etching an aluminum (Al) covered Si substrate in a solution composed of HF, HNO_3 , and H_2O for both p-type Si and n–p Si junctions. **[2]** This is the first demonstration of metal assisted chemical etching of silicon.

- The widely used metal-assisted chemical etching method was first investigated in detail by Li and Bohn in **2000**. [3] It was found that a thin layer of noble metal (e.g., Au, Pt, or Au/Pd alloy) sputtered on the surface of a Si substrate(100) catalyzed the etching of Si in a mixed solution containing HF, H_2O_2 , and EtOH, resulting in straight pores or columnar structures. Depending on the type of metal deposited and Si doping type and doping level, porous Si with different morphologies were produced.

Metal-Assisted Chemical Etching (MACE) is particularly promising among all other methods, because of its simplicity, cost-efficiency, and versatility. By MACE various Si nanostructures can be fabricated with the ability to control various parameters (e.g., cross-sectional shape, diameter, length, orientation, doping type, and doping level).[4]

Field emission is important in several areas of industry, including lighting and displays. The applications of field emission are in field emission displays, microwave power amplifiers, parallel e-beam lithography tools and electron guns for electron microscopes. As Si is the most important semiconductor for development of modern microelectronic technology attempts have been made to develop excellent field emission properties in Si nanostructures.

- In **1999**, Frederick et al. first reported the field emission properties of SiNWs which were synthesized by a laser-ablation method. For a current density of 0.01mA/cm^2 the turn-on field of the SiNW emitters with a nominal diameter ~10 nm(diameter distribution 7–12 nm), ~20 nm(diameter distribution 18–22 nm), and ~30 nm(diameter distribution 27–32 nm) were 4.5, 13, and 23 V/μm, respectively. The field-enhancing factor was determined to be ~500 by taking the local work function of the emission tip as that of elemental silicon, i.e., 3.6 eV. Further enhancement of the field emission was observed for the SiNWs of diameter ~20 nm after treated with hydrogen (H_2) plasma. Decreasing diameter and H_2 plasma treatment of SiNWs improved their field emission characteristics. [5]

- In **2003,** Lu et al. synthesized well-aligned arrays of silicon nanowires (SiNWs) by a chemical vapor deposition (CVD) template method without catalyst. The turn-on field for electron emission, defined as the macroscopic fields needed to produce a current density of 0.01 mA/cm^2, is ~14 V/μm. They concluded that the superior field emission behavior is believed to originate from the sharp tips and oriented growth of SiNWs.[6]

- Chueh et al. in **2005** have synthesized taperlike SiNWs by annealing of high-density $FeSi_2$ nanodots on (001) Si at 1200 ° C in a N_2 ambient. The tip regions of SiNWs were about 5–10 nm in diameter and the average length of the SiNWs was about 6 μm with aspect ratios as high as 150–170. The taperlike Si nanowires exhibit a turn-on field of 6.3–7.3 V/μm for generating a current density of 0.01 mA/cm2 and the threshold field of 9–10 V/mm for current density of 10 mA/cm^2. The excellent field emission characteristics are attributed to the taperlike geometry of the crystalline Si nanowires.[7]

- Kulkarni et al. reported the electron field-emission characteristics of SiNWs grown by the vapor-liquid-solid(VLS) technique in **2005**. The average threshold field for emission current density of 10mA/cm2 was found to be 11.58 V/μm and β was estimated to be ~500 using the work function of intrinsic Si (ϕ =4.5 eV). Threshold field was further reduced via postgrowth processing steps such as in situ annealing and in situ cesiation to ~9.9±0.3 V/μm and ~7.76±0.55 V/μm respectively.[8]

- In **2006**, She et al. reported a technique involving a combination of using self-assembled nanomask and anisotropic plasma etching is developed for fabricating vertically aligned single-crystalline SiNWs. The typical J-E curve of the as-fabricated SiNWs gave turn-on field of 0.8 MV/m and the threshold field of 5.0 MV/m(defined as the electric field required to extract a current density of 10$\mu A/cm^2$ and 10 mA/cm^2, respectively). An emission current density of 442 mA/cm^2 was obtained at an applied field of ~14 MV/m and β was found out to be 455.[9]

- McClain et al. in **2006** studied the effects of growth parameters on the morphology and field emission performance of silicon nanowires which were synthesized by chemical vapor deposition using indium tin oxide-coated glass as a substrate. Silicon Nanowires having growth-times of 5, 10, and 20 mins, the turn-on fields were determined to be 7.4, 7.9, and 11.5 V/μm, while the threshold fields were 9.9, 11.8, and 16.9 V/μm respectively. The turn-on and threshold fields referred to were, respectively, the applied fields required to obtain current densities of 10 μA/cm2 and 10 mA/cm^2. The resulting field enhancement factors were calculated to be 540, 270, and 265 for 5, 10, and 20 min growth-times, respectively from FN plot while peak emission currents in excess of 25 μA were observed for nanowires with 5 min growth-times. It was concluded that field enhancement factor increased with decreasing radius of curvature of the emitting tip which is directly related with the radius of SiNWs and emitter surface density also effected on the field emission performance of the SiNW specimens.[10]

- In **2007**, Zeng et al. investigated field emission of single crystal SiNWs of 100 nm in diameter by chemical vapor deposition growth procedure at 480 °C from silane using Au as catalyst. A turn-on electric field of 5.5 V/mm was obtained at an emission current density of 0.01 mA/cm^2 for the as-grown Si nanowires, and the highest saturated current density obtained was 0.03 mA/cm^2 . the same sample was annealed in vacuum at 550 °C for 24 h which improved the turn-on voltage to 2.0 V/mm and an emission current density of 1mA/cm^2 was obtained at 3.4 V/μm.[11]

- Zeng et al. reported an emission current density of 1 mA/cm2 was achieved at an electric field as low as 0.7 V/μm from Si nanowires grown on carbon cloth in **2007**. SiNWs were grown on carbon cloth via the vapor-liquid-solid reaction using silane gas as the silicon source and gold as catalyst from the decomposition of hydrogen gold tetrachloride. turn-on electric field of 0.3V/mm was obtained at an emission current density of 0.01 mA/cm2 and a field enhancement factor of 6.1×10^4.[12]

- In **2007**, Fang et al. synthesized well-aligned and evenly distributed SiNWs assembled in micro-sized semisphere ensembles through simple thermal evaporation without using any templates and me tal particle catalysts. a typical nanowire array density was of ~4 $\times 10^9$ cm^{-2} The turn-on field for field-emission of the arrays was found out to be 7.3 V/μm and the field enhancement factor b was measured as ~424.[13]

- Hsin-Luen Tsai in **2013** fabricated SiNWs by the vapor-liquid-solid (VLS) mechanism in the low pressure chemical vapor deposition chamber with Au catalyst and silane (SiH_4) precursor at three different Au sputtering times (10, 30, and 60 sec) with the growth time at 60 min. material. The higher number density of silicon nanowires was observed with longer sputtering time. The turn-on electric fields are found at 1.2, 4.6, and 7.6 V/μm for three sputtering time at 10, 30, and 60 sec respectively at the growth time 60 min.[14]

- In **2014,** Shasha et al. employed Ag-assisted chemical etching combined with polystyrene(PS) sphere as template to prepare size-controllable single crystal SiNWs with uniformity, and the diameter was further reduced via dry oxidation. The polystyrene monolayer template was first prepared on a p-type (100) oriented Si wafer. Then the diameter of the PS sphere was reduced via Reactive ion etching (RIE) with an O_2 flow rate of 40 sccm, basic pressure of 2 Pa, and applied radio frequency power of 30 W and the etching time was adjusted to control the diameter. After that, Ag was deposited onto the Si substrate by electron-beam evaporation forming a porous Ag film as catalyst. The Ag films used for the chemical etch were deposited at ~ 3 Å s-1. After the removal of PS sphere templates from the

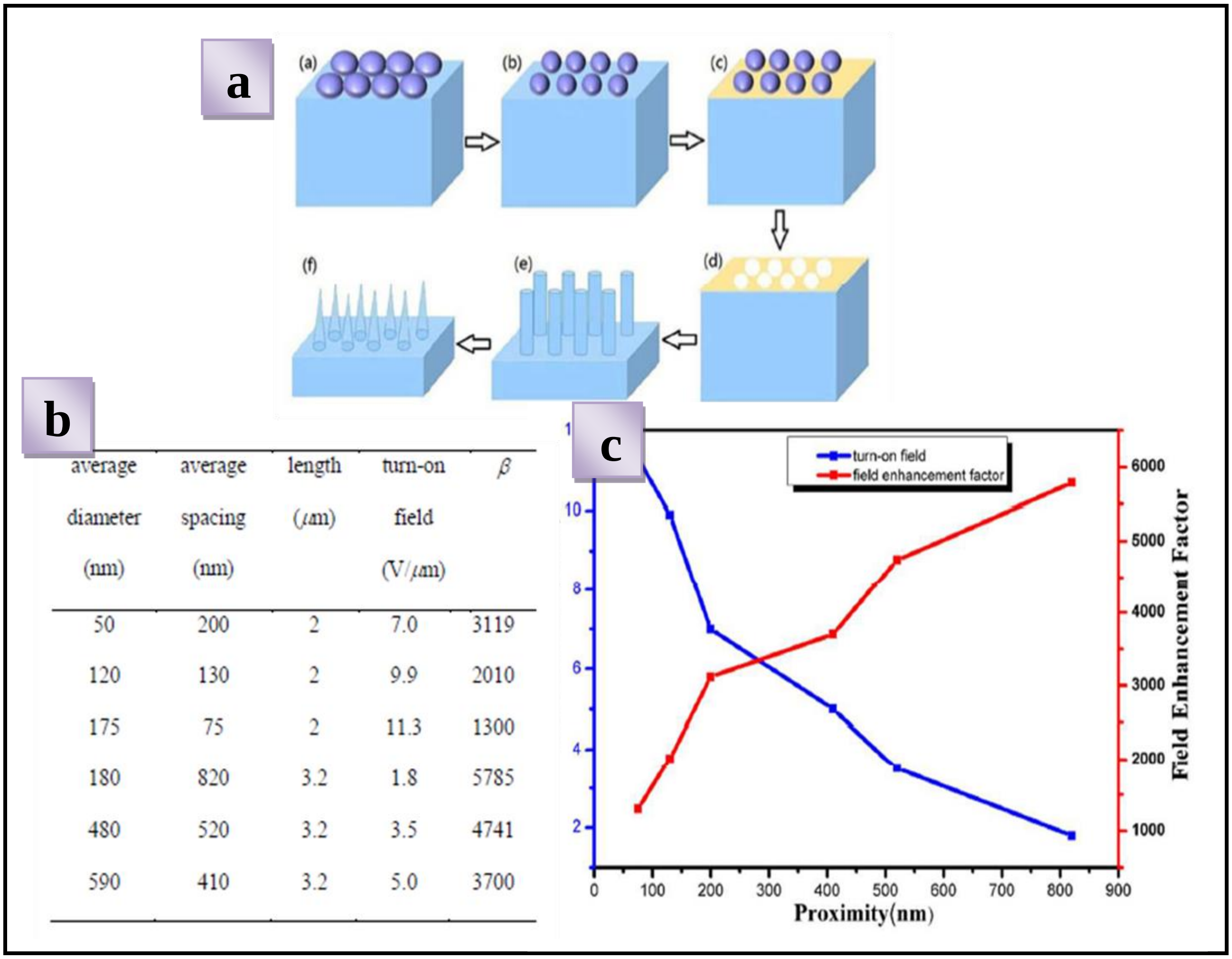

average diameter (nm)	average spacing (nm)	length (μm)	turn-on field (V/μm)	β
50	200	2	7.0	3119
120	130	2	9.9	2010
175	75	2	11.3	1300
180	820	3.2	1.8	5785
480	520	3.2	3.5	4741
590	410	3.2	5.0	3700

Figure3. 1 (a) Schematic depiction of the fabrication process (b) Key Parameters of SiNWs Field Emitters (c) Relationship of turn-on field and field enhancement factor β with proximity in the work by Shasha et.al [15]

substrate by ultrasonication in ethanol or in toluene Ag-assisted chemical etching was done to obtain the silicon nanowires. The FE properties of SiNWs were systematically studied by using two different polystyrene (PS) spheres template with the original diameters of 250 nm and 1000 nm. The turn-on field improved from 11.3 to 1.8 V/μm was observed with the average tip space increasing from 80 to 820 nm. The field enhancement factor improved progressively, up to 5785. The SiNWs with a tip diameter of 180 nm and height of 3.2 μm showed the lowest emission fields and exhibited favorable FE stability, that is, the emission current fluctuation ~ 10.4 % was observed at a fixed electric field of 2.3 V/μm for 6 h.[15]

Reduced Graphene Oxide thin films with thicknesses ranging from a single monolayer to several layers over large areas resulting in tuning of their opto-electronic properties over several orders of magnitude, making them potentially useful for flexible and transparent semiconductors or semi-metals. [16] The thinnest films exhibit graphene-like ambipolar transistor characteristics, whereas thicker films behave as graphite-like semi-metals. Collectively, rGO could be used for translating the interesting fundamental properties of graphene into technologically viable devices. Recent progress on the large-scale synthesis of single-layer graphene by chemical exfoliation opens up the possibility to investigating their field-emission properties, although assembly of graphene into continuous or patterned films is required for the given utilization of graphene in practical flat-panel displays.

- First the synthesis of Graphene oxide is to be discussed as **Reduced Graphene Oxide** (rGO) is obtained from graphene oxide (GO) . Graphite oxide was first prepared by Brodie in **1859** by repeated treatment of Ceylon graphite with an oxidation mixture consisting of potassium chlorate and fuming nitric acid. Since then, many other procedures had been followed for forming graphitic oxide, nearly all dependent upon strong oxidizing mixtures containing one or more concentrated acids. The methods most commonly used at the present time are the original Brodie synthesis and one described by Staudenmaier in **1898**. [17]

- In the Hummer's method, in **1958** the oxidation of graphite to graphitic oxide was accomplished by treating graphite with essentially a water-free mixture of concentrated sulfuric acid, sodium nitrate and potassium permanganate. The entire process requires less than two hours for completion at temperatures below 45º C and can be carried out safely providing reasonable care is maintained in observing the temperature limitations.[18]

- The graphite oxide was prepared by oxidizing purified natural flake graphite via modified Hummers method. UV-vis spectrum of GO exhibited maximum absorption peak at ~237 nm attributed to π-π* transitions of the C-C bonds. The results of FTIR and Raman spectroscopy showed that the graphite was oxidized by strong oxidants and the oxygen atoms are introduced into the graphite layers forming C=O, C-H, COOH and C-O-C bonds with graphene. The XRD results show 2θ of 12.2° with inter layer spacing equal to 7.26 nm. SEM images demonstrated ultrathin and homogeneous graphene films. Electrochemical behavior of GO modified glassy carbon electrode investigated with reference to K_3FeCN_6 redox system reflect that the electrochemical behavior is controlled by the electron transfer.[19]

- **Reduced Graphene Oxide** (rGO) is obtained by reducing graphene oxide (GO) .So some of the various methods of reducing Graphene oxide have been researched over the years are discussed. S.Stankovich et al. in **2007**[20] had successfully reduced graphite oxide using hydrazine hydrate as reducing agent. Shin et al. in **2009** [21] had proven the sheet resistance of graphite oxide film reduced using sodium borohydride ($NaBH_4$) is much lower than that of films reduced using hydrazine (N_2H_4). In **2011** Kim et al. [22] reported a simple, cost-effective, and environmentally benign process for reducing graphite oxide by treating solely with Sulfuric Acid. In **2015** Ghorbani et al. [23] sucessfully reduced GO to rGO hydrothermally is advantageous compared to conventional chemical reduction processes as hydrazine is toxic.

- Yamaguchi et al. in **2011** had studied on Point sources exhibit low threshold electron emission due to local field enhancement at the tip. The development and implementation of tip emitters have been hampered by the need to position them sufficiently apart to achieve field enhancement, limiting the number of emission sites and therefore the overall current. low threshold field (< 0.1 V/μm) emission of multiple electron beams from atomically thin edges of reduced graphene oxide (RGO)is reported. Field emission microscopy measurements show evidence for interference from emission sites that are separated by a few nano-meters, suggesting

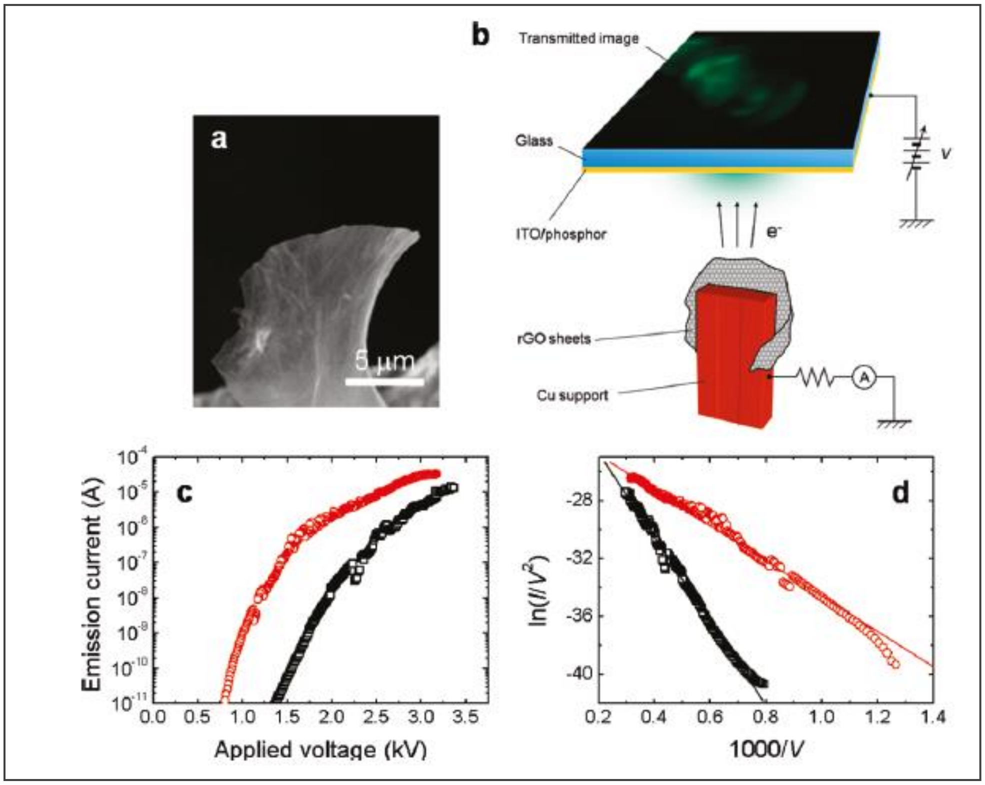

Figure 3. 2 Experimental setup of the field emission measurements. (a) Typical SEM image of rGO sheet mounted on a copper support bar. (b) Schematic of the FEM measurement setup. Voltages up to 4 kV were applied between the imaging anode and the cathode for FEM. For FIM, opposite bias is applied and helium ions (instead of electrons) produce the image on the screen. (c) IV field emission characteristics and corresponding (d) FN plot for rGO (red)and the multilayered (black) samples.[24]

that the emitted electron beams are coherent. Field emission from the RGO edge is attributed to a stable and unique aggregation of oxygen groups in the form of cyclic edge ethers. Such closely spaced electron beams from RGO offer prospects for novel applications and understanding the physics of linear electron sources to get enhanced Field Emission properties. The tunnelling of electrons from material surface to vacuum under the influence of external electric field through their sharp tips or in the case of thin films from edges or defects did occur.[24]

- The application of RGO towards the direction of Field Emission had been investigated by many research workers. Most of the cases the researchers prefer to make Graphene based nanocomposite material and several models. Roy et al. in **2013** they reported, top assembly of very thin layer of reduced graphene oxide (RGO) by Langmuir Blodgett method over a multi-walled carbon nanotubes (MWCNTs) thin film/ITO substrate to investigate the dual field emission property of the hybrid structure. The non-functionalized type of attachment in between the hybrid carbon nanostructures mainly due to van dar Waals force of attraction ensured easy fabrication procedure. Evidence of uniform distribution of web like networks of very thin transparent RGO sheets top assembled over densely packed MWCNTs thin film was found from the field emission scanning electron microscopy analysis. The base layer conductivity was enhanced due to the incorporation of MWCNTs bottom layer over ITO and the former also additionally facilitated as emitter site pockets in between RGO planes. This hybrid system a much feasible candidate for future field emission (FE) based device applications. = 50 $\mu A/cm^2$. The turn-on field at current density of 50 $\mu A/cm^2$.and β overall improved significantly in case of the MWCNT-RGO thin film ($E_{to} \sim 4.5$ V μm^{-1} and β ~3103)when compared with the pristine MWCNT thin film ($E_{to} \sim 5.2$ V μm^{-1} and β ~763), assuming the work function to be same as graphite ~5 eV for both materials for the calculation of β.[25]

- In **2013**, Devarapalli et al. observed highly efficient and stable field emission with low turn-on field for SiNW–GO heterostructures. The sharp protrusions created by stretching of the GO nanosheets on SiNWs locally enhanced the electric field and thus enhanced the field emission characteristics. The GO coated SiNWs showed a low turn-on value of 4.0 V/µm and a maximum current density of ~1.8 mA cm^{-2} at an applied electric field of 7.2 V/µm. The observed low turn-on field was associated with the enhancement in the β value of 2024 due to the atomically thick GO sheet which was higher than GO coated on Silicon substrate(β=823) and pristine silicon nanowires(β=1074) presented in the study.[26]

- Tang et al. in **2019** observed Graphene nanosheet (GNS) thin film was grown flat lying on Si nanoporous pillar array (Si-NPA) substrate using Ni nanocrystallites as catalyst by a chemical vapor deposition method, and its field electron emission characteristics were studied. For few-layer GNS/Si-NPA a turn-on field of ~2.85 V/µm, an emission current density of ~53.9 µA/cm^2 was obtained at an electric field of 4.2 V/µm and the enhancement factor was calculated to be ~2700 according to the Fowler–Nordheim theory. GNS/Si-NPA with multi-layer GNSs was prepared and its turn-on field was obtained at 8.5 V/µm. therefore it was observed that few-layer GNSs had lower turn-on field and higher emission current density than the multi-layer GNSs.[27]

Currently, a lot of research emphasis is going on to improve the field emission property through graphene and RGO due to its protruding edge effect of the sheet boundary peripheral region.[28] The presence of rich edges influences the electronic transport enabling easier tunnelling of electrons producing a lower barrier potential to eject electrons into vacuum. Graphene with its large lateral surface dimension, atomic thickness, high conductivity and good flexibility is expected to randomly align itself to the electric field direction under an applied field resulting in enhanced local field emission. In between RGO inter planes it can be assumed that they can act as additional pockets of secondary residual field emitting sites together making the whole system an even better field emitter under the influence of electric field. Hence, in the current context the main impetus has been given to study the behaviour of carbon nanostructure based crumpled network field emission. In a current work it has been demonstrated low threshold field emission from individual atomically thin reduced graphene oxide (RGO) sheets and show that it arises from a decrease in work function of the edge due to the creation of cyclic C-O-C[24] ether groups in combination with geometric field enhancement. Furthermore the emission sites from RGO are densely packed, located only a few nanometers apart.

Wettability of solid surfaces attracts many attentions both in research and practical applications and studies conducted on the superhydrophobic surfaces have grown dramatically. Surfaces with controllable wettability and adhesion behavior toward water droplets are widely studied because of their promising applications in self-cleaning, controllable oil/water separation, cell culture devices, deicing and microdroplet transportation.[29]

- Zhu et al. in **2006** described a method to control the wettability of a solid surface through fabricating a regular rough surface with a square pillar array by silicon micromachining and coating a hydrophobic layer. The measured results were compared with Wenzel's and Cassie's theories. The experimental results were closer to Cassie's theoretical predictions on the superhydrophobic surfaces than that by Wenzel's. In our experiment, the largest CA of 162° was observed. This method tuning surface wettability by controllable changing surface roughness can be also used to transport microdroplets. The spontaneous movement of a droplet has been observed qualitatively on a surface with a certain roughness spatial gradient.[30]

- In **2009**, Zhang et al. fabricated ordered silicon cone arrays (SCAs) of different morphologies using colloidal lithography by reactive ion etching, and their wettabilities have been investigated in detail. The surface roughness of the obtained silicon cone arrays can be adjusted by controlling the etching duration, which is proved to be of importance in tailoring the behavior of water droplets when being used as antireflection coatings with superhydrophobicity. On controlling the arrangement of colloidal spheres, silicon cone arrays with tunable periodicities, different lattice structures, and various patterns was prepared. The experiment results described above imply that the transformation of water droplets from isotropic dewetting to anisotropic dewetting is controllable by adjusting the strip width with and without silicon cones, which is helpful in the basic understanding of the influence of complex micro- and nanoscale roughness.[31]

- Ranella et al. in **2010,** fabricated laser structured Si micro and nano rough spike scaffolds with controllability of roughness ratio and surface chemistry which can serve as a novel means to elucidate the 3D cell–biomaterials interactions in vivo. It was demonstrated that the wettability of such artificial substrates can be preferentially tuned from super-hydrophobic to super-hydrophilic through independently controlling roughness ratio and surface chemistry. The dependency of fibroblast cell response on the artificial structures was systematically investigated and clarified that a fundamental parameter that determines cell adhesion on 3D substrates is not solely the degree of roughness or surface chemistry but the combination of both, which determines the wettability or surface energy of the substrate. Indeed, a proper change in the surface energy for the same degree of roughness can switch the behaviour from cell-phobic to cell-philic and vice versa and transition is always accompanied by a similar sharp transition in surface wettability. Although it appeared to be a general tendency that adhesion is favoured on hydrophilic substrates, it is observed that cells' spreading becomes optimum on low-rough substrates, independently of their wettability. This indicates that cell attachment is further enhanced and facilitated by a proper form and size of surface topography.[32]

- A new technique to directly grow Cu nanowire (CuNW) on Si substrate with electro-chemical deposition to produce height-controlled hydrophilic nanowired surfaces for enhancing poolboiling performance was developed by Yao et al. in **2011.** For broader heat transfer applications, CuNW and Si nanowires (SiNWs) with various nanowire heights were fabricated and examined under pool boiling with water. Both Cu and Si nanostructured surfaces demonstrated hydrophilic properties. Their contact angles are 28° and 0° respectively. As the contact angle of water on the plain Si and Cu surfaces are hydrophilic, the surfaces with nanowire structures become more hydrophilic. The hydrophilic surface is preferred in pool boiling as it can promote bubble nucleation and increase the critical heat flux by preventing dry out. At the same time, the availability of larger cavities with taller micro/nanostructures allow the onset of nucleate boiling at lower wall superheats.[33]

- In **2011**, Kim et al. synthesized micro-nano hybrid structures (MNHS) of silicon with hierarchical geometries that lead to maximizing of surface area, roughness, and wettability are developed for the boiling applications. MNHS is fabricated by a two-step silicon etching process, which are dry etching for micropattern and electroless silicon wet etching for nanowire synthesis having high aspect ratio. The fabrication process is readily capable of producing MNHS covering a wafer-scale area. By controlling the removal of polymeric passivation layers deposited during silicon dry etching (Bosch process), the geometries for the hierarchical structure can be controlled with or without the thin hydrophobic barriers that affect surface wettability. MNHS without sidewalls exhibited superhydrophilic behavior with a contact angle under 10°, whereas those with sidewalls preserved by the passivation layer display more hydrophobic characteristics with a contact angle near 60°.[34]

- Dawood et al. in **2011**, fabricated large-area, highly scalable ,hybrid superhydrophobic surfaces on silicon (Si) substrates with tunable, spatially selective adhesion behavior by controlling the morphologies of Si nanowire arrays. Au nanoparticles were deposited on Si by glancing angle deposition, followed by metal-assisted chemical etching of Si to form Si nanowire arrays and then chemically modified and rendered hydrophobic by fluorosilane deposition. The difference in nanowire morphology is attributed to capillary force-induced nanocohesion, which is due to the difference in nanowire porosity. The clumped nanowire surface demonstrated the lotus effect, and the straighter nanowires demonstrated the ability to pin water droplets while maintaining large contact angles (i.e., the petal effect). The high contact angles in both cases are explained by invoking the Cassie-Baxter wetting state. The high adhesion behavior of the straight nanowire surface may be explained by a combination of attractive van der Waals forces and capillary adhesion.[35]

- In **2013,** Coffinier et al. studied the wetting properties of silicon-based materials as a function of their roughness and chemical composition. The investigated surfaces consist of hydrogen terminated and chemically modified atomically flat crystalline silicon, porous silicon and silicon nanowires. The combination of high surface roughness with chemical functionalization with water repellent coating (1-octadecene) enables reaching superhydrophobicity (water contact angle greater than 150°) for silicon nanowires. Control of surface wettability of silicon-based substrates was achieved through the combination of surface roughness and chemical functionalization. The increase of surface roughness combined with coating with low surface energy induced by surface modification which ensured air trapping between the substrate and the liquid droplets, necessary to achieve superhydrophobicity. [36]

- Meng et al.in **2016**, employed a facile and controllable approach to fabricate a superwetting tilted silicon nanowires (TSNWs) surface through metal-assisted chemical etching and modified it with low-surface-energy material.The contact angle (CA) measurements of the nanostructured surface show a large range from the superhydrophilicity (the CA approximate to 0°) to superhydrophobicity (the CA up to 160°). The surface becomes antiadhesive to water upon nanostructuring with a measured sliding angle close to 0°. Moreover, the fluorinated TSNWs surface exhibits excellent stability and durability because strong chemical bonding has been formed on the surface.[37]

References :

[1] R. S. Wagner and W. C. Ellis "Vapor-Liquid-Solid Mechanism Of Single Crystal Growth" Applied Physics Letters, Volume 4, Number 5(1964): 89-90

[2] D. Dimova-Malinovska, M. Sendova-Vassileva, N. Tzenov, M. Kamenova. "Preparation of thin porous silicon layers by stain etching" Thin Solid Films 297 (1997) 9–12

[3] X. Li and P. W. Bohn “Metal-assisted chemical etching in HF/H_2O_2 produces porous silicon” Applied Physics Letters, Volume 77, Number 16, (2000): 2572-2574

[4] Zhipeng Huang ,Nadine Geyer ,Peter Werner , Johannes de Boor , and Ulrich Gösele "Metal-Assisted Chemical Etching of Silicon: A Review" Adv. Mater. 2011, 23, 285–308

[5] Frederick C. K. Au, K. W. Wong, Y. H. Tang, Y. F. Zhang, I. Bello, and S. T. Lee "Electron field emission from silicon nanowires" Applied Physics Letters Volume 75, Number 12 (1999):1700-1722

[6] M. Lu, M.K. Li , L.B. Kong , X.Y. Guo , H.L. Li " Silicon quantum-wires arrays synthesized by chemical vapor deposition and its micro-structural properties" Chemical Physics Letters 374 (2003) 542–547

[7] Y. L. Chueh, L. J. Chou, S. L. Cheng, J. H. He, W. W. Wu, and L. J. Chen "Synthesis of taperlike Si nanowires with strong field emission" Applied Physics Letters 86, (2005) 133112

[8] N. N. Kulkarni, J. Bae, C.K. Shih, S. K. Stanley, S. S. Coffee, and J. G. Ekerdt "Low-threshold field emission from cesiated silicon nanowires" Applied Physics Letters 87, (2005) 213115

[9] J. C. She, S. Z. Deng, N. S. Xu, R. H. Yao, and J. Chen "Fabrication of vertically aligned Si nanowires and their application in a gated field emission device" Applied Physics Letters 88,(2006) 013112

[10] D. McClain, L. F. Dong, R. Solanki, and J. Jiao, “Synthesis of single crystalline silicon nanowires and investigation of their electron field emission”, J. Vac. Sci. Technol. B 24, (2006).20-24

[11] Baoqing Zeng, Guangyong Xiong, Shuo Chen, S. H. Jo, W. Z. Wang, D. Z. Wang, and Z. F. Ren "Field emission of silicon nanowires" Applied Physics Letters 88,(2007) 213108

[12] Baoqing Zeng, Guangyong Xiong, Shuo Chen, Wenzhong Wang, D. Z. Wang, and Z. F. Ren " Field emission of silicon nanowires grown on carbon cloth" Applied Physics Letters 90,(2007) 033112

[13] Xiaosheng Fang, Yoshio Bando, Changhui Ye, Guozhen Shen, Ujjal K. Gautam, Chengchun Tang and Dmitri Golberg "Si nanowire semisphere-like ensembles as field emitters" Chem. Commun.(2007) 4093–4095

[14] Hsin-Luen Tsai "Characteristics of Silicon Nanowire Field Electron Emission" Advanced Materials Research Vols. 652-654

[15] Shasha Lv, Zhengcao Li, Shiming Su, Linhan Lin, Zhengjun Zhang, Wei Miao "Tunable Field Emission Properties of Well-aligned Silicon Nanowires with Controlled Aspect Ratio and Proximity" RSC Advances, (2014) 00, 1-3

[16] Goki Eda, Giovanni Fanchini And Manish Chhowalla "Large-area ultrathin films of reducedgraphene oxide as a transparent and flexible electronic material" Nature Nanotechnology Vol 3 May (2008) 270-274

[17] Brodie, B. C. "On the Atomic Weight of Graphite." Philos Trans R Soc London 14, 249–259 (1859).

[18] Williams, Hummers Jr , And Richard E . Offeman "Preparation of Graphitic Oxide" Journal of the American Chemical Society , 80 (6), (1958) 1339–1339

[19] Leila Shahriary, Anjali A. Athawale." Graphene Oxide Synthesized by using Modified Hummers Approach" International Journal of Renewable Energy and Environmental Engineering ISSN 2348-0157, Vol. 02, No. 01, (2014)

[20] Stankovich S, Dikin DA, Piner RD, KohlhaasKA,Kleinhammes A, Jia Y, et al., “Synthesis of graphene-based nanosheets via chemical reduction of exfoliated graphite oxide.”Carbon.45(7): (2007).1558–65

[21] Shin H-J, Kim KK, Benayad A, Yoon S-M, Park HK, Jung I-S etal. “Efficient reduction of graphite oxide by sodiumborohydride and its effect on electrical conductance.” Adv.Func.Mater. 19(12):1987–92.(2009).

[22] Dohyung Kim, Seung Jae Yang, YernSeung Kim, Haesol Jung, Chong Rae Park " Simple and cost-effective reduction of graphite oxide by sulfuric acid." Carbon 50 (2012) 3229 –3232

[23] M. Ghorbani, H.Abdizadeh, M. R. Golobostanfard "Reduction of Graphene Oxide via Modified Hydrothermal Method" Procedia Materials Science 11 (2015) 326 – 330

[24] Hisato Yamaguchi, Katsuhisa Murakami, X GokiEda, Takeshi Fujita, Pengfei Guan, WeichaoWang, Cheng Gong, JulienBoisse, Steve Miller, MugeAcik, KyeongjaeCho, Yves J.Chabal, Mingwei Chen, FujioWakaya, MikioTakai and Manish Chhowalla. "Field Emission from Atomically Thin Edges of Reduced Graphene Oxide" ACS Nano, 5 (6), 2011, 4945–4952

[25] Rajarshi Roy, Arunava Jha, Kalyan K. Chattopadhyay. "Chemically derived graphene sheets top assembled over multi-walled carbon nanotube thin film by Langmuir Blodgett method for improved dual field emission" Journal of Nanoscience and Nanotechnology Vol. 13, (2013)452–460.

[26] Rami Reddy Devarapalli, Ranjit V. Kashid, Ashvini B. Deshmukh, Ponchami Sharma, Manash R. Das, Mahendra A. More and Manjusha V. Shelke " High effciency electron field emission from protruded graphene oxide nanosheets supported on sharp silicon nanowires" Journal of Materials Chemistry C, (2013), 1, 5040–5046.

[27] Zhaojun Tang, Sen Li, Zheng Zhu, Xinjian Li" Electron field emission from graphene nanosheets grown on Si nanoporous pillar array" Materials Science in Semiconductor Processing 89 (2019) 105–109

[28] Rajarshi Roy, Arunava Jha, Diptonil Banerjee, Nirmalya Sankar Das, and Kalyan Kumar Chattopadhyay " Edge effect enhanced electron field emission in top assembled

reduced graphene oxide assisted by amorphous CNT-coated carbon cloth substrate." AIP Advances 3, 012115 (2013)

[29] Guomin Ding, Weicheng Jiao, Rongguo wang, Zhenming Chu and Yifan Huang " An underwater, self-sensing, conductive composite coating with controllable wettability and adhesion behavior" Journal of Materials Chemistry A(2019)

[30] Liang Zhu, Yanying Feng , Xiongying Ye, Zhaoying Zhou " Tuning wettability and getting superhydrophobic surface by controlling surface roughness with well-designed microstructures" Sensors and Actuators A 130–131 (2006) 595–600

[31] Xuemin Zhang, Junhu Zhang, Zhiyu Ren, Xiao Li, Xun Zhang, Difu Zhu Tieqiang Wang, Tian Tian, and Bai Yang “Morphology and Wettability Control of Silicon Cone Arrays Using Colloidal Lithography” Langmuir 2009, 25(13), 7375–7382

[32] A. Ranella , M. Barberoglou , S. Bakogianni , C. Fotakis , E. Stratakis " Tuning cell adhesion by controlling the roughness and wettability of 3D micro/nano silicon structures " Acta Biomaterialia 6 (2010) 2711–2720

[33] Z. Yao, Y.W. Lu , S.G. Kandlikar "Effects of nanowire height on pool boiling performance of water on silicon chips" International Journal of Thermal Sciences 50 (2011) 2084-2090

[34] Beom Seok Kim, Sangwoo Shin, Seung Jae Shin, Kyung Min Kim and Hyung Hee Cho "Micro-nano hybrid structures with manipulated wettability using a two-step silicon etching on a large area" Nanoscale Research Letters (2011), 6:333

[35] M. K. Dawood, H. Zheng, T. H. Liew K. C. Leong Y. L. Foo W. K. Choi R. Rajagopalan and S. A. Khan "Mimicking Both Petal and Lotus Effects on a Single Silicon Substrate by Tuning the Wettability of Nanostructured Surfaces" Langmuir 2011, 27, 4126–4133

[36] Y. Coffinier, G. Piret, M.R. Das, R. Boukherroub, “Effect of surface roughness and chemical composition on the wetting properties of silicon-based substrates.” C. R. Chim. 16(1), 65–72 (2013).

[37] Xiangman Meng . Ailin Zhou . Bo Wang . Yu Chen . Yun-Hui Tang . Hui Yan " Stable Superwetting Surface Prepared with Tilted Silicon Nanowires" Nano-Micro Lett. DOI:10.1007/s40820-016-0100-x

Chapter4

Instruments

In this chapter, major apparatus and instruments , which were used while characterization of the samples have been discussed . A brief description about the working principle of the instruments has also been given.

4.1 Morphological Analysis:

4.1.1 Field Emission Scanning Electron Microscopy (FESEM):

The scanning electron microscope (SEM) is one of the most versatile instruments available for the examination and analysis of the microstructure morphology. SEM utilizes a focused electron beam to scan across the surface of the specimen systematically, producing large numbers of signals. These electron signals are eventually converted to a visual signal displayed on a cathode ray tube (CRT). The electron beam can be generated by two ways:

a) Thermionic emission; b) Field emission.

The thermionic emission is by controlling the electron emission from the source using thermal energy. For modern electron microscopes, field emission electron guns (FEG) are a good alternative for thermionic electron guns. A FESEM is used to visualize very small topographic details (~ 5□m) on the surface or entire or fractioned objects. Researchers in biology, chemistry and physics apply this technique to observe structures that may be a small as 1 nanometre (= billion of a millimetre). The FESEM may be employed for example to study organelles and DNA material in cells, synthetically polymers, and coatings on microchips.

- **Sample Preparation**

Since the SEM is operated under high vacuum the specimens that can be studied must be compatible with high vacuum (~ 10^{-5} mbar). This means that liquids and materials containing water and other volatile components cannot be studied directly. Also fine powder samples need to be fixed firmly to a specimen holder substrate so that they will not contaminate the SEM specimen chamber. Nonconductive materials need to be attached to a conductive specimen holder and coated with a thin conductive film by sputtering or evaporation. Typical coating materials are Au, Pt, Pd, their alloys, as well as carbon.

- **Components of FESEM**

- **Electron Guns**

Modern SEM systems require that the electron gun produces a stable electron beam with high current, small spot size, adjustable energy, and small energy dispersion. Several types of electron guns are used in SEM system and the qualities of electrons beam they produced vary considerably. The first SEM systems generally used tungsten “hairpin” or lanthanum hexaboride (LaB_6) cathodes, but for the modern SEMs, the trend is to use field emission sources, which provide enhanced current and lower energy dispersion. Emitter lifetime is another important consideration for selection of electron sources.

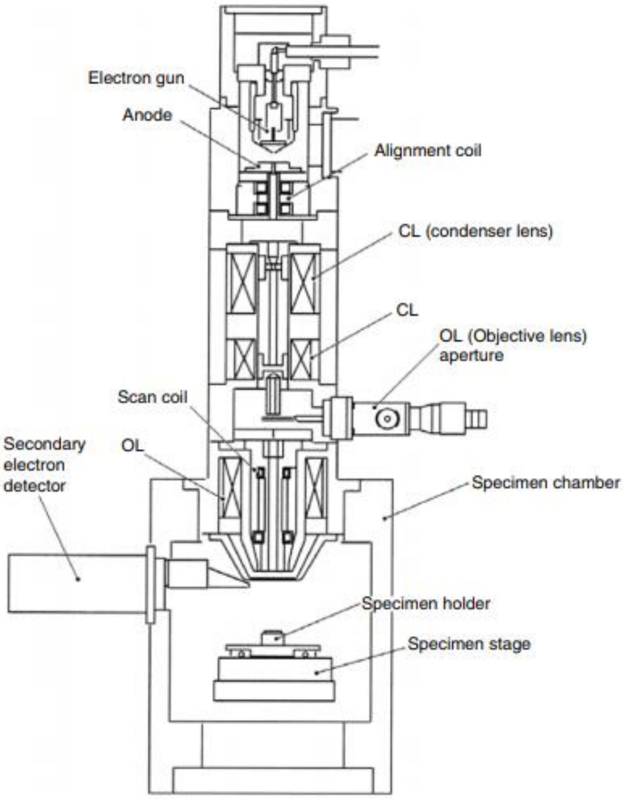

Figure 4. 1 Schematic Diagram of FESEM

- **Electron Lenses**

Electron beams can be focused by electrostatic or magnetic field. But electron beam controlled by magnetic field has smaller aberration, so only magnetic field is employed in SEM system. The trajectories of the electrons can be adjusted by the electromagnets.

  - **Condenser lens:**

The electron beam will diverge after passing through the anode plate from the emission source. By using the condenser lens, the electron beam is converged and collimated into a relatively parallel stream. A magnetic lens generally consists of two rotationally symmetric iron pole pieces in which there is a copper winding providing magnetic field. There is a hole in the center of pole pieces that allows the electron beam to pass through. A lens-gap separates the two pole pieces, at which the magnetic field affects (focuses) the electron beam. The position of the focal point can be controlled by adjusting the condenser lens current.

  - **Scan Coils**

The scan coils deflect the electron beam over the object according to a zigzag pattern. The formation of the image on the monitor occurs in synchrony with this scan movement. The scan velocity determines the refreshing rate on the screen and the amount of noise in the image. Scan coils often consist of upper and lower coils, which prevent the formation of a circular shadow at low magnification.

  - **The Objective Lens**

The electron beam will diverge below the condenser aperture. Objective lenses are used to focus the electron beam into a probe point at the specimen surface and to supply further demagnification. An appropriate choice of lens demagnification 1. Fundamentals of Scanning Electron Microscopy 15 and aperture size results in a reduction of the diameter of electron beam on the specimen surface (spot size), and enhances the image resolution.

- **The Stigmator Coil**

The stigmator coils are utilized to correct irregularities in the x and y deflection of the beam and thus to obtain a perfectly round-shaped beam. When the beam is not circular, but ellipsoidal, the image looks blurred and stretched.

- **Object Chamber**

After the object has been covered by a conductive layer it is mounted on a special holder. The object is inserted through an exchange chamber into the high vacuum part of the microscope and anchored on a moveable stage. The secondary electron emission detector (scintillator) is located at the rear of the object holder in the chamber.

Figure 4. 2 FESEM (Hitachi S-4800) set up

- Image Formation

Complex interactions occur when the electron beam in an SEM impinges on the specimen surface and excites various signals for SEM observation. The secondary electrons, BSEs(back scattered electrons), transmitted electrons, or the specimen current might all be collected and displayed. For gathering the information about the composition of the specimen, the excited x-ray or Auger electrons are analyzed. In this section, we will give a brief introduction about the interactions of the electron beam with the specimen surface and the principle of image formation by different signals.

4.1.2 Energy Dispersive X-Ray Spectroscopy (EDS/EDX)

Energy Dispersive X-Ray Analysis (EDX), referred to as EDS or EDAX, is an x-ray technique used to identify the elemental composition of materials. EDX systems are attachments to Electron Microscopy instruments (Scanning Electron Microscopy (SEM)) where the imaging capability of the microscope identifies the specimen of interest. The data generated by EDX analysis consist of spectra showing peaks corresponding to the elements making up the true composition of the sample being analysed. Elemental mapping of a sample and image analysis are also possible.

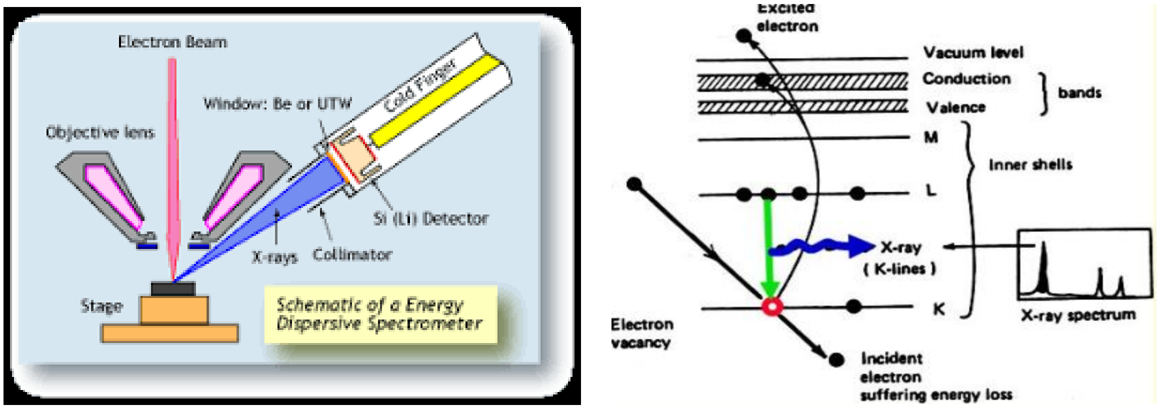

Figure 4. 3 Schematic Diagram of EDS

4.1.3 High Resolution Transmission Electron Microscopy (HRTEM):

Transmission electron microscope (TEM) is is an analytical tool allowing visualisation and analysis of specimens in the realms of microspace (1 micron/1□m =10^{-6}m) to nanospace (1 nanometer/nm =10^{-9}m). A beam of electrons is transmitted through an ultrathin specimen, interacting with the specimen as it passes through. An image is formed from the interaction of the electrons transmitted through the specimen; the image is magnified and focused onto an imaging device, such as a fluorescent screen, on a layer of photographic film, or to be detected by a sensor such as a CCD camera. TEMs are capable of imaging at a significantly higher resolution than light microscopes, owing to the small de Broglie wavelength of electrons.

Working Principle

- The "Virtual Source" at the top represents the electron gun, producing a stream of monochromatic electrons.
- This stream is focused to a small, thin, coherent beam by the use of condenser lenses 1 and 2. The first lens (usually controlled by the "spot size knob") largely determines the "spot size"; the general size range of the final spot that strikes the sample. The second lens (usually controlled by the "intensity or brightness knob" actually changes the size of the spot on the sample; changing it from a wide dispersed spot to a pinpoint beam.
- The beam is restricted by the condenser aperture (usually user selectable), knocking out high angle electrons (those far from the optic axis, the dotted line down the centre).
- The beam strikes the specimen and parts of it are transmitted.
- This transmitted portion is focused by the objective lens into an image.
- Optional Objective and Selected Area metal apertures can restrict the beam; the Objective

aperture enhancing contrast by blocking out high-angle diffracted electrons, the Selected Area aperture enabling the user to examine the periodic diffraction of electrons by ordered arrangements of atoms in the sample.

- The image is passed down the column through the intermediate and projector lenses, being enlarged all the way.
- The image strikes the phosphor image screen and light is generated, allowing the user to see the image.

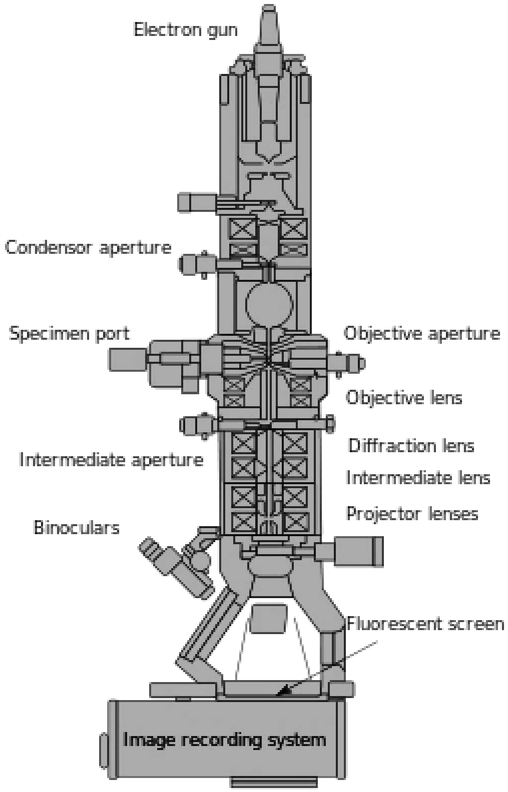

Figure 4. 4 Schematic diagram of TEM

- ➢ Restriction on samples

Sample preparation for TEM generally requires more time and experience than for most other characterization techniques. A TEM specimen must be approximately 1000 A^o or less in thickness in the area of interest. The entire specimen must fit into a 3 mm diameter up and be less than about 100 microns in thickness. A thin, disc shaped sample with a hole in the middle, the edges of the hole being thin enough for TEM viewing, is typical. The initial disk is usually formed by cutting and grinding from bulk or thin film/substrate material, and the final thinning done by ion milling. Other specimen preparation possibilities include direct deposition onto a TEM-thin substrate (Si_3N_4, carbon); direct dispersion of powders on such a substrate; grinding and polishing using special devices like tripod; chemical etching and electro-polishing; and lithographic patterning of walls and pillars for cross-section viewing.

Figure 4. 5 HRTEM (JEOL-200 kV)

4.2 Crystal Structure Analysis:

4.2.1 X-Ray Diffractometer (XRD):

X-rays were discovered by Wilhelm Conrad Röntgen in 1895, just as the studies of crystal symmetry were being concluded. Physicists were initially uncertain of the nature of X-rays, although it was soon suspected (correctly) that they were waves of electromagnetic radiation, in other words, another form of light. The atomic planes of a crystal cause an incident beam of X-rays to interfere with one another as they leave the crystal. The phenomenon is called X- ray diffraction. X-ray diffraction has been in use in two main areas, for the fingerprint characterization of crystalline materials and the determination of their structure. Each crystalline solid has its unique characteristic X-ray powder pattern which may be used as a "fingerprint" for its identification. Once the material has been identified, X-ray crystallography may be used to determine its structure, i.e. how the atoms pack together in the crystalline state and what the interatomic distance and angle are etc. X-ray diffraction is one of the most important characterization tools used in solid state chemistry and materials science. We can determine the size and the shape of the unit cell for any compound most easily using X-ray diffraction.

- **X-Ray Generation:**

X-rays are produced by bombarding a metal target (Cu, Mo usually) with high-energy electrons from a hot filament (often tungsten). The high energy electron must penetrate through the outer electron shells and interact with the inner-shell electrons. If more than a critical amount of energy is transferred to an inner-shell electron, that electron is ejected; i.e. it escapes the attractive field of the nucleus, leaving a hole in the inner shell and generates ionized one from the outer shells. It is this transition which is accompanied either by the emission of an X-ray or an Auger atoms. The ionized atom returns almost to its lowest energy by filling in the missing electron with electron.

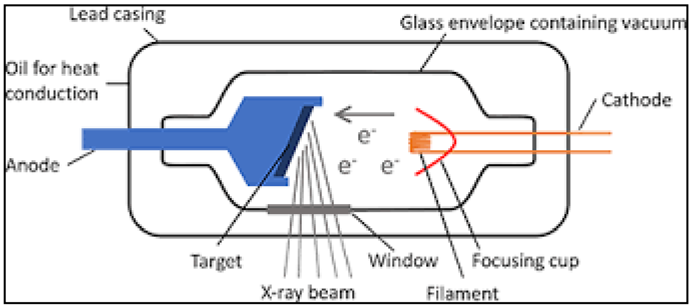

Figure 4. 6 X ray generation principle

- **Basic Principle:**

X-rays are electromagnetic radiation with wavelength of the order of 0.01 to 10 nm. . Crystals are regular arrays of atoms, and X-rays can be considered waves of electromagnetic radiation. Atoms scatter X-ray waves, primarily through the atoms' electrons. Just as an ocean wave striking a lighthouse produces secondary circular waves emanating from the lighthouse, so an X-ray striking an electron produces secondary spherical waves emanating from the electron. This phenomenon is known as elastic scattering, and the electron (or lighthouse) is known as the scatterer. A regular array of scatterers produces a regular array of spherical waves.

- **Measurement of Interplanar Spacing:**

The basic law involved in the diffraction method of structural analysis is the Bragg's law. The diffraction traces were recorded in θ-2θ mode. When monochromatic X-rays impinge upon the atoms in a crystal lattice, each atom acts as a source of scattering. The crystal lattice acts as series of parallel reflecting planes. The intensity of the reflected beam at certain angles will be maximum when the path difference between two reflected waves from two different planes is an integral multiple of λ. This condition is called Bragg's law and is given by the relation,

$$2d \sin\theta = n\lambda$$

Where n is the order of diffraction, λ is the wavelength of the x-rays, d is the spacing between consecutive parallel planes and θ is the incident angle.

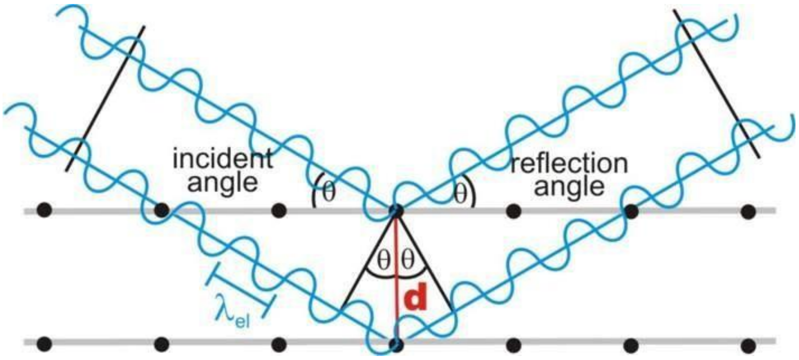

Figure 4. 7 X-ray diffraction from crystal planes satisfying Bragg's Law.

- **Crystallite size determination:**

The mean crystallite sizes of the powders are calculated using Scherrer formula:

$$D = \frac{0.9\,\lambda}{\beta\cos\theta}$$

Where D is the average crystallite size, λ =1.541 A° (X-ray wavelength), β is the full width of the diffraction peak at half maximum (FWHM) for the diffraction angle 2θ.

- **Phase identification:**

After above determination the generated XRD pattern is matched with the JCPDS card no. stored in JCPDS file. There are various JCPDS card for every organic inorganic element. Among those suitable cards is compared with the obtained pattern. Phase identification of the synthesized samples were carried out by x-ray diffraction (XRD) using a D8 Advanced Bruker instrument. XRD pattern was recorded in intensity vs 2θ mode. Germanium monochromator was used for Cu Kα (1.5406 Å) radiation from a highly stabilized Bruker X- ray generator (K 780).

Method	Wave Length (λ)	Incident Angle (θ)
Laue Method	Variable	**Fixed**
Rotating Crystal Method	Fixed	**Variable (In part)**
Power Method	**Fixed**	**Variable**

4.3 Bond Structure Analysis

4.3.1 Fourier Transform Infrared Spectroscopy (FTIR):

Fourier Transform Infrared Spectroscopy (FTIR) is a technique which is used to analyze the chemical composition of many organic compounds, polymers, paints, coatings, adhesives, lubricants, semiconductor materials, coolants, gases, biological samples, inorganics and minerals. FTIR can be used to analyze a wide range of materials in bulk or thin films, liquids, solids, pastes, powders, fibers, and other forms. FTIR analysis can give not only qualitative (identification) analysis of materials, but with relevant standards, can be used for quantitative (amount) analysis. An FTIR (Fourier Transform Infra-Red) is a method of obtaining infrared spectra by first collecting an interferogram of a sample signal using an interferometer, and then performing a Fourier Transform (FT) on the interferogram to obtain the spectrum. An FTIR Spectrometer collects and digitizes the interferogram, performs the FT function, and displays the spectrum.

An FTIR is typically based on a Michelson Interferometer the interferometer consists of a beam splitter, a fixed mirror, and a mirror that translates back and forth, very precisely. The beam splitter is made of a special material that transmits half of the radiation striking it and reflects the other half. Radiation from the source strikes the beam splitter and separates into two beams. One beam is transmitted through the beam splitter to the fixed mirror and the second is reflected off the beam splitter to the moving mirror. The fixed and moving mirrors reflect the radiation back to the beam splitter. Again, half of this reflected radiation is transmitted and half is reflected at the beam splitter, resulting in one beam passing to the detector and the second back to the source.

Components of Interferometer:

Different FTIR spectrometers use different interferometers, such as the Michelson interferometer, lamellar grating interferometer, and Fabry-Perot interferometer. The Michelson interferometer is often favored over the other two interferometers because of its easy construction and operation. Most of the commercially available FTIR spectrometers use the Michelson interferometer. These have a number of advantages over the other techniques, such as high energy throughput, multiplexing, and high precision in frequency measurement.

The basic Michelson Interferometer consists of following components:

(a) a broad-band light source which emits light covering the mid-IR range,

(b) a beam splitter made of KBr or CsI,

(c) Two front surface coated mirrors: one moving and one fixed, and

(d) a detector.

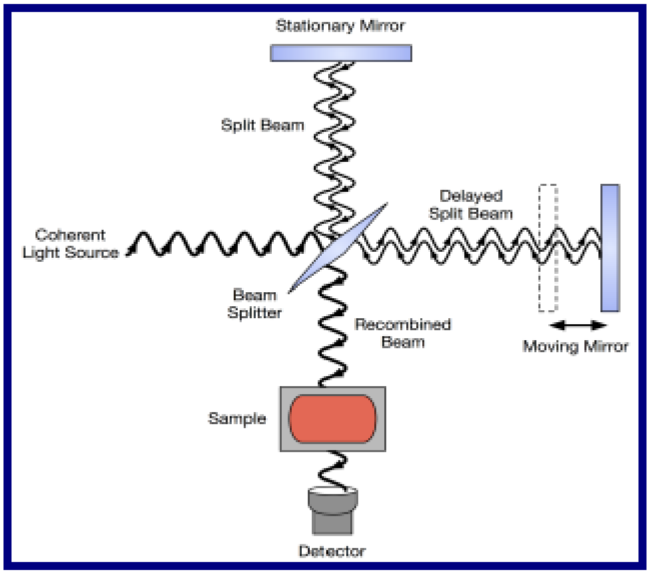

Figure 4. 8 schematic diagram of an FTIR

- **Working principle of interferometer:**

- Light from the light source is directed to the beam splitter. Half of the light is reflected and half is transmitted.
- The reflected light goes to the stationary mirror where it is reflected back to the beamsplitter. The transmitted light is sent to the moving mirror and is also reflected back towards the beam splitter.

At the beam splitter, each of the two beams from the stationary and moving mirrors are splitted into two: one goes back to the source (and “lost” since it does not reach the detector) and the other goes towards the detector. Hence the detector sees two beams: one from the moving mirror and the other from the stationary mirror.

The two beams reaching the detector come from the same source and have an optical path difference determined by the positions of the two mirrors, i.e. they have a fixed phase difference. Therefore the two beams interfere.

The two beams may be made to interfere constructively or destructively for a particular frequency by positioning the moving mirror. If the moving mirror is scanned over a range, interferogram is generated with its maximum intensity corresponding to constructive interference and the minimum intensity corresponding to destructive interference.

Figure 4. 9 FTIR spectrometer experimental set up

4.3.2 Raman Spectroscopy:

Raman scattering was first observed by Dr. C. V. Raman in 1928 and was used to investigate the vibrational states of many molecules. In Raman Spectroscopy technique is based on the principle of inelastic scattering of monochromatic light on the sample. A laser beam is used as the monochromatic light to irradiate a spot on the sample under investigation. Inelastic scattering deals with the phenomenon in which frequency of photons in monochromatic light changes upon interaction with a sample. Frequency of the reemitted photons is shifted up or down in comparison with original monochromatic frequency, which is called the Raman Effect. The scattered radiation produced by the Raman Effect contains information about the energies of molecular vibrations and rotations, and these depend on the particular atoms or ions that comprise the molecule, the chemical bonds connect them, the symmetry of their molecule structure, and the physico-chemical environment where they reside. Raman spectroscopy can be used to study solid, liquid and gaseous samples.

- **Working principle :**

When a sample is irradiated with an intense monochromatic light source (usually a laser), most of the radiation is scattered by the sample and the same wavelength as that of the incoming laser radiation in a process known as Rayleigh scattering. However, a small proportion of the incoming light approximately one photon out of a million is scattered at a wavelength that is shifted from the original laser wavelength.

The Raman effect is based on molecular deformations in electric field E determined by molecular polarizability α. The laser beam can be considered as an oscillating electromagnetic wave with electrical vector E. Upon interaction with the sample it induces electric dipole moment $P = \alpha E$ which deforms molecules. Because of periodical deformation, molecules start vibrating with characteristic frequency υ_m amplitude of vibration is called a nuclear displacement. In other words, monochromatic laser light with frequency υ_0 excites molecules and transforms them into oscillating dipoles.

Depending upon the change of frequency of the scattered light Raman Scattering phenomenon can be classified as:

- **Rayleigh scattering -** A molecule with no Raman-active modes absorbs a photon with the frequency υ_0. The excited molecule returns back to the same basic vibrational state and emits light with the same frequency υ_0 as an excitation source. This type of interaction is called an elastic Rayleigh scattering.
- **Stokes** - A photon with frequency υ_0 is absorbed by Raman-active molecule which at the time of interaction is in the basic vibrational state. Part of the photon's energy is transferred to the Raman-active mode with frequency υm and the resulting frequency of scattered light is reduced to υ_0 - υ_m. This Raman frequency is called Stokes frequency, or just "Stokes".
- **Anti-Stokes -** A photon with frequency υ0 is absorbed by a Raman-active molecule, which, at the time of interaction, is already in the excited vibrational state. Excessive energy of excited Raman active mode is released, molecule returns to the basic vibrational state and the resulting frequency of scattered light goes up to $\upsilon_0 + \upsilon_m$. This Raman frequency is called Anti-Stokes frequency, or just "Anti-Stokes".

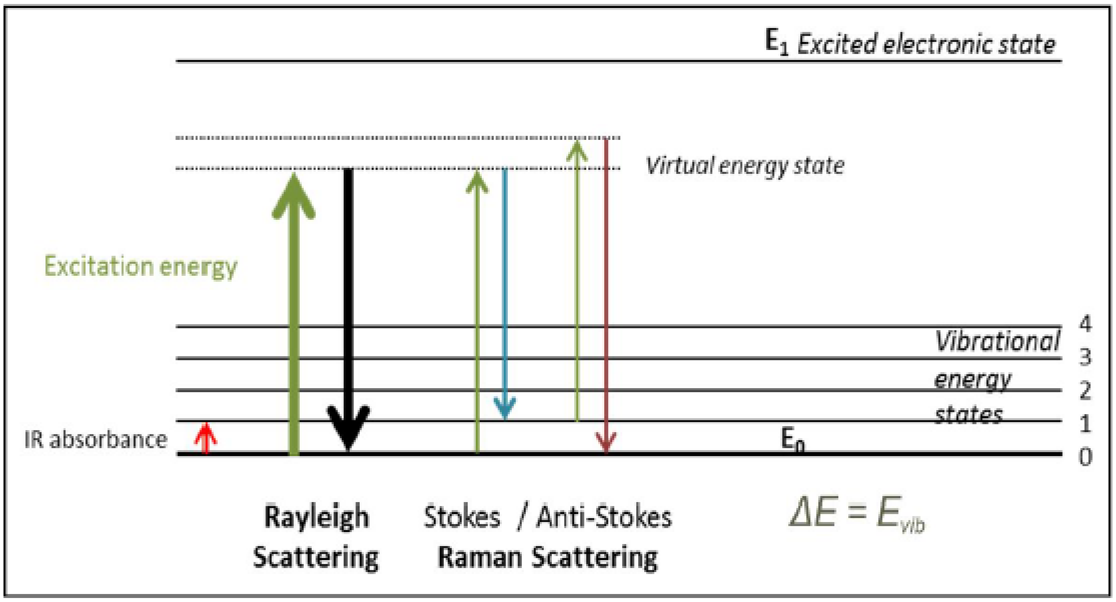

Figure 4. 10 Different scatterings of RAMAN Spectra

- **Components of Raman spectroscope :**

Raman Spectrometer consists of the following components,

1. Monochromatic source

A sample is normally illuminated with a laser beam in the ultraviolet (UV), visible (Vis) or near infrared (NIR) range. Scattered light is collected with a lens and is sent through interference filter or spectrophotometer to obtain Raman spectrum of a sample. Sample illumination and light collection (probe). The probe is a collection device that collects the scattered photons, filters out the Rayleigh scatter and any background signal from the fiber optic cables, and sends the scattered light to the spectrograph. Many probes also focus and deliver the incident laser beam.

2. Wavelength selector (Filter or Spectrophotometer)

When Raman-scattered photons enter the spectrograph, they are passed through a transmission grating to separate them by wavelength and are passed to a detector. The same transitions between molecular vibrational states (M) and (M*) in the infrared absorption can also result in Raman scattering. A key difference between the Raman and infrared processes is that, in the former process, the photons involved are not absorbed or emitted but rather shifted in frequency by an amount corresponding to the energy of the particular vibrational transition.

3. Detector (Photodiode array, CCD or PMT)

Optical multichannel analyzer, PMT, intensified photo array, a charged coupled device(CCD) records the intensity of the Raman signal at each wavelength. This data is represented as a Raman spectrum. The monochromatic light from a laser passes through focusing optics and a beam splitter to the sample. The scattered light passes through the beam splitter to a detector. The laser light illuminates the sample through a microscope objective (magnification from 100x to 1000x, typically), which is used both for the illumination (laser beam coming from the laser through mirrors and/or optical fibre) and collection of the scattered light. The scattered light goes to the CCD detector via two steps, the first one to suppress the Rayleigh scattering and the second one to split the selected spectral window on the CCD array in order to be able to see all the spectral components. A computer is used to scan, collect, and process the data creating a graph showing the intensity of light at each wavelength. The change in energy is observed as a change in frequency of the incident beam upon scattering.

4.4 Optical Property Analysis:

4.4.1 UV-VIS near Infrared Spectroscopy:

UV-Vis near Infrared (UV-Vis-NIR) Spectrophotometer measures Optical transmittance, absorbance and reflectance in the ultraviolet-visible spectral region. UV-Vis near Infrared (UV-Vis-NIR) Spectrophotometer measures Optical transmittance, absorbance and reflectance in the ultraviolet-visible spectral region**.** UV-Vis absorption spectroscopy measures the percentage of radiation that is absorbed or transmitted or reflected at each wavelength. Typically, this is done by scanning the wavelength range and recording the absorbance. It is widely used in organic chemistry to investigate the extent of multiple bond or aromatic conjugation within molecules. The technique can be expanded to gases and solids, and also beyond absorption, to include measured reflected rather than transmitted light.

Light **absorption** can be described by two fundamental laws as

- **Lambert's Law -**The proportion of incident light absorbed by a transparent medium is independent of the intensity of the light (provided that there is no other physical or chemical change to the medium). Therefore, successive layers of equal thickness will transmit an equal proportion of the incident energy.

Lambert's law can be expressed by

$$I/I_o = T,$$

where I is the intensity of the transmitted light, Io is the intensity of the incident light, and T is the Transmittance.

- **Beer's Law-**The absorption of light is directly proportional to both the concentration of the absorbing medium and the thickness of the medium in the light path.

A combination of the two laws (known jointly as the Beer-Lambert Law) defines the relationship between absorbance (A) and transmittance (T).

$$A = \log Io/I = \log 100/T = \varepsilon\ c\ b$$

Where, A is absorbance (no unit of measurement), ε is molar absorptivity ($dm^3\ mol^{-1}\ cm^{-1}$), c is molar concentration ($mol\ dm^{-3}$), and b is path length (cm).

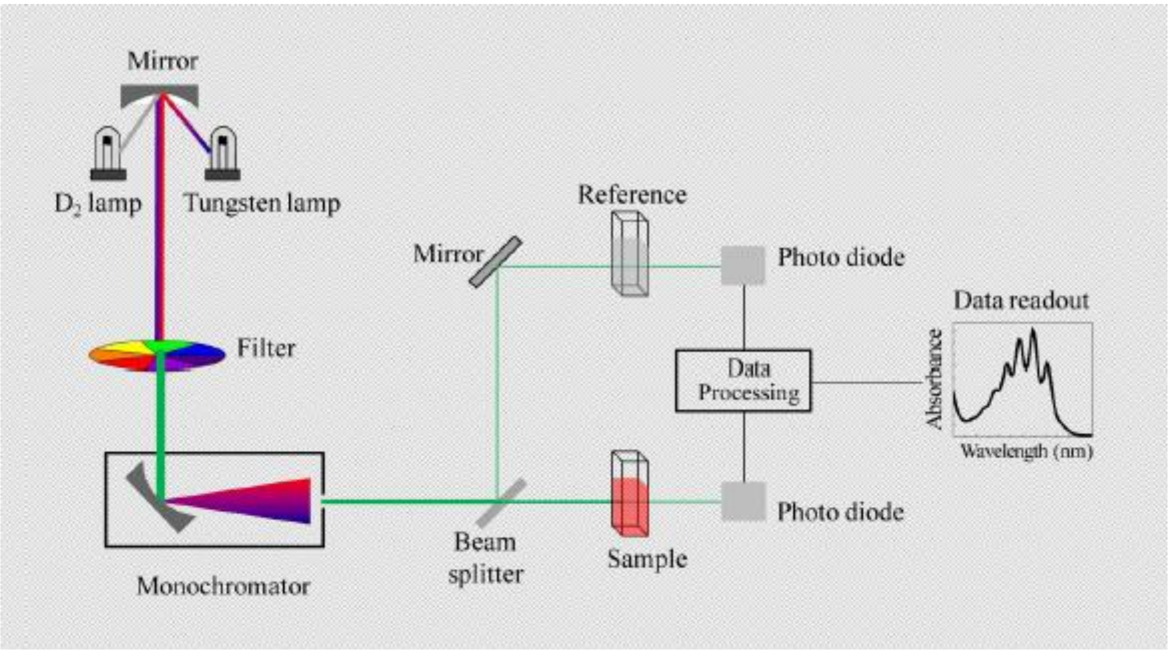

Figure 4. 11 Basic Principles of UV-VIS Spectroscopy

- **Light reflection and reflectance spectra**

Diffuse reflectance relies upon the focused projection of the spectrometer beam into the sample where it is reflected, scattered and transmitted through the sample material (shown on the right). The back reflected, diffusely scattered light (some of which is absorbed by the sample) is then collected by the accessory and directed to the detector optics. Only the part of the beam that is scattered within a sample and returned to the surface is considered to be diffuse reflection.

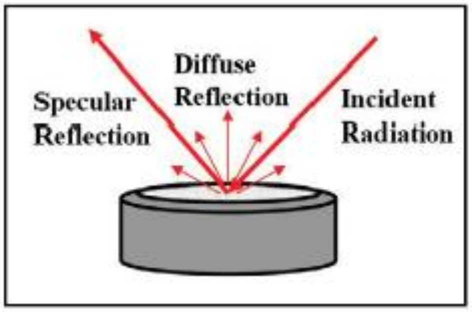

Figure 4. 12 Diffuse and Specular Reflectance

Other factors related to high spectral quality for diffuse reflectance sampling are particle size, refractive index, homogeneity,packing. Even with all these sample preparation practices, the raw diffuse reflectance spectra will appear different from its transmission equivalent (stronger than expected absorption from weak IR bands). A Kubelka-Munk conversion can be applied to a diffuse reflectance spectrum to compensate for these differences.

Kubelka-Munk Function

$$\mathbf{F(R)} = \frac{\mathbf{(1-R)^2}}{\mathbf{R}} = \frac{\mathbf{k}}{\mathbf{s}}$$

R is the absolute reflectance of the sampled layer, k is the molar absorption coefficient and s is the scattering coefficient.

The spectra shown above demonstrate this spectral conversion for ibuprofen collected by diffuse reflectance. The Kubelka-Munk converted spectrum for ibuprofen shows excellent comparison with the transmission spectrum and is easily identified using library search of a transmission spectral data base.

- **Components UV-Vis Spectrophotometer**

Spectrophotometer consists of the following components

- a source of radiation of appropriate wavelengths
- Monochromator and optical geometry,
- filter Sample compartment
- Detector, Photomultiplier, Measuring system, computer

The UV VIS spectra carried out by Shimadzu UV 3600 spectrophotometer.

Figure 4. 13 UV-VIS-NIS (SHIMADZU UV-3600) Spectrophotometer

4.5 Wettability Analysis:

4.5.1 Contact Angle Measurement and Drop Contour Analysis:

The optical analysis of drops that hang from a dosing needle or are placed on a solid surface facilitates the determination of different surface and interfacial parameters. The contact angle that a liquid drop establishes on a solid surface characterizes the solid's wetting behavior with said liquid.

Having measured the contact angles of multiple test liquids the surface energy of the solid can be determined and the latter can be used to calculate the work of adhesion for different liquids. In short: the measurement of contact angle helps in all situations where solids and liquids meet and advantage is to be gained by the control of wetting and adhesion properties.

- **Working Principle:**

- **Young's Equation**

An equilibrium of vectorial forces dictates the contact angle θ_c at the three phases contact line of a deposited drop. The surface energy of the solid γ_S acts along the solid surface. The solid-liquid interfacial energy γ_{SL} acts in the opposite direction and the surface tension γ_L of the liquid acts tangential to the drop surface. This can be described by a simple scalar equation:

$$\gamma_L \cos\theta_c = \gamma_S - \gamma_{SL}$$

The drop is viewed in profile during the contact angle measurement. The image processing software recognizes and records the drop contour, as well as the base line at the solid-liquid interface and fits a mathematical function to the drop shape.

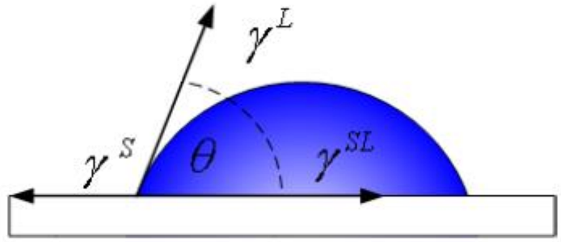

Figure4. 14 Young's Equation

- **Young-Laplace Evaluation:**

When no other factor is in play a drop of liquid tends to form a sphere, due to its surface tension. The typical drop shape materializes because the drop is elongated due to gravity. The Young-Laplace evaluation of pendant drops recognizes this fact: The characteristic shape of the drop profile yields the surface tension γ_L of a liquid. In the case where a pendant drop is surrounded by a second liquid, rather than air, the interfacial tension between the two liquids can be deduced from the drop shape. For optical analysis the outer liquid has to be transparent. Depending on the relative densities, the inner liquid can be dosed either as a pendant drop or upwards, via a bent needle.

To determine the surface energy of a solid one measures the contact angles of test liquids whose surface tensions including their dispersive and polar parts are known. These dispersive and polar parts are used to calculate the interfacial tension γ_{SL} between the solid and a liquid based on a suitable model.

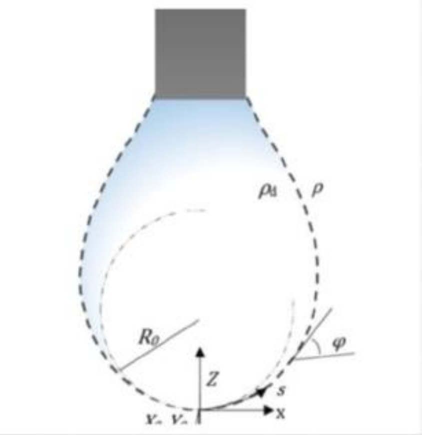

Figure 4. 15 Pendant Drop in Young-Laplace Equation

An applied model is the one of Owens, Wendt, Rabel and Kaelble (OWRK model) which considers the geometric mean of the dispersive and polar parts of the liquid's surface tension γ_L and of the solid's surface energy γ_S

$$\sigma_{SL}=\sigma_S+\sigma_L-2\sqrt{\sigma_S^d\sigma_L^d}-2\sqrt{\sigma_S^p\sigma_L^p}$$

Substituting this expression in the Young equation, the polar and the dispersive part of the solid's surface energy can be determined from the regression line in a suitable plot. The linear regression requires contact angle measurements with at least two different test liquids. However, as a regression line based on just two points contains no information on the accuracy of the result, contact angle measurements with at least three test liquids are recommended for the determination of the surface energy of solids.

- **OCA 15C (Instrument for Contact Angle Measurement):**

The OCA 15EC is the entry level measuring device for professional contact angle measurements and drop shape analysis.

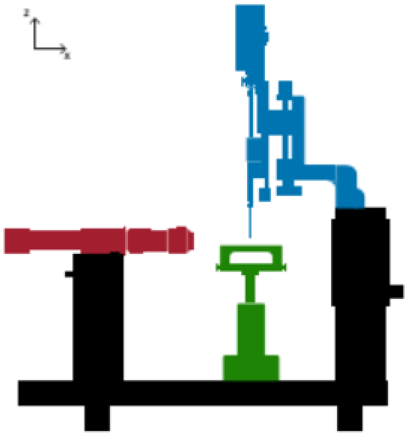

Figure 4. 16: Schematic Diagram for Contact Angle Measurement

- **Sample table:** The sample table of the OCA 15EC can slide freely in X- and Y-direction and is locked into position with its switchable magnetic base. In Z-direction the sample table is adjustable using precision mechanics with a hand wheel.

- **Lens and Camera:** The fast 6-fold zoom lens with manual focus and adjustable observation angle in combination with the USB camera ensures pin-sharp drop images and facilitates the effortless analysis with the SCA software.

- **Dosing System:** With a single direct dosing system SD-DM can be positioned and dosed with one or two electronic syringe modules ESr-N, respectively. Direct tubeless dosing of the syringe content and the ability to use cost-saving disposable syringes and needles allow for short preparation times and minimal cleaning efforts.

- **External light:** This comes with a feature of a LED lighting with manually and software-controlled intensity. Due to an automatic temperature drift compensation a stable and homogeneous illumination of the sample is guaranteed at all times.

Even though the OCA 15EC is a high precision measuring device designed for laboratory use, it is highly mobile and can effortlessly be taken apart with two star grip screws and be stored securely in a transport case.

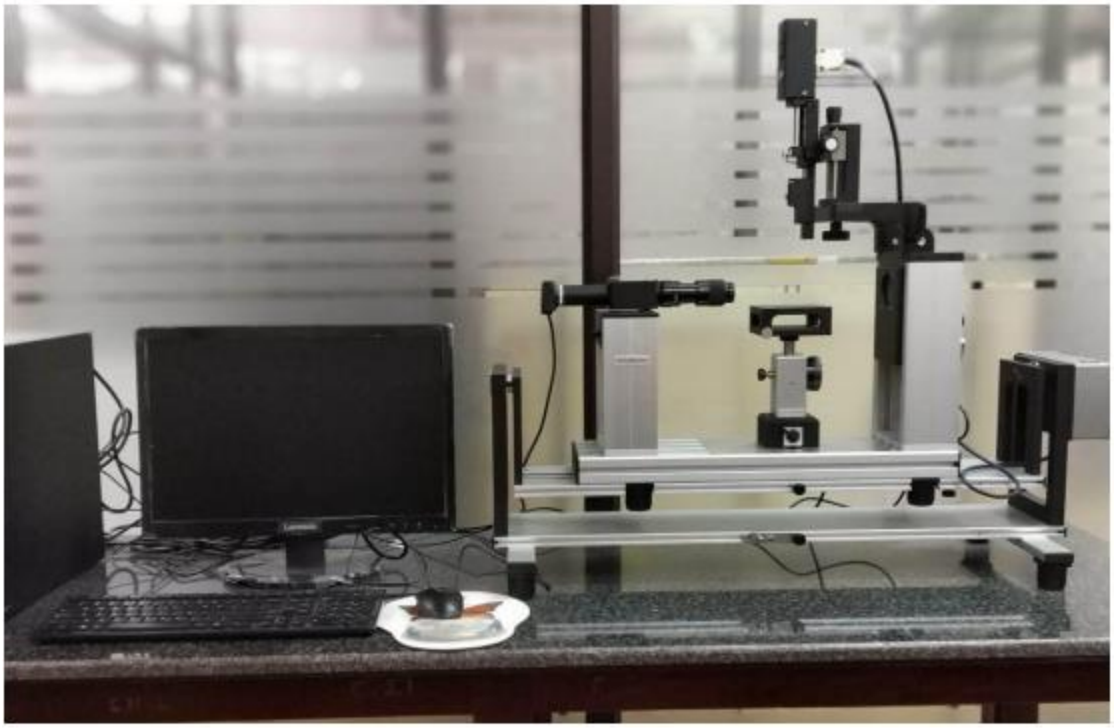

Figure 4. 17: Instrument for Contact Angle Measurement

- **Software: SCA**

The SCA software, designed for Microsoft Windows, is the modular program for all OCA instruments. The SCA software features recording and storing of movie sequences which allows for a controlled evaluation of even the fastest processes. The SCA software is divided into the following separately available modules:

- **SCA 20-contact angle -** It measures and presents the static contact angle on plane, convex and concave surfaces according to the sessile drop and the captive drop method. It also measures dynamic contact angles (advancing and receding angle, contact angle hysteresis) according to the needle-in-drop method and the tilting method.
- **SCA 21- surface energy** - It determines the surface energy of solids as well as of its

components (e.g. dispersive, polar and hydrogen bond parts, acid and base portions) according to nine different theories. It can calculate and represent of wetting envelopes and work of adhesion/contact angle diagrams.

- **SCA 22 - surface/interfacial tension -** It determines the surface and interfacial tension, as well as of their polar and dispersive parts, based on the Young-Laplace evaluation of pendant drops.

4.6 Field Emission Setup

Electrons may be emitted from a solid surface into a vacuum by many mechanisms, including thermionic emission, photoemission and field emission. In field emission, electrons tunnel though the surface potential energy barrier, which has been thinned and shaped by a strong electric field. A sharp emitter structure usually offers a strong electric field even when the applied voltage is low.

- **Working Principle:**

The field emission is an application example of the quantum-mechanical tunneling effect. The field emission allows generation of free electrons with a very low energy spread, the effect is used for field emission microscopy and scanning tunneling microscopy. The conduction electrons are almost freely movable in the interior of a metal. The emission of electrons into the outer space is prevented by a potential rise at the surface of the metal. This is how to characterize a free electron gas that is trapped in a potential well. At temperature T = 0 K, all states are occupied by two electrons (Pauli principle) up to the Fermi energy E_F within the model of potential box. The energy difference between the Fermi energy E_F and the vacuum level is referred to as the work function ϕ. At temperatures above absolute zero point, the free electrons occupy energy levels above the Fermi energy by thermal excitation. They can even be excited in the energy continuum above the vacuum level for strong heating, and thus can be emitted. This is referred to as thermionic emission. The potential step at the surface of a metal is transformed into a wedge-shaped potential barrier in case of a strong electric field. For high field strengths, the width Δx of potential barrier at the Fermi level is reduced such that some of the electrons can pass through due to quantum mechanical tunneling effect. The electrons are not raised over the potential step as in the case of the thermionic emission; but they tunnel through the potential barrier without changing their energy.

- **Instrumental description:** Field emission measurements were carried out by using a diode configuration consisting of a cathode where the sample is being kept and a stainless steel tip anode of conical shape with a 1 mm tip diameter mounted in a liquid nitrogen trapped rotary-diffusion vacuum chamber with appropriate chamber baking arrangement. The measurements were performed at a base pressure of ~ 10^{-7} mbar and the temperature was measured with the help of a PID control system. The tip to sample distance was continuously adjustable to a few hundred μm by spherometric arrangement with screw-pitch of 10 μm. The position of just touching the anode with the sample having high resistance was determined by an optical microscope and then various spacing was obtained by rotating the micrometer screw as its screw-pitch is known. Field emission current-voltage measurements were done with the help of an Agilent multimeter (model 3440-1A). The schematic of the field-emission apparatus has been shown in fig 4.18.

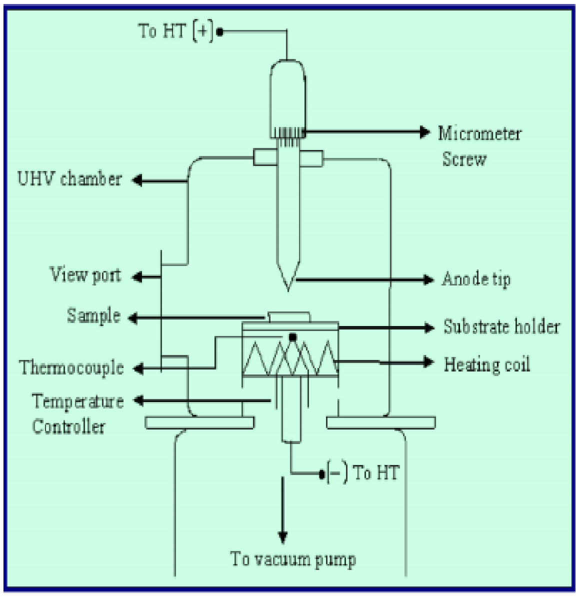

Figure 4. 18 Schematic Diagram of Field Emission Setup

Chapter 5

Synthesis, characterizations and field emission property of porous SiNWs

Abstract:

In this study, silicon nanowires are synthesized by metal assisted chemical etching (MaCE) at 60 ^{0}C temperature with different etching time. SiNW 40, SiNW 60, SiNW 80 are obtained at 40, 60, 80 min of etching time respectively. XRD, FESEM, TEM, UV-VIS, FTIR are studied to characterize all nanowires. The sharp needle like structure of nanowires influences them to be good field emitters. Field emission study is performed for all the samples experimentally and it is observed that as the etching time increases field current density enhances though after 60 min of etching, there is a degradation of field emission property like turn on, enhancement factor. It is primarily due to high aspect ratio for which tip agglomeration can cause of screening effect at low electric field. Thus 60 min of etching of silicon nanowire can be optimum one for field emission application. ANSYS simulation is performed which agrees the fact of enhancement of field current at high etching time by varying the diameter and length of the nanowires.

5.1 Introduction

Silicon is the most important semiconductor for development of modern microelectronic technology leading to one of the greatest industrial success stories of the 20th century.[1]Therefore, many research works are being carried out toward the development Si nanowires, nanoribbons and nanotubes, and utilization of such nanostructures in miniaturized electronic devices by enhancing photothermal effect,[2] excellent field emission,[1,6,7] and photovoltaic applications[3]. One-dimensional semiconductor nanowires are of a great interest for their physical properties due to its high aspect ratio, optical, electrical, electronic and mechanical property which can be tuned by simply varying the aspect ratio by changing the conditions during synthesis or by doping with suitable foreign material. [4]

Silicon nanowires have been synthesized by various methods which have been reported before like laser ablation, vapour-liquid-solid (VLS) process, chemical vapour deposition, oxide-assisted growth, plasma etching, physical evaporation or metal-assisted chemical etching. [5-9]. Out of these techniques metal-assisted chemical etching is most cost effective and easy process as the other methods require high temperature, high vacuum and ignitable silicon precursors which incurs a high cost of synthesis [5-9].So here we use the metal-assisted chemical etching technique for the synthesis of the silicon nanowires and the parameters during synthesis are varied to obtain changes in the morphological structure.

Field-emission (FE) is one of the main features of nanomaterials and nanostructures and it has a great commercial interest in displays and other electronic devices. In comparison with conventional bulky technologies, nanostructures have the advantage of faster device turn-on time, compactness and sustainability [10]. Recently a lot of research work has been carried out for one dimensional nanostructures as these are the potential candidates of field emission which can be used as practical field emitters and are also cost efficient. Silicon nanowires as field emitters were already reported but the synthesis procedure was costly.

Generally silicon nanowires considered to be long cylinder without any pores. Actually having pores may be come advantageous to several applications due to its increment of surface area and quantum confinement effect from the shrinkage in Si residual skeletons. Here, MaCE is the most cost effective and full proved mechanism to discuss. Porosification of silicon nanowires has enhanced its acceptance in the field of batteries, energy storage, drug delivery, photocatalysis, gas sensors etc.

In this study, porous silicon nanowires (SiNW) are synthesized through MaCE (Metal assisted Chemical Etching) varying the etching time under a constant temperature. Different characterizations are performed to confirm its formation and properties. After that, The field emission characteristics of these nanowires are characterized in an ultra-high vacuum chamber with a cathode-anode probe arrangement and turn-on fields and enhancement factors of the samples are found using Fowler Nordheim equations.

5.2 Experimental

5.2.1 Synthesis

Silicon nanowires are prepared by the method of Metal-Assisted Chemical Etching (MaCE) in a two-step etching approach.[11] Commercially available (boron doped) p-type silicon wafers of (100) orientation are cut into suitable sizes and cleaned in acetone followed by ethanol for 10 minutes each in an ultrasonic bath. Organic residues are removed from the surface of wafers with a freshly prepared Piranha-solution, a mixture of 3:1 H_2SO_4 (97%) an H_2O_2 (35%) for 30 min followed by proper rinsing by DI water. The generated thin oxide layer are then dissolved in HF (5%) solution.

Now, in the first step of MaCE process, the treated wafers were transferred for Ag nanoparticles (AgNPs) deposition into a solution containing 4.8 M HF and 0.014 M $AgNO_3$ for 1 min at room temperature. In the second step, the Ag-coated samples are etched by 4.8 M HF and 1.0 M H_2O_2 in oven at **60° C** temperature for three time periods **40, 60 and 80 minutes** respectively. After etching the Ag particles are removed by HNO_3 solution and the sample is rinsed with deionized water. During rinsing oxide layer is generated by HNO_3 which is removed by dipping the substrate in HF (5%) solution for 5 minutes again. The wafer is washed in deionized water for several times and then dried in vacuum oven at 60°C temperatures for 3-4 hours.

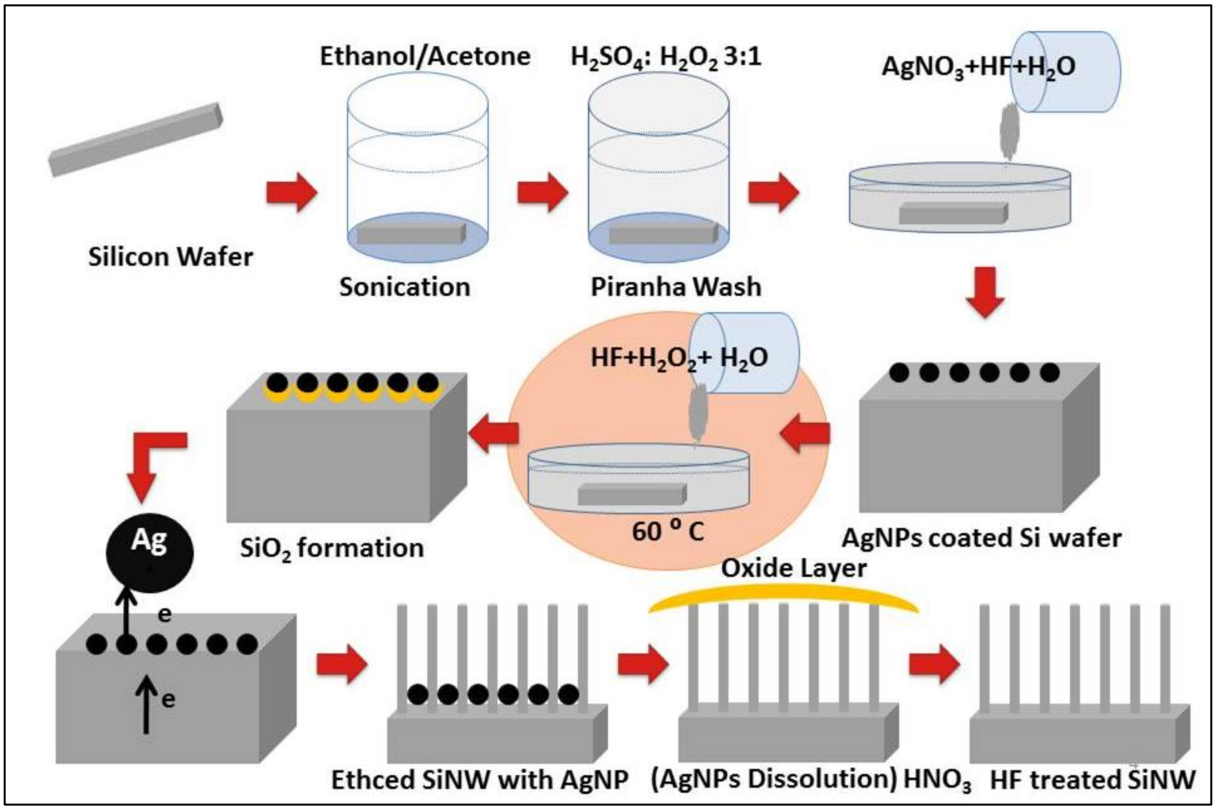

Figure 5. 1: Schematic diagram of the synthesis process of Silicon Nanowires

At first, oxidation of silicon takes place

$$Si + 2\ H_2O + 4h^+ \rightarrow SiO_2 + 4H^+ \quad \text{……….. (1)}$$

$$Si + 2\ H_2O \rightarrow SiO_2 + 4H^+ + 4e^- \quad \text{……….. (2)}$$

At second, etching of silicon dioxide produces

$$SiO_2 + 6HF \rightarrow H_2SiF_6 + 2\ H_2O \quad \text{……….. (3)}$$

Etching of SiO_2 occurs with a higher rate than etching of pure Si in HF. Therefore, it is the dominating etching process. Additionally, the Si oxidation is promoted by Ag and so a higher etching rate of Si mediated through the catalytic activity of the noble metal is achieved.

Through the charge transfer on the interface of Ag and Si, the silver nanoparticles are sinking deeper and the silicon nanowires arise as the remaining of unetched silicon. The driving force is the oxidizing power of the oxidizing agent H_2O_2. The driving force is given by H_2O_2 oxidizes the Ag particles, which in turn reduced at the silicon interface by an electron transfer from the silicon and thereby oxidize the silicon. This can be described as charge transfer process in which the silver injects holes into the silicon, eq. (2). Thus the porous SiNW 40 (40 min of etching), SiNW 60 (60 min of etching), SiNW 80 (80 min of etching) are synthesized. H_2O_2 plays an important role in increasing porosification and an optimum temperature is also a worthy factor.

• Preparation of Piranha solution

Piranha solution is a typical mixture is 3 parts of concentrated sulfuric acid and 1 part of 30% hydrogen peroxide solution. It is used to clean organic residues off substrates. Because the mixture is a strong oxidizing agent, it will remove most organic matter, and it will also hydroxylate most surfaces (add OH groups), making them highly hydrophilic (water-compatible). Piranha solution should always be prepared by adding hydrogen peroxide (3ml) to sulfuric acid (9ml) slowly, never in reverse. Mixing the solution is extremely exothermic. If the solution is made rapidly, it will instantly boil, releasing large amounts of corrosive fumes and increasing temperature of the mixture highly.

• Hydrofluoric acid safety

Some of the procedures presented here use hydrofluoric acid (HF) but it is an extremely corrosive acid. Exposure to HF and its fumes can be fatal even if the amount is very small. It must be handled only by trained one and must be used very cautiously. Only plastic materials are used during using of HF as it is highly reactive to metal.

Some basic concepts about solutions

→ Molarity is the number of moles of solute present in 1 litre of solution.

→ Mass percentage of a component in the solution is 100 times the mass of the component in the solution divided by total mass of the solution.

→ Number of moles= mass in grams/Molar mass.

→ Normality equation : $V_1S_1=V_2S_2$

→ Molarity equation : $M_1V_1=M_2V_2$

→ Molarity formula M=((% x density)/molecular weight)x1000

To prepare 4.8M HF (Hydrofluoric acid) solution

Density of 40% HF acid (d) = 1.13 gm/ml

Molecular weight of HF = 20.01 gm/mol

Molarity of 40% HF acid = (40% x 1130)/20.01= 452/20.01=22.6M

Now using $M_1V_1= M_2V_2$

$22.6\times V_1 = 4.8\times10$

$V_1 =2.125$ ml

So, add 2.125 ml HF to 2.5 ml DI and make final volume 10 ml.

To prepare 0.014M $AgNO_3$ (Silver nitrate) solution

Density of $AgNO_3$ (d)= 4.35 gm/cm^3

Molecular weight of $AgNO_3$ = 169.87 gm/mol

So, 1000ml of solution contains 169.87 gm/mol of $AgNO_3$

This implies, 10ml solution contains 1.6987 gm/mol of $AgNO_3$

So to prepare 10ml of 0.014M of $AgNO_3$ solution, (1.6987x 0.014) = 0.0234gm of $AgNO_3$ is added to 10ml of DI.

- **To prepare 1M H_2O_2 (Hydrogen Peroxide) solution**

Density of 30% H_2O_2 (d) =1.11 gm/ml

Molecular weight of H_2O_2= 34.01 gm/mol

Molarity of 30% H_2O_2 = (30% x 1110)/34.01= 333/34.01= 9.8M

Now using $M_1V_1=M_2V_2$

$9.8 \times V_1 = 1.0 \times 10$

$V_1 = 1.020$ ml

So, add 1.020 ml of 30% H_2O_2 to DI and make final volume 10 ml.

5.2.2 Characterizations

The as-prepared samples are characterized by a X-ray diffraction (XRD, BRUKER D8 Advance) analysis using a Cu-Kα radiation (0.154056 nm) over a scanning angle (2θ) ranges from 20° to 80°. Morphological study of the as prepared samples is carried out by Field emission scanning electron microscope (FESEM, Hitachi, S-4800) and transmission electron microscope (JEOL-JEM 2100, operated at 200 kV). The chemical structure of the nanowires is analyzed by using the Fourier transform infrared (FTIR) spectrometer (Shimadzu). Detail optical study is done with the help of a UV-Vis spectrophotometer (Shimadzu UV-3600).Field emission studies are measured in high vacuum field emission set up. The field emission measurement setup was in a high vacuum (2×10^{-6} mbar) chamber.

5.3 Results and Discussion

5.3.1 Morphological analysis

5.3.1.1 FESEM analysis

In fig 5.2, the FESEM images of SiNWs synthesized at different etching times are shown as top view. Fig 5.2(a), (b) represent silicon nanowires at 40 minutes of etching time at different scales (SiNW 40); (c), (d) denotes 60 minutes of etched silicon nanowires (SiNW 60) and (f), (g) are image of 80 minutes etched silicon nanowires (SiNW 80). It can be clearly seen that porous SiNWs are developed uniformly over the entire field of view, thus the yield is very high. The nanowires are vertical as (100) oriented silicon wafer is used for the experiment. The diameter obtained from the images of SiNWs varies from 40 nm to 200 nm with variation of etching time approximately. SiNWs becomes ultrathin with increase of etching and heating time. The diameter of the nanowires of 40 min etching time ranges from 150-200nm, nanowires of 60 min etching time is 100-150 nm and nanowires of 80 min etching time is 40-100 nm obtained from fig 5.2 (a), fig (c) and fig (f) respectively. The length of SiNWs as observed from fig 5.2 are 20, 25, 30 μm respectively. So it can be summarized from FESEM analysis that as etching time increases the length of the nanowires increases and it becomes ultrathin. [12]

It is seen in fig 5.2 (f) and (g) that the tips of the nanowires get agglomerated for SiNW 80 due to excessive increment of its length. The possible reason behind this conglomeration has been discussed by Zhang et al. [13] and it describes about strong forces among the tip of the long nanowire which is due to dangling bonds and electrostatic charges resulting in mutual interaction between them. Again, Bai et al. [14] emphasizes on van der wall force for this bundling of the nanowires at high etching time as seen in for 80 minutes. As density of nanowires increases the wires become closer to one another resulting in the increased effect of van der walls force therefore joining of the tips of the wires. It can play an important role in many applications.

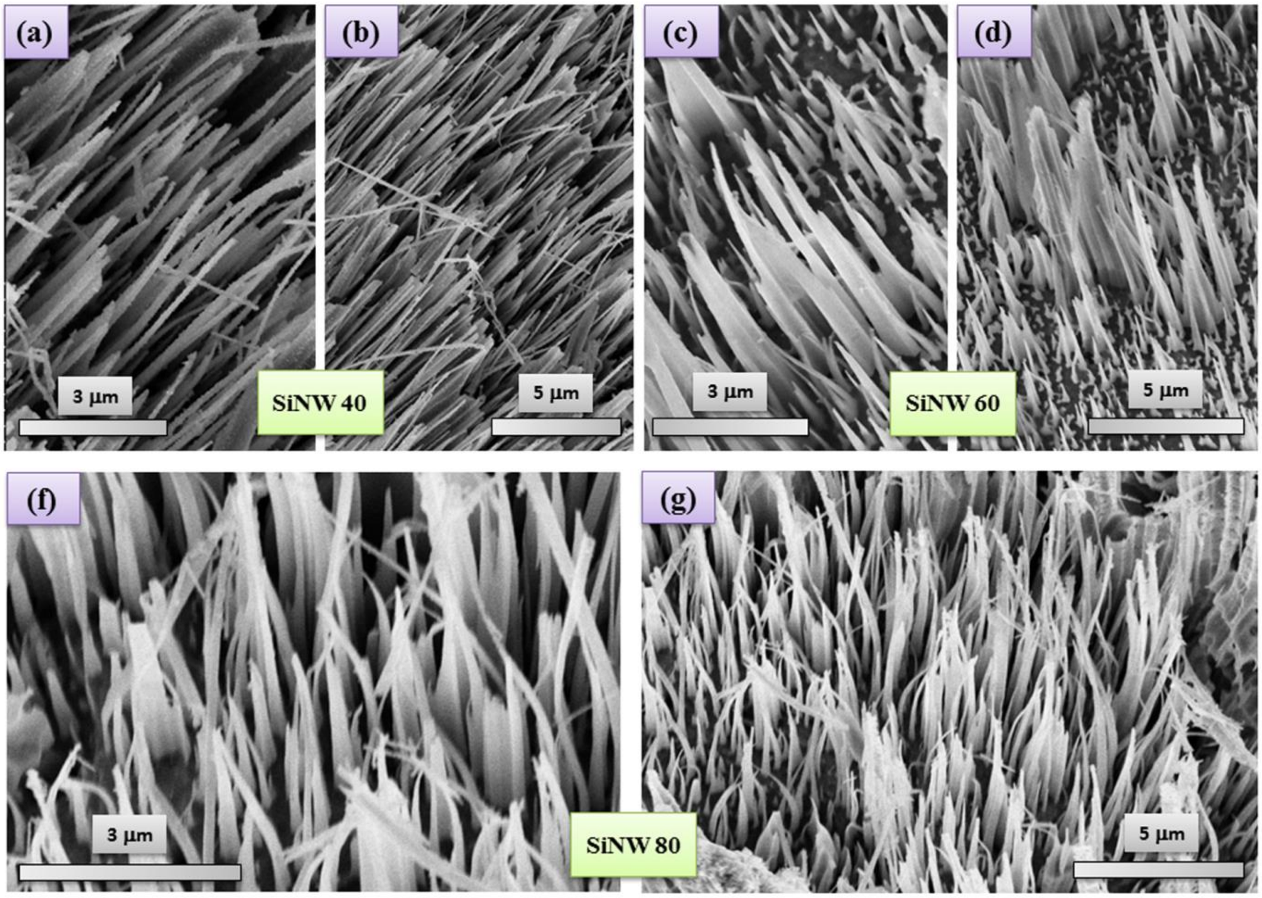

Figure 5. 2: Top view of MaCE synthesized (a), (b) SiNW 40 (c), (d) SiNW 60, (f), (g) SiNW 80

5.3.1.2 HRTEM analysis

Detailed analysis of the microstructure is represented by the HRTEM image of SiNWs synthesizes at 80 min etching time in fig 5.3. The sample grid is prepared by scraping the SiNWs from the silicon substrate and sonicating it in a small amount of ethanol and then it is dropcasted on the grid. Though the TEM image displays the size of the nanowires can be clearly seen to be around 100nm. From the fig 5.3(c) and (d) it is evident that the SiNWs formed are porous in nature. Balasundaram et al. [15] previously reported that with increase of etching time and heating, the porosity increases. The formation of the pores result in the decrease in mechanical strength of silicon nanowire as suggested by liu et al. [16] which may also be a reason for the agglomeration of the wires. The concentration of oxidizing agent i.e. H_2O_2 may also play an important role in increment of porosity.

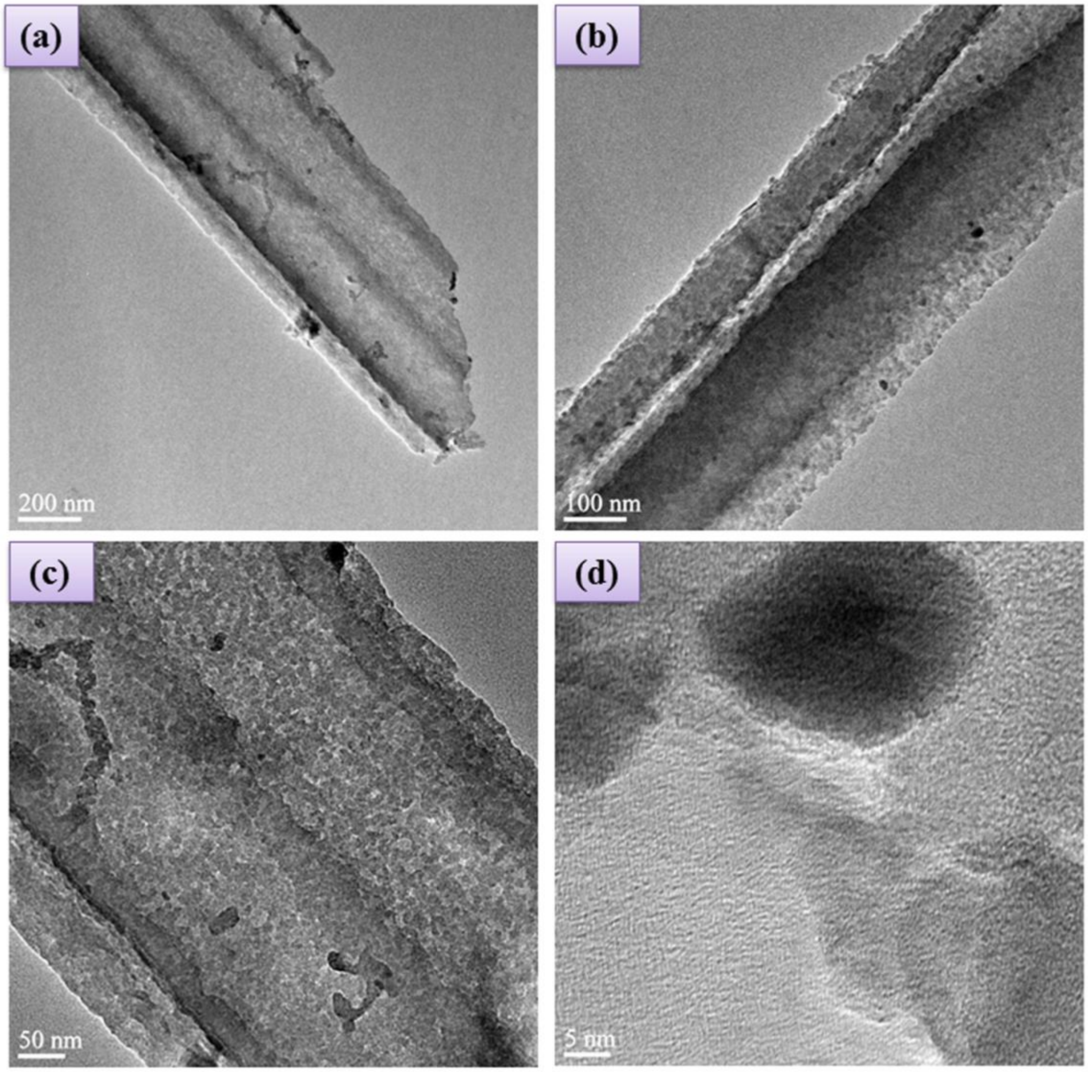

Figure 5. 3: (a), (b)TEM image of SiNW 80 at different scales with (c) porosity and (d) lattice image

5.3.2 XRD analysis

Changes in crystallinity during synthesis of the nanowires are analyzed using x-ray diffraction (XRD). XRD results show the most intense sharp peak at every sample around 69° (2θ) which correspond to (400) plane as observed in fig 5.4. This means both the Si wafer and produced SiNWs retained the crystalline property of silicon as we know that amorphous materials do not produce sharp peaks. Hence, the peaks in the XRD pattern indicate good crystallinity of the prepared samples. This means property of silicon is intact and no contamination or transformation occurred although several chemicals are used during synthesis.

The interplanar spacing (d_{hkl}) was obtained for each sample using Bragg's law of diffraction $d_{hkl} = \frac{\lambda}{2\sin\theta}$. The d_{hkl} for Si wafer is 1.355 Å. The d_{hkl} of 40 min, 60 min and 80 min obtained for the respective θ values from the XRD plots are 1.357 Å, 1.360Å and 1.359Å.

The position of second less intense peaks are 32.93° ,61.64° for sample with etching time 40 minutes, 32.87° , 61.62° for etching time 60 minutes and 33.25°, 61.88° for pure Si respectively as seen fig 5.4. Less intense peak for sample etched for 80 minutes almost disappeared. So intensity peak at $2\theta \approx 33°$ of Si wafer is becoming broader in the etched SiNWs. Now if we compare the broadening of the peak among the etched samples with different etching time, we see that with the increase of etching time, the peak becomes more broader and for SiNW 80, this peak is about to disappear.

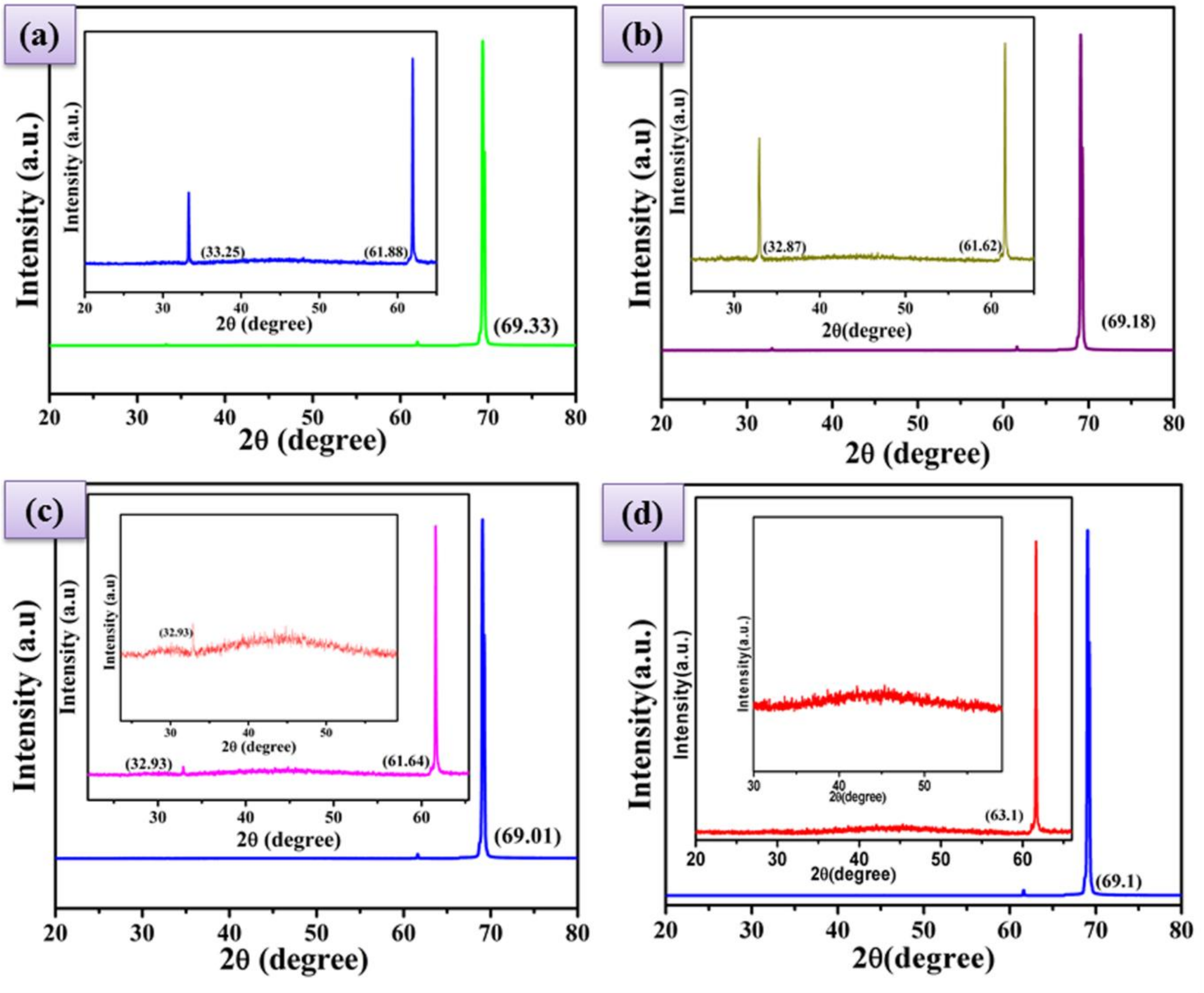

Figure 5. 4: XRD analysis of (a) Pure p-type Si wafer; (b) SiNWs etched and heated for 40mins; (c) SiNWs etched and heated for 60 mins; (d) SiNWs

As the peak become broader, the full width at half of maximum intensity increases. According to Scherrer formula, $\tau = \frac{k\lambda}{\beta\cos\theta}$ where τ is thickness and β is full width at half maximum for a given wavelength. So from Scherrer formula decreasing of β implies the formation of nanowires. [17]

5.3.3 FTIR analysis

In fig 5.5, the absorption spectra of the samples are presented. It shows the well-known transversal optical (TO) resonance, the Si–O–Si bond rocking vibrational mode (468cm^{-1}), the O–Si–O bond bending mode (808 cm^{-1}) and Si–O asymmetric stretching mode (1082cm^{-1}) [18]. Furthermore, the strongest absorption peak is found at the higher-frequency side around 1082 cm^{-1}.The absorption bands of silicon lattice are also observed, such as 611 cm^{-1}, 738 cm^{-1}, and891 cm^{-1}, which are almost same for all the samples. [19]

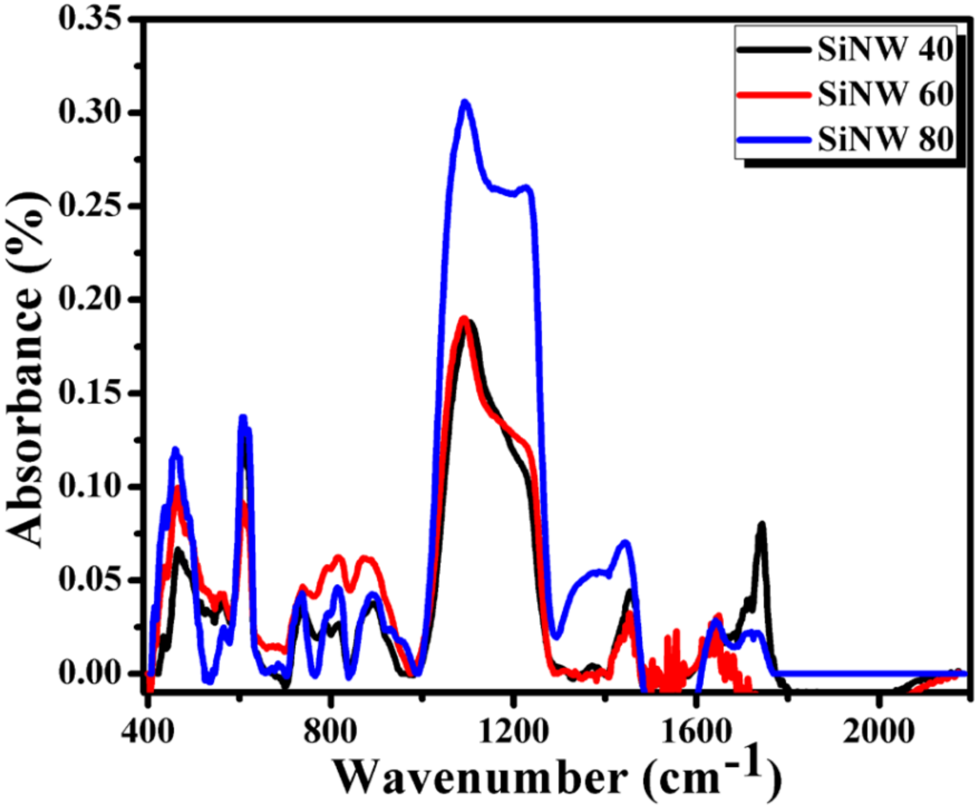

Figure 5.5: FTIR spectra of SiNW 40, SiNW 60, SiNW 80

The intensity and the shape of the main Si-O vibrational band at 1082 cm^{-1} increases with decreasing of the diameter of nanowires. These peaks appear when disorder of the structure is introduced. This can be explained from the analysis of oxide layer on SiNWs grown under different conditions. [20] The intensity of the absorption band of amorphous SiO_2 at the high frequency side of the main stretching mode can be enhanced in samples with a large degree of structure disorder [21].As the peak intensity at 1082 cm^{-1} difference between the sample of 40 min and 60 min etching time is not very high but it increases significantly for 80min so we can say that the structural disorder begins after 60 min of the etching time.

5.3.4 UV-VIS-NIR Spectroscopy

Diffuse reflectance spectra of the pure and SiNW samples etched for different times are shown in fig 5.6(a).The marked differences between the reflectance spectra between pure and etched samples can be seen from the fig 5.6(a) .In all 4 cases, reflectance shows an overall decrease with the decrease in wavelength and the reflectance falls sharply in wavelength range of 1000-1200 nm range. Moreover reflectance is around 11% in case of Si wafer and it varies from 40- 60% in SiNWs etched for different times which means that reflectance increases due to the formation of SiNWs. Here we measure diffuse reflectance which increases with increase in surface area. The rough surface obtained from long nanowire is responsible for such a visible increment of diffuse reflectance spectra. It also confirms about the large surface area formed from the wire formation. It is seen that the reflectance doesn’t change much with the varying etching times. So increasing reflectance confirms the formation of nanowires.

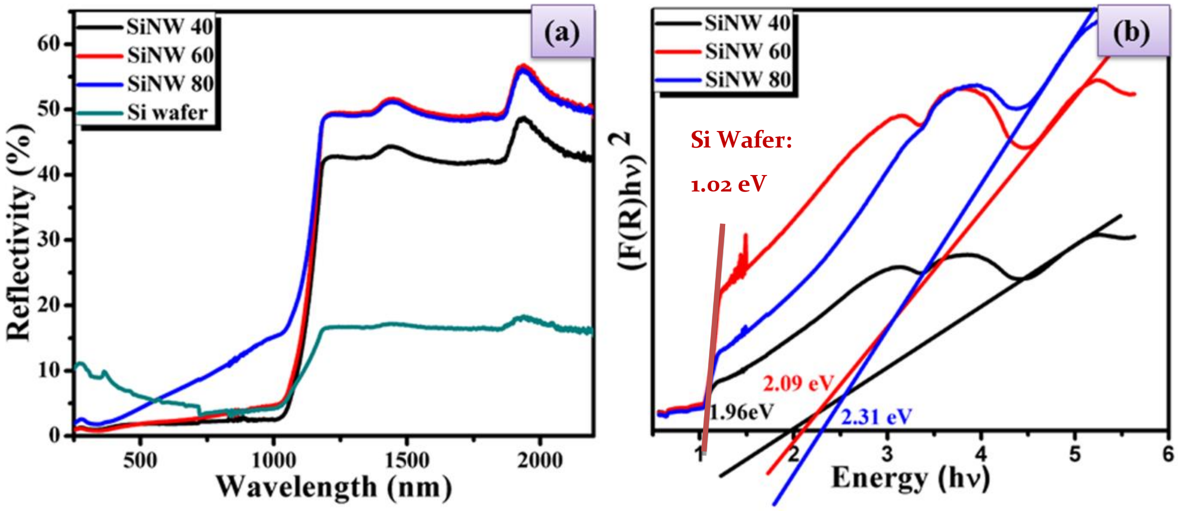

Figure5. 6:(a) Reflectance Spectra (b)Band gap for P- Type Si Wafer , SiNW 40, SiNW 60, SiNW 80

Table I: Bandgap of SiNW

Sample	Si Wafer (100)	SiNW 40	SiNW 60	SiNW 80
Bandgap (eV)	1.02	1.96	2.09	2.31

Band gap calculation: Bandgap calculation is done for SiNW 40, SiNW 60, SiNW 80 respectively from Kubelka-Munk formula. [22] The K–M method is based on the following equation.

$$F(R) = \frac{(1 - R)^2}{2R}$$

Where, R is the absolute reflectance of the sampled and F(R) is the so-called Kubelka–Munk function. After that, $(F(R)*h\upsilon)^{0.5}$ as silicon has indirect band gap is calculated and $(F(R)*h\upsilon)^{0.5}$ vs hυ is plotted. The linear portion of this graph is extrapolated to get band gap for the three cases. Band gap increases as the etching time increases as we can notice the band gaps are 1.96eV, 2.09eV, 2.31eV for SiNW 40, SiNW 60, SiNW 80 respectively in fig 5.6 (b). The band gap energy increases as diameter size of the semiconductor nanomaterials decreases and it is also higher than bulk silicon having a band gap of 1.13± 0.057 eV as silicon has indirect bandgap. [23]

5.3.5 Field Emission

Cold cathode emission characteristics were performed in our laboratory designed high vacuum system at pressure of ~ 10^{-6} mbar. In this experiment, a SiNW sample is glued to a stainless steel base acted as cathode and a conical shaped stainless steel tip (1.0 mm tip diameter) works as anode. The corresponding current (I) vs electric field (E) curves are obtained for pristine SiNW samples. The cold cathode emission current voltage characteristics are analyzed by the classical Fowler Nordheim (F-N) equation [24]:

$$J = A\frac{\beta^2 E^2}{\phi}\exp\left(-\frac{B\,\phi^{3/2}}{\beta E}\right)$$

where $A = 1.54 \times 10^{-6}$ A eV V^{-2} and $B = 6.83 \times 10^{9}$ eV$^{3/2}$ V m^{-2},J is the current density, E is the applied field, φ is the work function of the emitting materials and β is the enhancement factor relating to the following equation:

$$\beta = -\frac{B_{FN}\phi^{\frac{3}{2}}}{s}$$

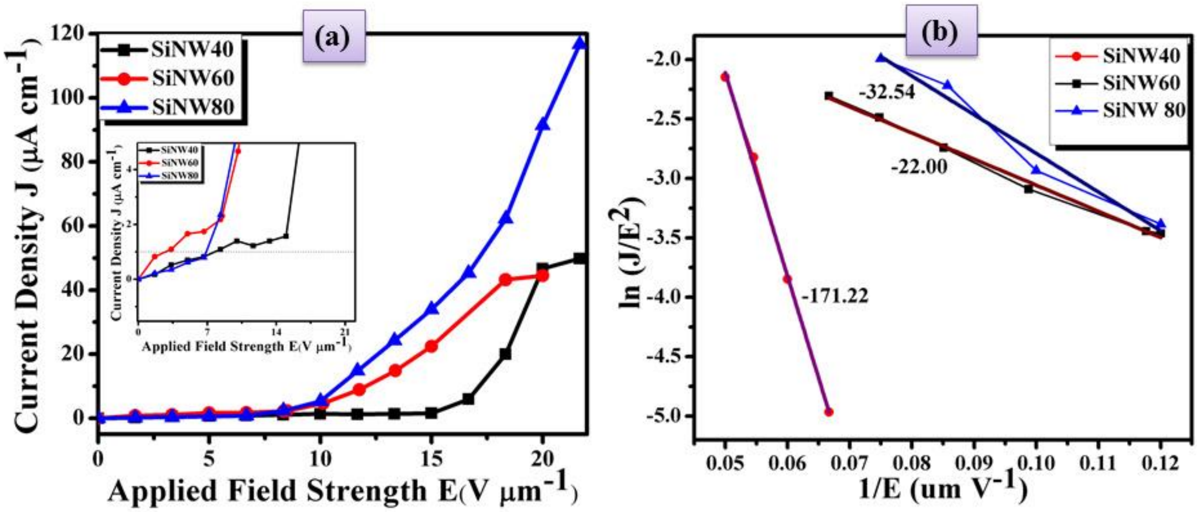

Figure5. 7: (a) Current density (J) versus applied field (E) plot, (b) F-N plot of SiNWs at 120 μm inter-electrode distances

The experimental J-E curve and corresponding F-N plot are shown in fig 5.7. The experimental turn on fields of the synthesized SiNW 40, SiNW 60 and SiNW 80 for 120 μm inter-electrode distances are 8.39 V/μm, 6.89 V/μm and 1.75 V/μm (defined as the field required obtaining current density of 1 μA/cm^2) (fig 5.7(a)). The enhancement factors of SiNWs have been calculated from the slope obtained in FN plot by taking the work function 4.64 eV [25]. The enhancement factors and the turn on fields have been given in the following table.

Table II: Field Emission properties of SiNW

Samples	Turn-on Field at 1μA/cm^2 (V/μm)	Enhancement factor (β)	Emission Current Densities at 15 V/μm (μA/cm2)
SiNW 40	7.8	399	1.56
SiNW 60	2.5	3103	22.6
SiNW 80	6.84	2098	34.6

Electron field emission behaviors are significantly dependent on the various parameters such as nanostructure morphology, nanostructure-anode distance, work function and screening factor etc. [26] The turn on field decreases as the etching time increases for SiNW40 and SiNW60. It is due to the fact that length of the nanowire and density of nanowire increases or as the tips becomes sharper [27]. The enhancement factor also increase as a result giving better emission characteristics.

It is to be noted that the enhancement factor does not vary linearly with aspect ratio (i.e. synthesis time) because in case of SiNW80 the turn on voltage decreases as observed in fig 5.7(b). [28] This may be due to various reasons like screening effect or local nanostructure i.e. the agglomeration of the tips of the nanowires. The screening also reduces the local electric field at the apex of SiNWs, thus offering less field enhancement factor. Again, in case of maximum emission current density drawn it increases linearly from SiNW40 to SiNW80. So the optimum synthesis time of nanowires is 60 min.

The local electric field profile of the silicon nanowires are further computationally investigated a finite displacement method as implemented in ANSYS Maxwell simulation package for theoretical understanding of the cold cathode emission at the nanoscale level of silicon nanowires. Simulated electric field distributions are carried out for silicon nanowires as cathode and stainless steel electrode as anode. Simulated parameters are chosen carefully to replicate the actual dimension of experimental configuration to keep up the direct correlation of the experimental counterpart taking only a few nanowires into consideration. A rainbow colour coordinate (red is maximum and blue is minimum) is used to plot the magnitude of the electric field of 2D plane in fig 5.8. Here the field increase constantly from SiNW40 to SiNW80 as obtained in 2.6kV voltage difference which relates with the experimental results.

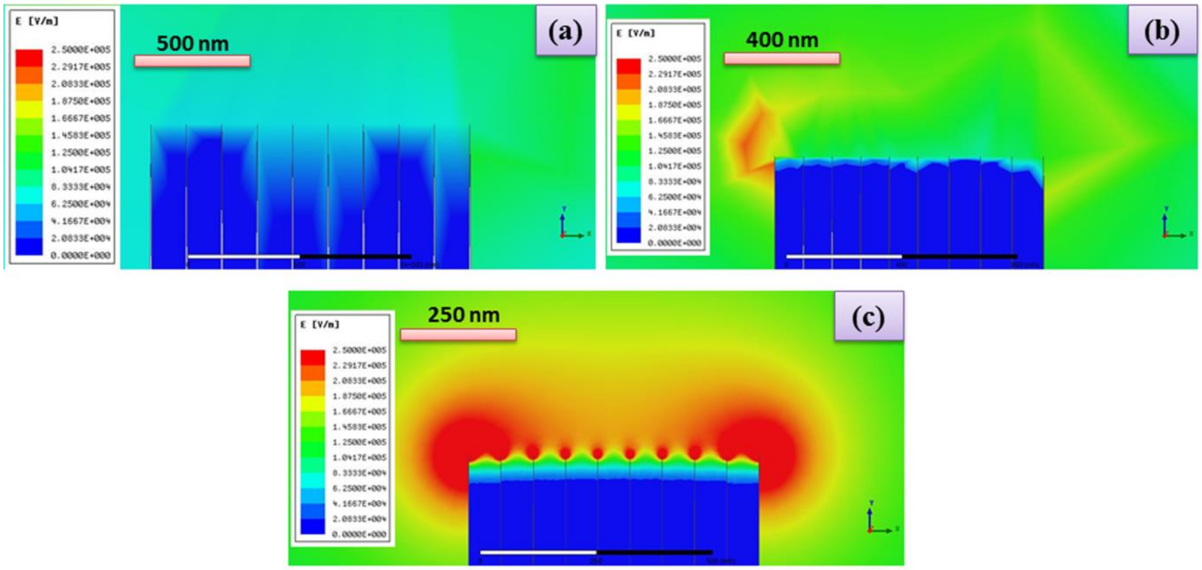

Figure 5. 8: Two dimensional representations of the enhancing field of (a) SiNW 40, (b) SiNW 60 and (c) SiNW 80 in ansys

From the FESEM image length of nanowires at different etching time can be obtained whereas from top view, diameter of the nanowire can be derived. These experimental results give the information how the diameter and length of the nanowires varies with etching time. Thus, these trends with different etching time are applied to ANSYS to get the trend of the field enhancement with etching time. It completely agrees with the experimental results. As etching time increases, enhancement of field emission is observed in simulation. In experiment also same trends are seen but there is a screening effect due to tip agglomeration at high etching time (80 min), therefore high turn on voltage is seen at low electric field though enhancement of current density is observed at high electric field. If there were no such agglomeration but only impressive aspect ratio was observed, it might completely agree with simulated results.

5.4 Conclusions:

In this study, SiNWs of different lengths are successfully synthesized using the metal assisted chemical etching technique at 60 °C temperature with different etching time. Important characterizations confirm about its successful formation. Due to its sharp structural properties, these nanowires are applied as good field emitters. Among all etching times, 60 minutes of etching of SiNW can be addressed as optimum due its low turn on field and high enhancement factor. SiNW80 is also a good field emitter but there is a drawback of tip agglomeration of nanowires for which screening effect is observed. Thus, turn on at low electric field increases and enhancement factor decreases though a high current is observed at high electric field. To support these results, simulation is done in ANSYS which also agrees that as the etching time increases, field current density increases. As the work function for all the nanowires are same, here structure i.e. diameter, length of nanowires become the key factors for field emission application. Again from the TEM, porosity of nanowires are observed. As etching time increases, porosity of nanowires increases, thus the surface roughness enhances with high surface areas. Thus, number of emitting site increases. It can also be an important factor for such a good field emission property.

References:

[1] Xiaosheng Fang, Yoshio Bando, Ujjal K. Gautam, Changhui Ye and Dmitri Golberg." Inorganic semiconductor nanostructures and their field-emission applications" J. Mater. Chem., 2008, 18, 509–522

[2] N.Wang, B.D.Yao, Y.F.Chan and X. Y. Zhang," Enhanced Photothermal Effect in Si Nanowires " Nano Lett., 2003, 3, 475.

[3] Kui-Qing Peng , Shuit-Tong Lee "Silicon Nanowires for Photovoltaic Solar Energy Conversion" Adv. Mater. 2011, 23, 198–215

[4] Mehedhi Hasan , Md Fazlul Huq and Zahid Hasan Mahmood "A review on electronic and optical properties of silicon nanowire and its different growth techniques" . SpringerPlus 2013, 2:151

[5] R. S. Wagner and W. C. Ellis "Vapor-Liquid-Solid Mechanism Of Single Crystal Growth" Applied Physics Letters, Volume 4, Number 5(1964): 89-90

[6] D. McClain, L. F. Dong, R. Solanki, and J. Jiao, “Synthesis of single crystalline silicon nanowires and investigation of their electron field emission”, J. Vac. Sci. Technol. B 24, (2006).20-24

[7] Xiaosheng Fang, Yoshio Bando, Changhui Ye, Guozhen Shen, Ujjal K. Gautam, Chengchun Tang and Dmitri Golberg "Si nanowire semisphere-like ensembles as field emitters" Chem. Commun.(2007) 4093–4095

[8] J. C. She, S. Z. Deng, N. S. Xu, R. H. Yao, and J. Chen "Fabrication of vertically aligned Si nanowires and their application in a gated field emission device" Applied Physics Letters 88,(2006) 013112

[9] Z. Huang, X. Zhang, M. Reiche, L. Liu, W. Lee, T. Shimizu, S. Senz, U. Gösele, Extended arrays of vertically aligned sub-10 nm diameter [100] Si nanowires by metal-assisted chemical etching, Nano Lett. 8 (9) (2008) 3046–3051.

[10] Xiaosheng Fang, Yoshio Bando, Ujjal K. Gautam, Changhui Ye and Dmitri Golberg "Inorganic semiconductor nanostructures and their field-emission applications" J. Mater. Chem., 2008,18, 509-522

[11] Xiangman Meng, Ailin Zhou, Bo Wang, Yu Chen, Yun-Hui Tang, Hui Yan "Stable Superwetting Surface Prepared with Tilted Silicon Nanowires" Nano-Micro Lett. (2016)

[12] Sanjay K Srivastava, Dinesh Kumar, S W Schmitt, K N Sood,S H Christiansen and P K Singh "Large area fabrication of vertical silicon nanowire arrays by silver-assisted single-step chemical etching and their formation kinetics" Nanotechnology 25(17):175601 (2014)

[13] M. Zhang, K. Peng, X. Fan, J. Jie, R. Zhang, S. Lee and N. Wong," Preparation of Large-Area Uniform Silicon Nanowires Arrays through Metal-Assisted Chemical Etching" Journals of Physical Chemistry C 112 (2008) 4444 – 4450.

[14] F. Bai, M. Li, D. Song, H. Yu, B. Jiang and Y. Li," One-step synthesis of lightly doped porous silicon nanowires in HF/$AgNO_3$/H_2O_2 solution at room temperature" Journals of Solid State Chemistry 196 (2012) 596 – 600.

[15] Karthik Balasundaram, Jyothi S Sadhu, Jae Cheol Shin, Bruno Azeredo, Debashis Chanda, Mohammad Malik, Keng Hsu, John A Rogers, Placid Ferreira, Sanjiv Sinha and Xiuling Li “Porosity control in metal-assisted chemical etching of degenerately doped silicon nanowires" Nanotechnology 23 (2012) 305304

[16] Junjun Liu and Zhifeng Huang " Reducing the porosity and reflection loss of silicon nanowires by a sticky tape" Nanotechnology 26 (2015) 185601

[17] T Ungár "Microstructural parameters from X-ray diffraction peak broadening" Scripta Materialia Volume 51, Issue 8, October 2004, Pages 777-781

[18] Quanli Hu , Hiroshi Suzuki, Hong Gao, Hiroshi Araki, Wen Yang, Tetsuji Noda "High-frequency FTIR absorption of SiO_2/Si nanowires" Chemical Physics Letters 378 (2003) 299–304

[19] Martin Kopani, Milan Mikula, Daniel Kosnac, Jan Gregus, Emil Pincik "Morphology and FT IR spectra of porous silicon" Journal of ELECTRICAL ENGINEERING, VOL 68 (2017), NO7, 53–57

[20] Junjie Niu , Deren Yang , Jian Sha , Jian Nong Wang , Ming Li "Infrared spectra of silicon nanowires" Materials Letters 61 (2007) 894–896

[21] P.H. Gaskell, D.W. Johnson, J. "The optical constants of quartz, vitreous silica and neutron-irradiated vitreous silica (I)" Non-Cryst. Solids 20 (1976) 171.

[22] C. Aydın, M.S.AbdEl-sadek , KaiboZheng , I.S.Yahia , F.Yakuphanoglu "Synthesis,diffused reflectance and electrical properties of nanocrystalline Fe-doped ZnO via sol–gel calcination technique" Optics & LaserTechnology48(2013)447–452

[23] S. M. Sze, The Physics of Semiconductor Devices, (Wiley, New York, 1969) pp. 12-20.

[24] R.H. Fowler, L. Nordheim, "Electron emission in intense electric fields," Proc. R. Soc. Lond. 119 (1928) 173–181..

[25] D. Banerjee, N.S. Das, K.K. Chattopadhyay, “Enhancement of field emission and hydrophobic properties of silicon nanowires by chemical vapor deposited carbon nanoflakes coating”, Appl. Surf. Sci. 261 (2012) 223–230.

[26] Sumanta Kumar Sahoo and Arumugam Marikani "Morphological Dependence of Field Emission Properties of Silicon Nanowire Arrays" Nano Vol. 11, No. 02, 1650017 (2016).

[27] P.H. Cutler, Jun He, J. Miller, N. M. Miskovsky, B. Weiss and T. E. Sullivan “Theory of electron emission in high fields from atomically sharp emitters: Validity of the Fowler-Nordheim equation” Progress in Surface Science Volume 42, Issues 1–4, January–April 1993, Pages 169-185

[28] U. Ray , D. Banerjee, B. Das, N.S. Das, S. K.Sinha, K. K Chattopadhyay "Aspect Ratio Dependent Cold Cathode Emission from Vertically Aligned Hydrophobic Silicon Nanowires" Materials Research Bulletin Volume 97, January 2018, Pages 232-237

Chapter 6

Study of field emission property of rGO wrapped porous SiNWs

Abstract:

Here, in this chapter, the motivation is to enhance the field emission properties of porous SiNW 80. As it is already established that graphene has several advantages of using 2D nanomaterials in field emission devices due to its different properties like a thickness of only a few atomic layers, high aspect ratio, excellent electrical properties, extraordinary mechanical strength and low cost synthesis. Above all, edges present in graphene enhance the tunneling probability of electrons same as observed in nanotube. Thus, rGO layer is spin casted over porous SiNW 80 to form rGO-SiNW 80 composites. Important basic characterizations like FESEM, RAMAN, FTIR are performed. Experimentally field emission study is carried out which gives enhancement of current density at low applied field in composite compared to bare nanowires. Low turn on and threshold voltage, high current and enhancement factor are observed in rGO-SiNW 80 composite. Theoretical simulation data of ANSYS Maxwell software completely agrees with the experimental result.

6.1 Introduction

Graphene is a 0 eV bandgap semiconductor in which the filled valence band touches the empty conduction band, thus giving rise to peculiar properties [1] that have interesting applications in electronic devices. Graphene and its oxygenated derivatives, including graphene oxide (GO) and reduced graphene oxide (rGO), are becoming an important class of nanomaterials in the field of electronic devices. [2] In addition to individual sheet devices, efforts to obtain graphene-based composites through the reduction of graphene oxide (GO) in solution and incorporation into the nanomaterials has also yielded promising results. [3] There are some advantages of using 2D materials in the field emission display devices i.e. the few atomic layered thickness, high aspect ratio, impressive electrical properties, excellent mechanical strength and low cost synthesis. Apart from this, the existing edges can act as emitting sites for the tunneling probability of electrons.

Incorporation of one dimensional nanostructure with sharp tips on the emitting surface enhances local electric field. [4, 5] By enveloping nanometer scale sharp emitter tips by suitable 2D materials such as graphene, reduced graphene oxide the field emission properties can be further enhanced. [6] These high density protrusions further localize and enhance the electric field, thereby permitting electrons to tunnel through the tips at very low electric fields and to produce stable emission in a large area. In the previous chapter, it is observed that SiNW 80 has some experimental drawbacks for which there is a degradation of field emission properties though high current density is observed at high applied electric field. Thus, in this chapter, the aim is to enhance the field emission properties of that particular nanowire.

To implement the above mentioned criteria, rGO layer is superimposed on sharp tipped nanowires through simple spin casting method. Raman study is performed to ensure the reduction of grapheme oxide. FESEM and FTIR have given constant support to the synthesized materials. As per our desire, field emission property is enhanced impressively. The turn-on fields and enhancement factors of the samples are found using Fowler Nordheim equations. The experiments results are correlated to the theoretical ANSYS MAXWELL simulation data.

6.2 Experimental

6.2.1 Synthesis:

6.2.1.1 Synthesis of Silicon nanowires:

Silicon nanowires are prepared by the method of Metal-Assisted Chemical Etching (MaCE) in a two-step etching process as described in chapter 5 in details. Here the etching is done in oven at **60° C** temperature for time period of **80 minutes**. After etching the Ag particles are removed by HNO_3 and the sample is rinsed with deionised water. During rinsing oxide layer is generated by HNO_3 which is removed by dipping the substrate in HF(5%) solution for 5 minutes again.

6.2.1.2 Preparation of stable dispersion of graphene:

Graphite oxide (GO) suspension in water is synthesized by a modified version of Hummers and Offemans method from graphite powder. [7] [8]

6.2.1.3 Deposition of rGO sheets on SiNW by Spin Coating Method:

At first GO is reduced in hydrothermal at 180°C for 24 hours. Obtained precipitates are collected and rinsed with DI and ethanol for 3 to 4 times. After drying at 60 °C temperature, obtained rGO is spin coated on the silicon nanowires (80 min) by rGO-ethanol diluted solution. The silicon nanowire samples are referred as **SiNW80** and Reduced graphene oxide--Silicon Nanowire composite sample synthesized by spin coating as **rGO-SiNW80.**

6.2.2 Characterizations:

Morphological study of the as prepared sample was carried out by Field emission scanning electron microscope (FESEM, Hitachi, S-4800). Raman spectra was obtained with the excitation of a 532 nm laser source (WITECH).The chemical structure of the synthesized nanochips were analysed by using the Fourier transform infrared (FTIR) spectrometer (Shimadzu).

Field emission studies

The field emission measurement setup is in a high vacuum (2×10^{-6} mbar) chamber. At the time of measurement, a stainless steel electrode with tip diameter (2R) of ~1.5 mm and the sample are treated as cathode and anode respectively keeping 120μm separation between them. Cathode has been connected with 1.3 MΩ resistor.

6.3 Results and Discussion

6.3.1 Morphological analysis by FESEM

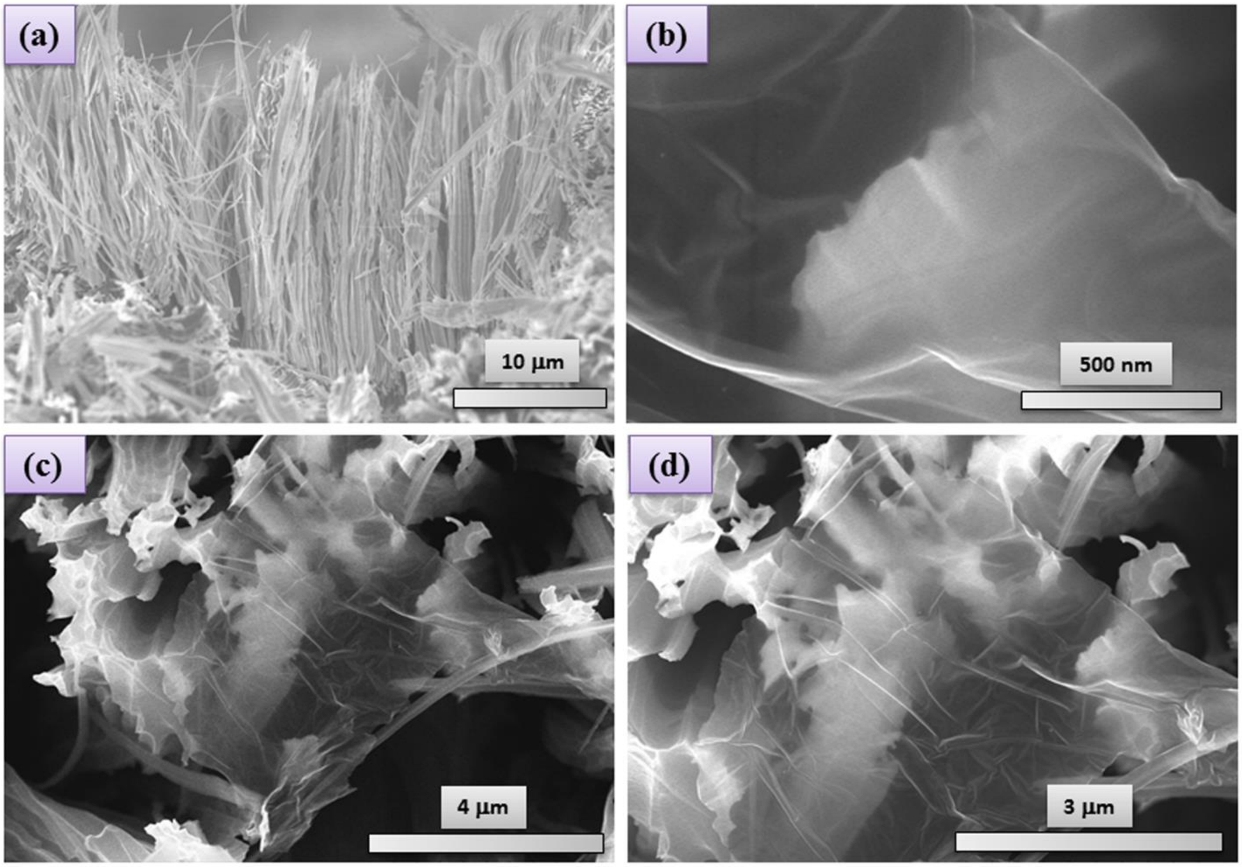

Figure6. 1: (a) Cross-sectional view of SiNW80 (b) Hydrothermally synthesized rGO sheets (c), (d) top view of rGO-SiNW80 composites at different magnification

The FESEM images of the silicon nanowires, hydrothermally synthesized Reduced Graphene Oxide and their spin casted composite is shown in fig 6.1. The cross-sectional view of SiNW80 in fig 6.1(a) shows that silicon nanowires are synthesized uniformly with a length of around 30 µm .In fig 6.1 (b) the image of hydrothermally synthesized rGO is displayed. From the highly magnified image of rGO, the fine sheet like structure of reduced graphene oxide can be seen. In fig 6.1(c) and (d) are the image of the rGO coated SiNWs. It can be clearly seen that the thin sheet like rGO is adhered on the top of the

SiNW 80. The rGO sheets are very thin and highly transparent so the underlying silicon nanowires can be viewed through them. It determines the perfect attachment of rGO with the nanowires which can be effective one for various applications

6.3.2 RAMAN spectroscopy

Raman analysis is carried out for better confirmation of rGO. A Raman peak at 528 cm^{-1} can be seen in the Raman spectrum fig 6.2(a) of which is due to the silicon nanowires. [9] The main features of the GO Raman spectra are the D, G, 2D and D + D´ peak. Raman spectrum shows vibration mode of D-band at 1354 cm^{-1} and G band at 1600 cm^{-1}. The D peak originates from the breathing modes of six-membered rings that are activated by defects and the G peak at 1580–1600 cm^{-1} that is due to the E_{2g} phonon at the Brillouin zone center. The 2D peak at 2700 cm^{-1} is the second order of the D peak and the D + D´ peak at 2940 cm^{-1} is due to the defect activated combination of phonons. [10, 11] The intensity ratio(I_D/I_G) is greater than one signifying the formation of rGO.

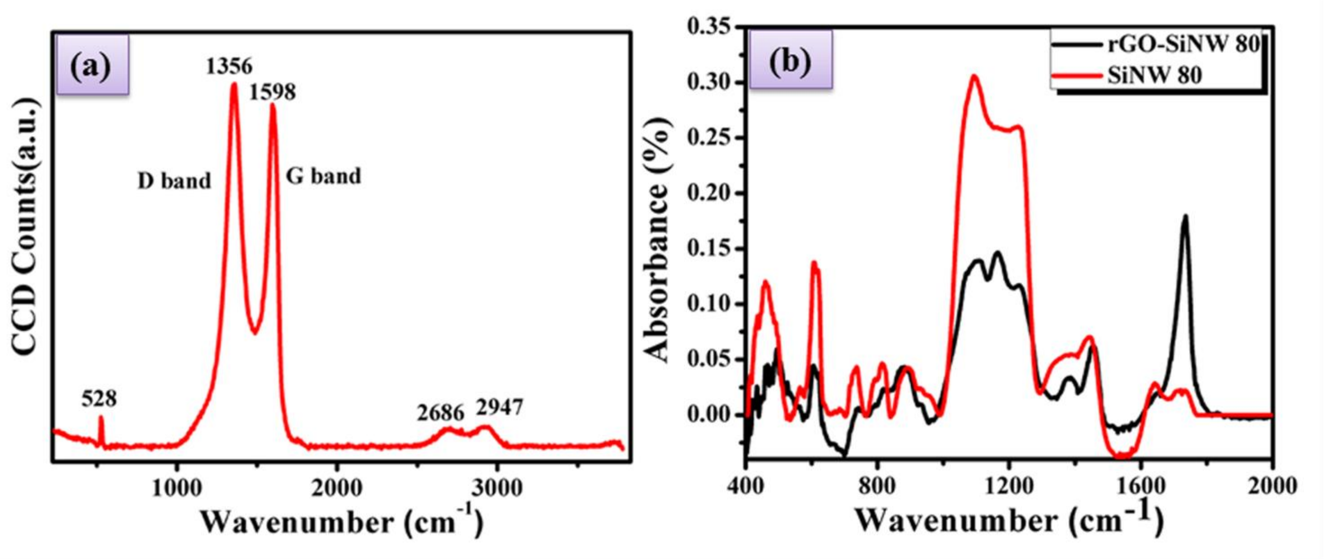

Figure6. 2: (a) Raman Spectra of rGO-SiNW80 composite (b) comparison of FTIR spectra of SiNW 80 with rGO-SiNW 80

6.3.3 FTIR analysis

FTIR spectra of rGO-SiNW 80 are almost consistent with SiNW 80 that signifies the presence of silicon nanowires as observed in fig 6.2(b). Again, there is a presence of characteristic peak at 1735 cm^{-1} which may be attributed to reduction of graphene oxide. This peak is not so prominent for silicon nanowires itself. Apart from this, there is a decrement of absorbance after composite formation. rGO sheet may help to reduce the structural disorder of SiNW 80. Thus, FTIR can be an important property of rGO-SiNW 80 composite.

6.3.4 Field Emission

As discussed in previous chapter, SiNW 80 has given excellent current density at high applied electric field though the turn on and enhancement factor are not improved compared to other nanowires. So, to enhance all the competitive properties of SiNW 80, rGO-SiNW 80 composite is produced by a simple cost-effective method. Now, again, cold cathode emission characteristics are carried out in same laboratory designed high vacuum system at pressure of ~ 10^{-6} mbar. In our experiment a SiNW samples glued to a stainless steel base acts as cathode and a conical shaped stainless steel tip (1.0 mm tip diameter) works as anode. The corresponding current (I) Vs electric field (E) curves are obtained for SiNW80 and rGO-SiNW80 samples. The cold cathode emission current voltage characteristics are analyzed by the classical Fowler Nordheim (F-N) equation [12]:

$$J = A\frac{\beta^2 E^2}{\phi}\exp\left(-\frac{B\,\phi^{3/2}}{\beta E}\right)$$

where $A = 1.54 \times 10^{-6}$ A eV V^{-2} and $B = 6.83 \times 10^{9}$ $eV^{3/2}$ V m^{-2},J is the current density, E is the applied field, φ is the work function of the emitting materials and β is the enhancement factor relating to the following equation:

$$\beta = -\frac{B_{FN}\phi^{\frac{3}{2}}}{s}$$

The experimental J-E curve and corresponding F-N plot are shown in fig 6.3. Here, turn on field is defined at current density of 1 μA/cm^2 which is generated at field of 6.84V/μm for SiNW 80 and 0.12 V/μm for rGO-SiNW 80 as shown in fig 6.3(a). The experimental threshold field of the synthesized SiNW80 and the rGO-SiNW80 composites for 120 μm inter-electrode distances is 10.92 V/μm and 1.2 V/μm (defined as the field required obtaining current density of 10 μA/cm^2). The enhancement factor of SiNW and its rGO composite have been calculated from the slope obtained in F-N plot at fig 6.3(b). The work function for SiNW80 sample is taken as 4.64 eV [13] and for rGO-SiNW80 composite the work function of rGO is considered to be the same as of graphite of 5 eV [14].

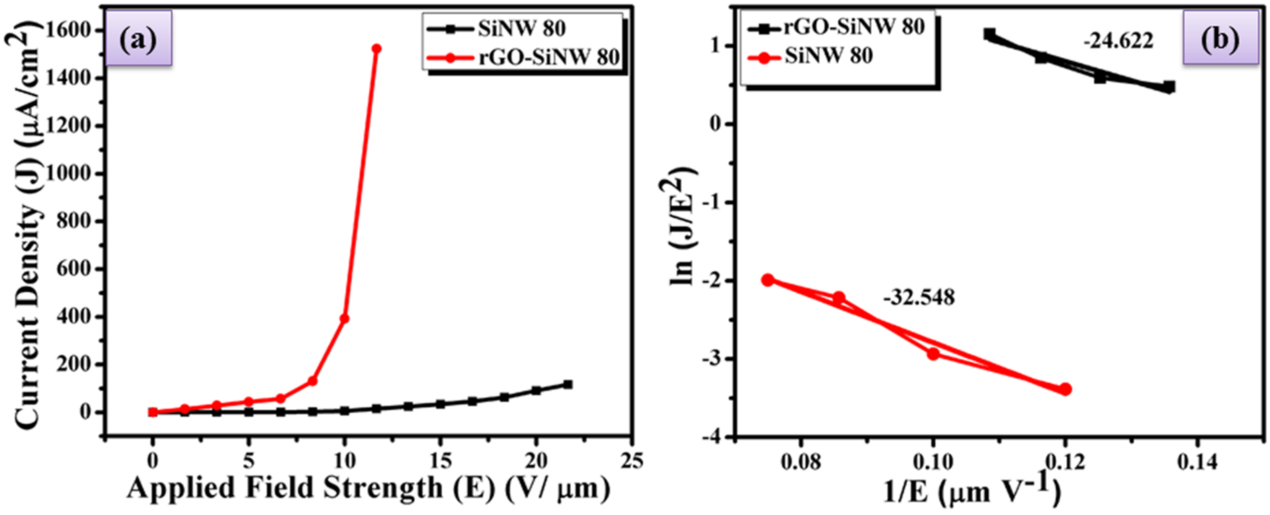

Figure6.3: (a) Current density (J) versus applied field (E) plot of SiNW80 and rGO-SiNW80 at 120 μm inter-electrode distances (b) F-N plot of SiNW80 and rGO-SiNW80

The turn on, threshold fields, enhancement factors and emission current densities (at 5 V/μm) have been given in the following table.

Table I: Comparison of field emission properties

Sample	Turn-on Field at $1\mu A/cm^2$ (V/µm)	Threshold Field at $10\mu A/cm^2$ (V/µm)	Enhancement factor (β)	Emission Current Densities at 5 V/µm (µA/cm2)
SiNW80	6.84	10.92	2098	0.45
rGO-SiNW80	0.12	1.2	3102	43.46

The threshold voltage, turn on field and the enhancement factor are improved for rGO-SiNW80 significantly in comparison with SiNW80. The comparatively low threshold voltage and turn on field, high enhancement factor and current density can be explained mainly due to two reasons. Firstly, the increase in density of the effective emission tips from the rGO edge sites, resulting in better field emission which have been reported previously [15, 14] The second reason is that the sharp peaks of silicon nanowires in bottom layer also contributed partially in providing additional pocket emitter sites in rGO layers by creating unevenness in the thin sheets. Therefore the rGO layers spread over the silicon nanowires helps in minimizing the effect of screening which have been observed for SiNW80 as mentioned in chapter 5.

Field emission simulation and explanation

For 2D simulation of the electric field gradient distribution in SiNWs and rGO-SiNW composite, finite element modelling is employed and the local electric field dispersion is found using ANSYS Maxwell software package as shown in fig 6.4. The simulations have been carried out by considering the following geometrical and material parameterization. For silicon nanowires we have chosen the base diameter of the nanowires as 40nm ending in sharp pointed peaks. We have considered a symmetrical system and the silicon nanowires are equispaced having a separation of ~30nm in between them for convenience. The height of the each SiNW was taken to be ~30μm. For simulation of the composite structure with top rGO sheet assembly a curved sheet of graphite having a thickness of ~2nm is taken. The samples were taken as cathode and a stainless steel anode was considered. A rainbow colour coordinate (red is maximum and blue is minimum) is used to plot the magnitude of the electric field of 2D plane. Here an overall increase in the field can be observed for the rGO-SiNW80 composite which coincides with the experimental results.

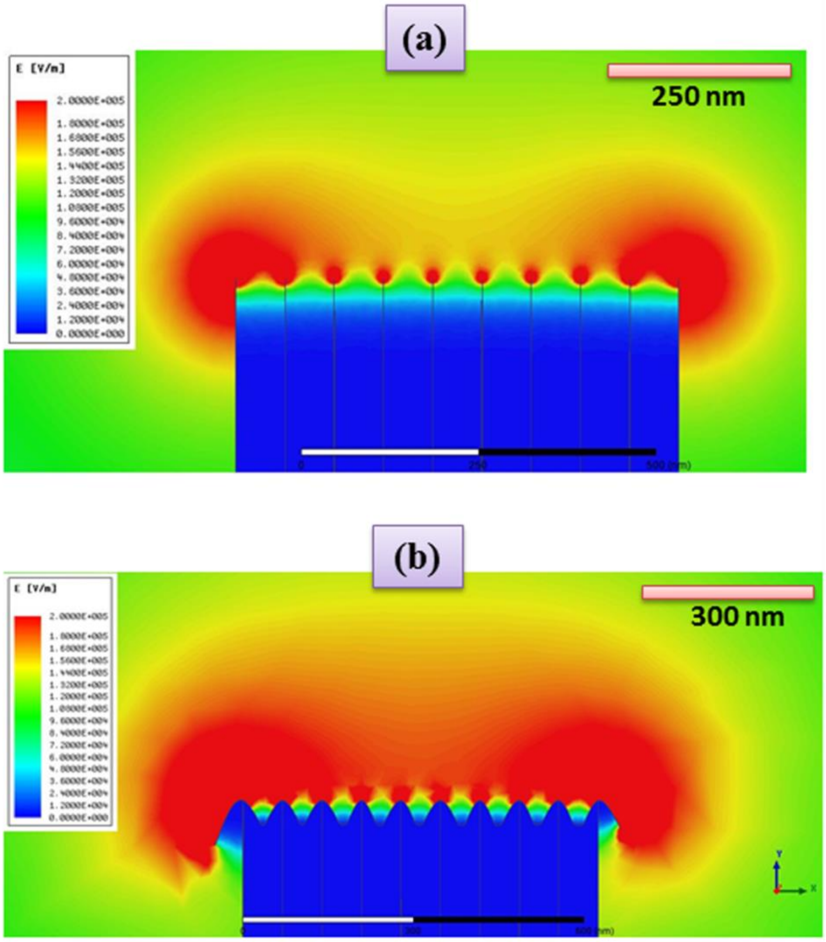

Figure 6.4: Two dimensional representations of the enhancing field vector of (a) SiNW 80 (b) rGO-SiNW 80

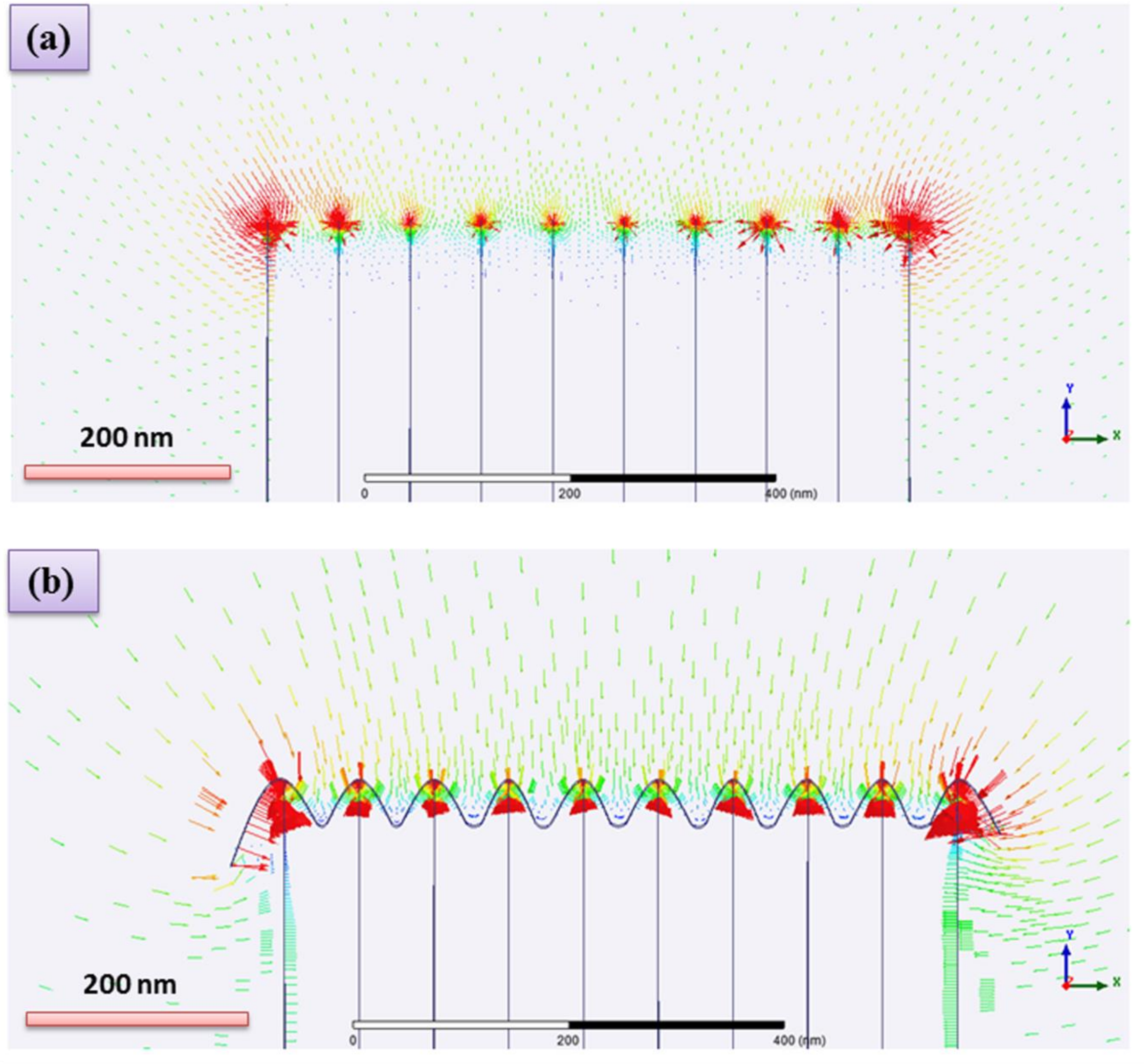

Figure 6.5: Two dimensional representations of the enhancing field of (a) SiNW 80 (b) rGO-SiNW 80

The enhancement of the field after rGO deposition can be nicely demonstrated from the vector images as shown in fig 6.5. It can be clearly noticed that a large amount of increase in the field is due to the emissions of the edge sites from rGO sheets.

6.4 Conclusions:

Thus it can be concluded that rGO –SiNW 80 is synthesized by spin casting method successfully as per the basic characterized obtained data. This composite has acted as best field emitter among all the samples. It is primarily due to the intrinsic properties of the rGO which triggers the emission of electron from long length silicon nanowires. The advantage of both porous nanowire (1D material), sheet (2D material) is extracted here in the field emission application. Both contain extreme aspect ratio which becomes useful here. Apart from porous silicon nanowire sites, rGO also produces emitting edges which enhances the field emission properties like current density, enhancement factors. A significant decrement of turn on and threshold voltage is observed in this composite. Even the theoretically obtained ANSYS Maxwell data completely correlates with experimental results.

References

[1] A. K.Geim, and K. S. Novoselov, , "The rise of graphene.," Nature Mater, vol. 6, p. 183–191, (2007).

[2] Minas M. Stylianakis , George Viskadouros et.al., "Updating the Role of Reduced Graphene Oxide Ink on Field Emission Devices in Synergy with Charge Transfer Materials," Nanomaterials , 9, 137;, (2019).

[3] S.Stankovich, et al., " Graphene-based composite materials.," Nature 442, p. 282–286, (2006).

[4] Shenghan Zhou Ke Chen, Matthew Thomas Cole, Zhenjun Li, Jun Chen, Chi Li and Qing Dai, "Ultrafast Field-Emission Electron Sources Based on Nanomaterials," Adv. Mater,1805845, (2019).

[5] Xiaosheng Fang, Yoshio Bando, Ujjal K. Gautam, Changhui Ye and Dmitri Golberg, "Inorganic semiconductor nanostructures and their field-emission applications," Journal of Materials Chemistry, vol. 18, p. 509–522, (2008).

[6] D. Ye, S. Moussa, J. D. Ferguson, A. A. Baski and M. S. El- Shall,, "Highly efficient electron field emission from graphene oxide sheets supported by nickel nanotip arrays.," Nano Lett., vol. 12, p. 1265–1268., (2012).

[7] W. S. Hummers and R. E. Offeman, " Preparation of Graphitic Oxide," J. Am. Chem. Soc., vol. 80, pp. 1339-1339., 1958.

[8] D. Li, M. B. Muller, S. Gilje, R. B. Kaner and G. G. Wallace, "Processable aqueous dispersions of graphene nanosheets," Nature Nanotechnoly, vol. 3, pp. 101-105, (2008).

[9] M. Ghorbani , H.Abdizadeh , M. R. Golobostanfard, "Reduction of Graphene Oxide via Modified

Hydrothermal Method," Procedia Materials Science , vol. 11 , p. 326 – 330, (2015).

[10] Bibo Li, Dapeng Yu, and Shu-Lin Zhang, "Raman spectral study of silicon nanowires," Physical Review B, Vols. Volume 59, Number 3, (1999).

[11] S. Eigler, C. Dotzer and A. Hirsch,, "Visualization of defect densities in reduced graphene oxide," Carbon, vol. 50, p. 3666–3673, (2012).

[12] L. G. Cançado, A. Jorio, E. H. M. Ferreira, F. Stavale,C. A. Achete, R. B. Capaz, M. V. O. Moutinho,A. Lombardo, T. S. Kulmala and A. C. Ferrari,, "Quantifying Defects in Graphene via Raman Spectroscopy at Different Excitation Energies," Nano Lett., vol. 11, p. 3190–3196, (2011).

[13] R.H. Fowler, L. Nordheim, , "Electron emission in intense electric fields," Proc. R. Soc. Lond.119, p. 173–181., (1928).

[14] D. Banerjee, N.S. Das, K.K. Chattopadhyay,, "Enhancement of field emission and hydrophobic properties of silicon nanowires by chemical vapor deposited carbon nanoflakes coating," Appl. Surf. Sci. 261, p. 223–230, (2012) .

[15] A Jha, R Roy, D Sen and K K.Chattopadhyay, "Curvature aided efficient axial field emission from Carbon nanofiber-Reduced graphene oxide superstructures on Tungsten wire substrate," Applied Surface Science 366,, pp. 448-454, (2016).

[16] R. Roy, A. Jha, D. Banerjee, N.S. Das, K.K. Chattopadhyay,, "Edge effect enhanced electron field emission in top assembled reduced graphene oxide assisted by amorphous CNT-coated carbon cloth substrate," AIP Advances, vol. 3 (1), p. 012115, (2013) .

Chapter 7

Comparative wettability study of SiNW and rGO composite at varying time and temperature

Abstract:

In this chapter silicon nanowires are synthesized by metal assisted chemical etching in room temperature (RT) as well as oven temperature of 60°C. There is a feasible change of wettability is observed like RT synthesized nanowires are hydrophobic in nature but heat synthesized nanowires are hydrophilic initially with some contact angle nearly 90° but within few minutes it spreads out. Both type of CA are explained by two models: Wenzel model and Cassie-Baxter model. They correlate the surface roughness property. In previous chapter already mentioned rGO composite with SiNW_H80's wettability is also measured here and it shows significant improvement of CA to 142°. It again determines how lengthy nanowires with sharp tip affect the DI CA. A thin layer of rGO on the sharp tipped nanowires makes the surface hydrophobic in nature.

7.1 Introduction

Wettability of solid surfaces has attracted many attentions both in research and practical applications in the recent years. Superhydrophobic coatings have found many applications in industry including anti-fog coating, anti-freeze surfaces, oil and water separation, anti-bacterial surfaces, increasing corrosive resistance and medical applications. [1-3] The superwetting properties of solid surface has crucial applications in our daily life as well as engineering fields, such as self-cleaning, digital microfluidic devices, biomedical engineering ,pool boiling and silicon hybrid solar cells.[4-7]

It have been found from previous studies that the wettability and adhesive force of surfaces are determined by their chemical composition[8] and physical structure of the materials.[9,10] As a result, many surfaces materials with adjustable wettability have been fabricated by multiple methods, by introduction of changes in the micro-nanoscale hierarchical structure and chemical modification on the surface of the nanoparticles.[11-13] The control of liquid adhesion by changing the surface energy or surface tension, mainly referring to the superhydrophobic surface in the research, is also realized by similar methods, such as to change the microstructure, and changing the chemical properties by UV irradiation[14] or coating[15] .

In wettability studies, usually the contact angle is one of the most important data showing the amount of the wetting value in a liquid and solid interface. Contact angle greater than 90° represents hydrophilic substances having higher surface energy and greater than 90° represents lower surface energy. Because the wettability of a solid surface is determined by both the chemical component and micro or nanoscale geometrical structure, it could be changed through roughening of the surface or adjustment of the surface energy on a flat surface. [16]

In the present work wettability properties of silicon nanowires synthesized by metal assisted chemical etching is studied. Various parameters during the synthesis process are varied to determine their effect on the contact angle and therefore the wettability properties of the nanowires. Also wettability property of rGO-SiNW is also studied.

7.2 Experimental

7.2.1 Synthesis

The silicon nanowires etched at room temperature are referred to as **SiNW 40 ,SiNW 60 and SiNW 80** for etching time of 40 , 60 and 80 minutes respectively. The silicon nanowires etched in 60° C are referred as **SiNW_H40, SiNW_H60 and SiNW_H80** respectively for the different time of etching. rGO-SiNW_H80 is denoted as composite material.

7.2.2 Characterizations

Contact angle measurements of the sample are done to detect the wettability nature of the samples in the contact angle measurement device (OCA 15EC).

7.3 Results and Discussion

7.3.1 Morphological Analysis by FESEM

In fig 7.1 the FESEM images of SiNWs synthesized with different etching times are shown for heat untreated samples. It can be clearly seen that SiNWs are developed uniformly over the entire field of view, thus the yield is very high. Cross-sectional images show that the average diameters of samples ranges between **140 -220** nm whereas the length of the SiNWs etched for 60 minutes is 2.674µm.

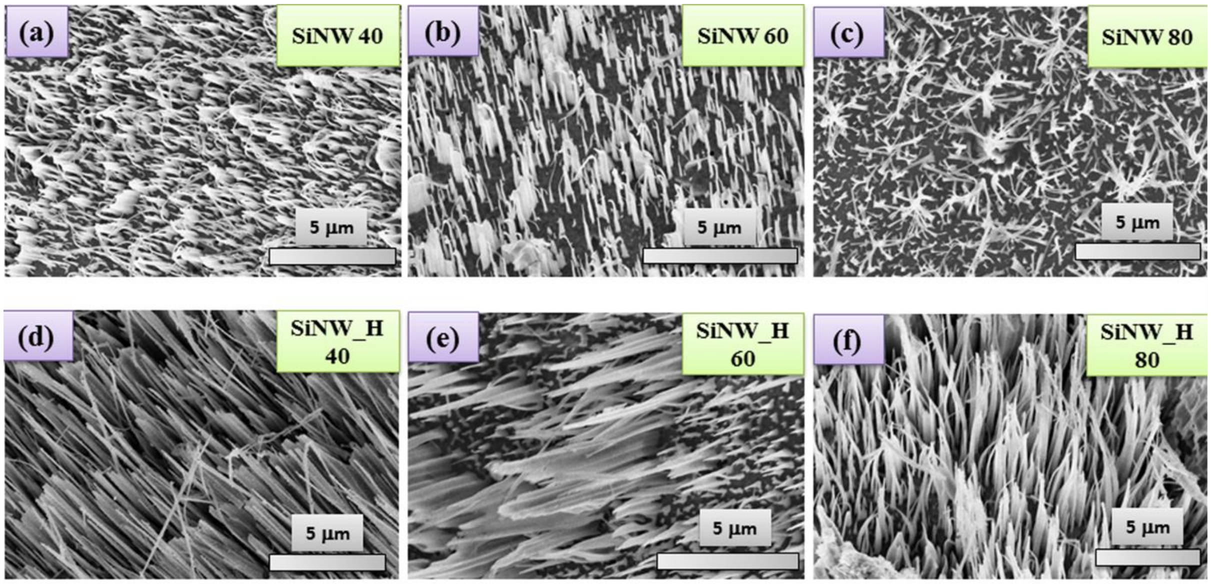

Figure7.1: FESEM images of room temperature synthesized (a), (b), (c) and 60 ^{o}C temperature synthesized (d), (e), (f) silicon nanowires

The fesem images of the heat treated samples are shown in fig 7.1. The diameter of the images of SiNWs varies from **40 nm to 200 nm** with variation of etching time. SiNWs becomes ultrathin with increase of etching and heating time. The length of SiNW_H60 as observed from fig 7.1 (e) is around 30µm respectively. So it is observed that as etching time increases the length of the nanowires increases and diameter decreases in both room temperature conditions and in in 60° C.[18] It can be noticed that the silicon nanowires grows faster and thinner in 60° C compared to their counterparts grown at room temperature with same etching time.

As the etching is performed at 60°C constant environments, there is a faster formation of SiO_2 at the surface of formed nanowire during etching around the Ag nanoparticles and that oxide layer is accordingly etched in different time. As a result there is tendency of formation of ultrathin nanowire with distinct tips. The length of the wire also has been increased significantly due to heat etching which is not seen in room temperature atmosphere. It is also a very important to note that as per previous reports [21] there is a tendency to form bundle at the tip of nanowire as the etching time increases. It is primarily due to dangling bonds and electrostatic charges resulting in mutual interaction between them. In case of heat etching bundling effect is much less which is important to note.

7.3.2 Contact Angle

The water Contact Angle (CA) of room temperature etched SiNW and heat etched SiNW are evaluated to identify whether the surface is hydrophobic, hydrophilic or super-hydrophilic.

The contact angle of the **bulk silicon wafer** is observed to 76.1° having hydrophilic nature as θ is less than 90°.

First, the samples etched **at room temperature** are considered. Fig 7.2 shows that the angle made by droplets of water on the surface of SiNW 40 is 116.85° initially and decreases to 115.63° after stability. This means that contact angle remains quite stable and almost no with time as can be seen from the time vs. CA graph in fig 7.2 where we get almost a straight line. Since contact angle measured is greater than 90°, we can say that the water repellence of the surface increases significantly when SiNWs are formed i.e. the surface becomes hydrophobic in nature.

In case of SiNW 60 contact angle measured is 130.49° initially which decreases to 123.34° after stability in fig 7.2. So in this case also contact angle shows no significant variation with time as can be seen from fig 7.2. Since contact angle measured is greater than 90°, here also we can say that the water repellence of the surface increases significantly and the surface becomes hydrophobic in nature. Moreover contact angle increases remarkably as etching time changes to 60 minutes from 40 minutes.

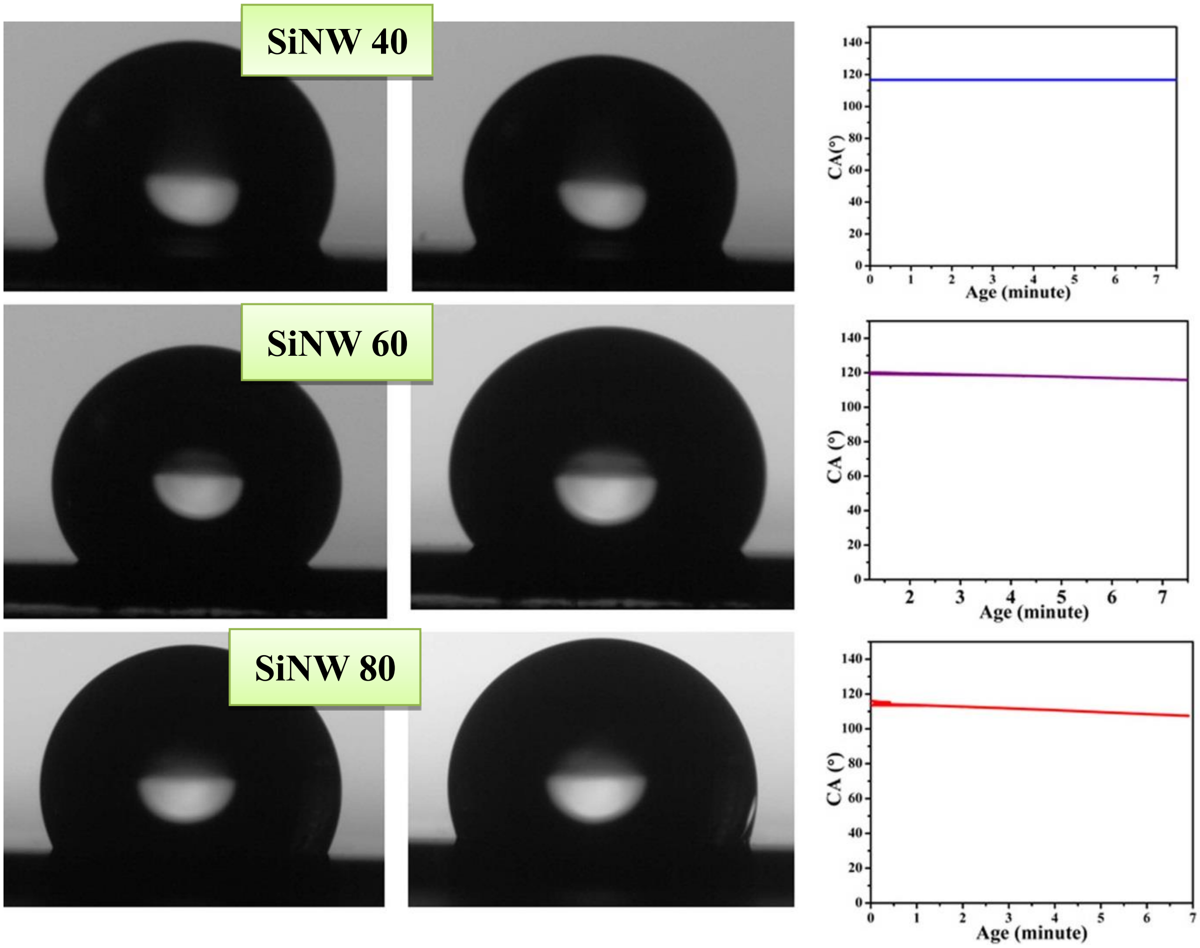

Figure7.2: Contact angles of room temperature synthesized silicon nanowires

From SiNW 80 contact angle measured is 116.21° initially which decreases to 111.29° after few seconds and finally after stability it becomes 100°. Again in this case contact angle varies slightly with time as can be seen from fig 7.2 but the variation is faster than the previous two cases. Since contact angle measured is greater than 90°, here it can be said that the water repellence of the surface is present and is hydrophobic in nature. Contact angle is smaller in case of SiNW 80 than that of SiNW60 and the stability also decreases. This shows that 60 minutes etching time in room temperature is the optimum case for the heat untreated samples and has a stable hydrophobic nature.

Now, the contact angle with droplets of deionized water (DI) of the samples etched at **60°C temperature** is considered. SiNW_H40 minutes is 84.2° initially, decreases to 32.27° after a very few seconds. After a few minutes, when it is stabilized contact angle decreases around to 0°. So in this case contact angle varies rapidly with time as can be seen from fig 7.3 (a). Since contact angle measured is lesser than 90°, here we can say that the surface is still remains hydrophilic in nature after being etched from bulk silicon. Though initially it is greater than bulk silicon but the stable contact angle is 0° which clearly increases the hydrophilic nature after nanowire formation.

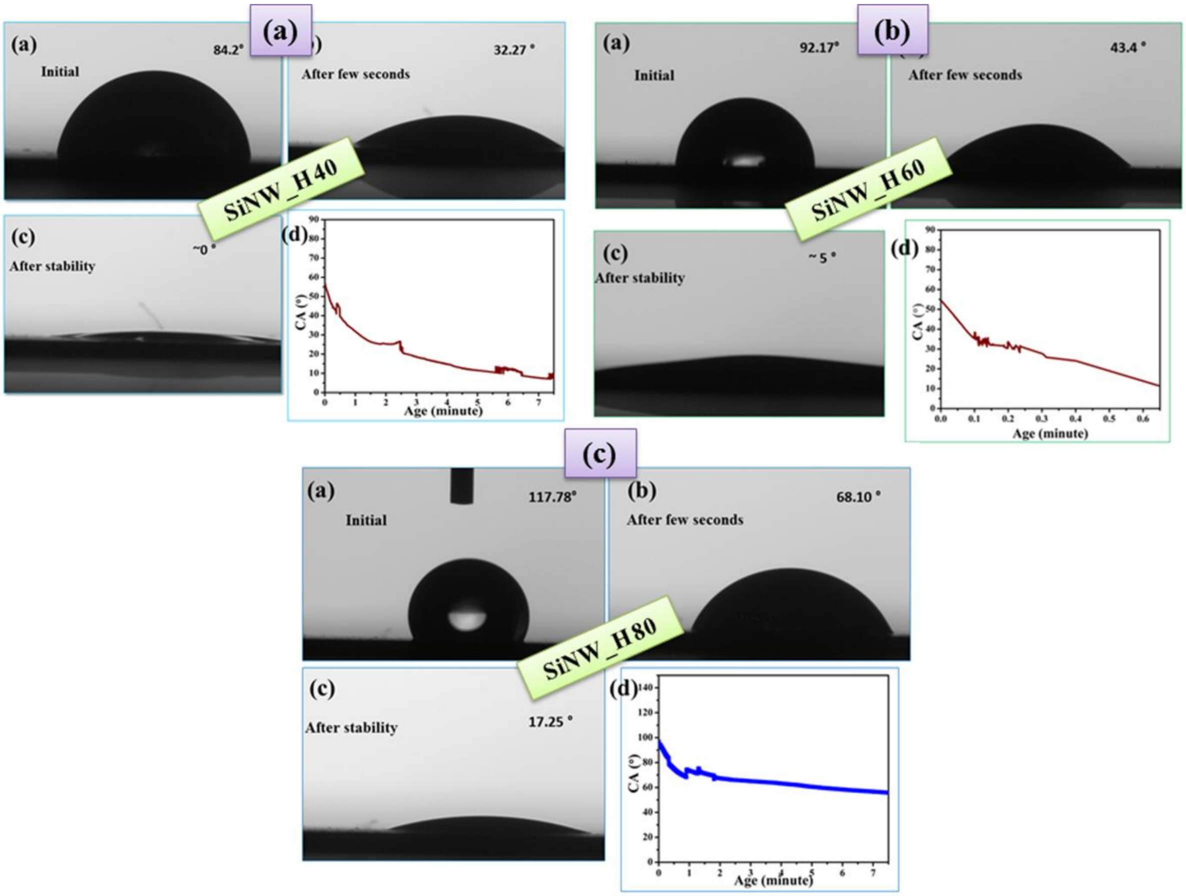

Figure 7.3: Contact angle of 60 ^{0}C synthesized silicon naowires

SiNW_H60 minutes is 92.17° initially, then decreases to 43.4° after a very few seconds. After a few minutes, when it is stabilized contact angle decreases around to 5°. So in this case contact angle varies rapidly with time as can be seen from fig 7.3 (b). Although initial CA measured is very slightly greater than 90°, but it stabilized to 5°, the surface still remaining hydrophilic in nature.

From the fig 7.3 (c), contact angle for SiNW_H80 117.78° initially decreasing to 68.10° in a few minutes, finally stabilising at 17.25°. So in this case CA varies comparatively slower with time as can be seen from fig 7.3 (c). Contact angle measured is greater than 90°, but it stabilized to 17.25° and then dies out within 15 minutes completely. It is observed that as the etching time increases for the heat treated samples, CA increases at the instant when the droplet touches the substrate but eventually it spreads out on the sample substrate resulting in a transition from hydrophobic to hydrophilic nature.

The contact angle of all the cases is summarized in the following table.

Table I: Comparison of contact angle of room temperature and heat synthesized silicon naowires

	SiNW 40	**SiNW 60**	**SiNW 80**	**SiNW_H40**	**SiNW_H60**	**SiNW_H80**
Initial	116.85°	130.49°	116.21°	84.2°	92.17°	117.78°
After few seconds	115.5°	126.55°	111.29°	32.27°	43.4°	68.10°
After stabilisation	115.63°	123.34°	100°	0°	5°	17.25°

Young’s static and dynamic contact angle equations [22] are the most common and relevant parameters describing the wetting property of a surface with respect to liquid water which is valid for homogeneous, molecularly smooth, flat rigid solid surface. Contact angle will strictly be a function of the liquid's surface tension, and the surface's chemistry (surface energy) of the solid. The earliest theoretical model to investigate the behavior of liquid drops on rough surfaces is proposed by Wenzel and Cassie-Baxter.[23,24] While both regimes describe an increase in contact angle with increasing surface roughness, the Cassie–Baxter regime comes into effect when there is a trapped air layer within the roughened or textured surface which causes a substantial increase in contact angle.

According to Wenzel model, When a liquid drop penetrates the asperities of a rough solid substrate and completely wets its area, an expression for apparent equilibrium CA, θ*, as follows:

$$\cos\theta^* = r\cos\theta$$

Where, r is the roughness factor, defined as the ratio of the actual solid-liquid contact area to the flat projected area of the rough solid substrate, and θ is the intrinsic equilibrium CA on a smooth flat surface of the same material. Values of r are always ≥ 1. In Wenzel's model, increasing r makes a hydrophobic surface more hydrophobic and a hydrophilic surface more hydrophilic. In particular, if the roughness of a hydrophilic surface is larger than a critical value given by $r_c = \frac{1}{\cos\theta}$ then the surface becomes superhydrophilic.

The Cassie-Baxter equation provides an expression for the apparent CA, θ^*, as follws:

$$\cos\theta^* = r_f f\cos\theta - (1 - f)$$

Where, r_f (≥ 1) is the roughness factor for the solid-liquid contact area at the top of the rough surface and is analogous the term r discussed in the context of Wenzel state of wetting, f is the ratio of flat projection of solid-liquid contact area, to the total flat geometrical area of the composite substrate under the drop. Thus (1- f) is the ratio of liquid-air interface area, to the total flat geometrical area of the composite substrate under the drop.

Surface roughness is a fact which makes hydrophilic substrate more hydrophilic and hydrophobic surface more hydrophobic according to Wenzel model. As **bulk silicon wafer** is hydrophilic having CA 76.1° the hydrophobic nature of the surface cannot be explained with the Wenzel state for **the room temperature etched samples** (**SiNW 40 , SiNW 60 and SiNW 80**). Cassie Baxter model is valid when the water CA on a smooth surface of the same material is higher than 90°. Here, Cassie Baxter model can be applied as the formation of NW has increased the CA from 76.1° to above 100° which clearly indicates transformation of hydrophilic Si substrate to hydrophobic SiNW. So, it can be assumed that the surface roughness increases in such an extent that decrement of wetting property is observed. Apart from this, there is a visible change of CA with etching time i.e. when the etching time increases from 40 min to 60 min, CA increases from 116.85° to 130.49°. As length increases with etching time, surface area as well as surface roughness increases and surface energy decreases which helps to produce lesser contact between the liquid drop and solid through the base line and air trapped between the wires. It results in increment of CA but for SiNW80 has given lower contact angle for DI drop than SiNW60. This is primarily due to the bundling effect of nanowire. As it has already explained that repeatedly increase of length of porous nanowire for SiNW80 results in congregation of tip due to electrostatic interaction which reduces the surface area, as a whole surface energy increases from SiNW60 and CA decreases. So, it can be concluded that 60 minutes etching is optimum in this process for clearly visible distinct nanowire array. Apart from this, stability of DI droplet on substrate is also observed for 7.5 minutes and it is seen that SiNW40 and SiNW60 are almost stable to its initial angle, the droplet has not spread out. There is slight decrement of angle due to vaporization from droplet surface whereas SiNW80 has a visible change of CA. This is not only vaporization but also there is a slight increment of water adhesion property for SiNW substrate.

Now we consider the case of silicon nanowires **etched in 60° C** (**SiNW_H40, SiNW_H60 and SiNW_H80)**. It is observed that as the etching time increases, CA increases at the instant when the droplet touches the substrate then spreads out on the sample substrate showing a gradual transition from hydrophobic towards hydrophilic nature. This type of activity can also be termed as water adhesive hydrophobic nanowire which is not observed before. SiNW_H40 shows a greater CA than **bulk silicon wafer** (CA is 76.1°) but it still persists its hydrophilicity and spreads out within 7.5 minutes due to its water adhesion property though there is no such oxide layer. As the etching time increase to 60 minutes, initial CA increases to 92.17° which can be termed as hydrophobic but again it shows very high water adhesive property for which within 1-2 minutes droplet dies out completely. At the etching time of 80 minute the substrate acts as hydrophobic one with CA of 117.78° and it takes almost 15 minutes to completely die out i.e. CA~ 0°. As it has already been explained the NWs are significantly longer than room temperature synthesis process and CA are also lower than room temperature synthesis procedure. Above all a significant water adhesion is observed in this oven etched SiNWs which can be explained by surface roughness property as well as length property of SiNWs.

For SiNW 40, substrate’s roughness can be explained by Wenzel model but as the etching time increases and there is a tendency of increase in length of the wire, the roughness is transformed from Wenzel to Cassie Baxter model which clearly shows hydrophobic property. Secondary roughness and spiky morphologies can favour transition of water droplets from the Wenzel to the Cassie-Baxter state as they grow in size[25]. Finally, Wenzel and Cassie-Baxter models are valid only if the drop size is large relative to the size of the roughness features and are easier to define on surfaces with a simple, geometric roughness; however on surfaces with complex, statistical roughness, a mixture of the two models may apply [26].

Now there is a water adhesion property which is very important to mention. There are again several factors but most importantly length of the nanowire which is significantly high and may be larger than critical length. For nanowires grown on either the Si surface, the CA of the nanowire surface initially increases with the nanowire length and decreases after a critical length of the nanowire. This can be explained as the length of NW increases due to heat etching than room temperature etching CA decreases due to longer nanowire. After a critical length, the pining of nanowire becomes effective [27], which draws the water flow downstream and decreases the CA. This is one of the important factors which is responsible to spread out the water on the surface and transforms the surface from hydrophobic to hydrophilic by its water adhesion nature. Surface defects may also play an important role which has to be studied. Even the porosity may play an important role as the no of pores increase as the temperature increase, it may initiates to spread out the water droplet too.

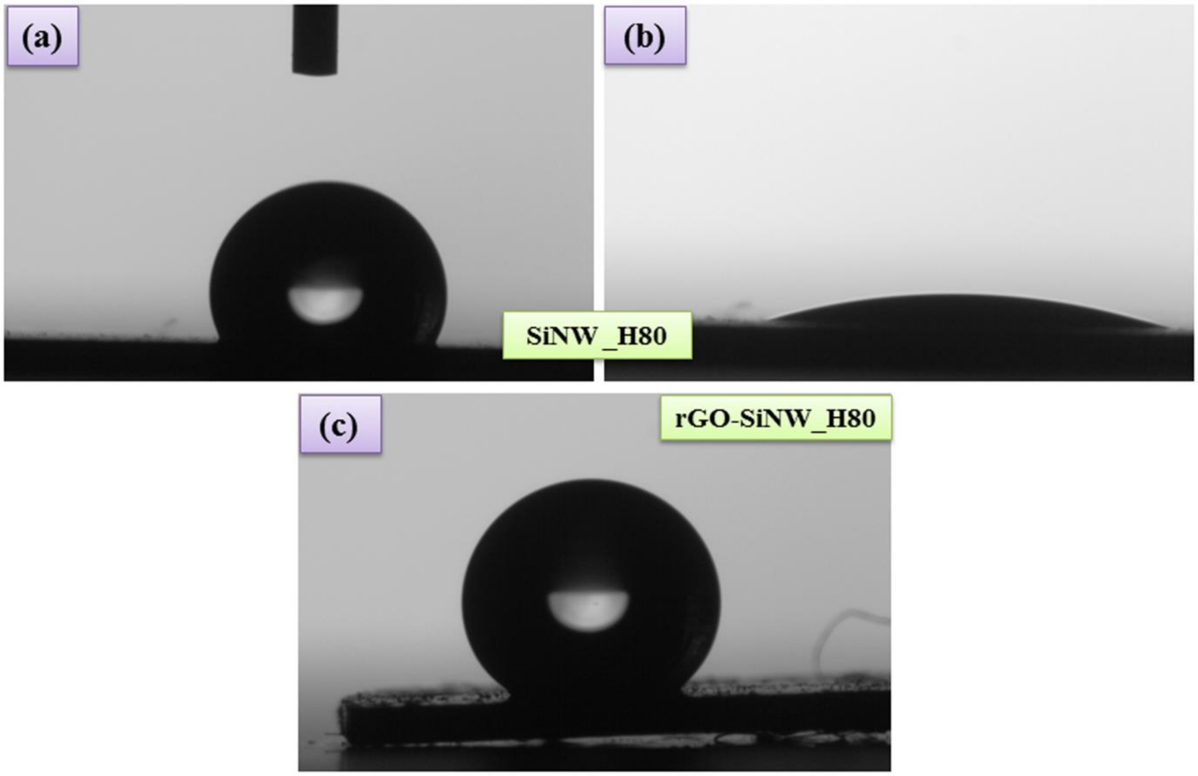

Figure 7.4: Contact angles of room temperature synthesized silicon nanowires

As already mentioned in the previous chapter, rGO layer is spin casted on SiNW_H80. Wettability of that composite is also measured. It is observed that rGO- SiNW_H80 gives contact angle of 142° as displayed in fig 7.4. So, it can be said that there is an increment of contact angle from 117.78° to 142°

and it is more stable than bare SiNW_H80. As the hydrophobicity enhances due to the presence of rGO layer, it can be explained by Cassie-Baxter model. Thus, surface roughness can be one important factor in this case to enhance the hydrophobicity. Apart from this, there is a tendency of water droplet to pinch inside the long nanowire which may initiate to decrease the water contact angle but after deposition of a thin layer of rGO, this tendency diminishes and water droplet tries to round off on the surface of the film. Surface energy of this composite degrades accordingly which may be responsible for such good hydrophobic charateristics.

7.4 Conclusion

It can be concluded that room temperature synthesized silicon nanowires are hydrophobic in nature. It is almost stable for few minutes. When the silicon nanowires are synthesized at 60°C temperature, porosity is observed and there is a decrement of contact angle indicating hydrophilicity. Even the water droplet spreads out within few minutes. It is primarily due to high surface energy, long length of nanowires, presence of pores, tip agglomeration etc. After forming the composite with rGO, the same SiNW_H80 has shown hydrophobicity with contact angle of 142°. Several important factors like surface roughness, thin layer of rGO, low surface energy etc. are responsible.

References:

[1] Bharat Bhushan, Kerstin Kochab and Yong Chae Jung" Nanostructures for superhydrophobicity and low adhesion" Soft Matter, 2008,4, 1799–1804

[2] Qian Xu, Juan Li, Jian Tian, Jie Zhu, and Xuefeng Gao "Energy-Effective Frost-Free Coatings Based on Superhydrophobic Aligned Nanocones" ACS Appl. Mater. Interfaces 2014, 6, 12, 8976-8980

[3] Eric J.Faldea, Stefan T.Yohea, Yolonda L.Colson, Mark W.Grinstaff "Superhydrophobic materials for biomedical applications" Biomaterials Volume 104, October 2016, Pages 87-103

[4] Gh. Barati Darband , M. Aliofkhazraei , S. Khorsand , S. Sokhanvar , A.Kaboli "Science and Engineering of Superhydrophobic Surfaces: Review of Corrosion Resistance, Chemical and Mechanical Stability" Arabian Journal of Chemistry

[5] B. Xin, J. Hao, “Reversibly switchable wettability.” Chem. Soc. Rev. 39(2), 769–782 (2010).

[6] J. Drelich, E. Chibowski, D.D. Meng, K. Terpilowski, “Hydrophilic and superhydrophilic surfaces and materials.” Soft Matter 7(21), 9804–9828 (2011)..

[7] Y. Zhang, W. Cui, Y. Zhu, F. Zu, L. Liao, S.T. Lee, B. Sun, “High efficiency hybrid PEDOT:PSS/nanostructured silicon Schottky junction solar cells by doping-free rear contact.” Energ. Environ. Sci. 8(1), 297–302 (2015).

[8] Y. Coffinier, G. Piret, M.R. Das, R. Boukherroub, “Effect of surface roughness and chemical composition on the wetting properties of silicon-based substrates.” C. R. Chim. 16(1), 65–72 (2013).

[9] Y. Lai, F. Pan, C. Xu, H. Fuchs, L. Chi, “In situ surface-modification- induced superhydrophobic patterns with reversible wettability and adhesion.” Adv. Mater. 25(12), 1682–1868 (2013).

[10] T. Darmanin, F. Guittard, Wettability of conducting polymers: from superhydrophilicity to superoleophobicity. Prog. Polym.Sci. 39(4), 656–682 (2014)

[11] Y T. Lv, Z. Cheng, D. Zhang, E. Zhang, Q. Zhao, Y. Liu and L. Jiang, “Superhydrophobic surface with shape memory micro/nanostructure and its application in rewritable chip for droplet storage” ACS Nano, 2016, 2016, 10, 9379.

[12] J. Fang, A. Kelarakis, L. Estevez, Y. Wang, R. Rodriguez and E.P. Giannelis, “Superhydrophilic and solvent resistant coatings on polypropylene fabrics by a simple deposition process” J. Mater. Chem., 2010, **20**, 1651

[13] R. B. Pernites, R. R. Ponnapati and R. C. Advincula, “Superhydrophobic–superoleophilic polythiophene films with tunable wetting and electrochromism” Adv.Mater., 2011, 23, 3207-3213

[14] K. Uchida, N. Nishikawa, N. Izumi, S. Yamazoe, H. Mayama, Y.Kojima, S. Yokojima, S. Nakamura, K. Tsujii and M. Irie, Angew. “Phototunable diarylethene microcrystalline surfaces: lotus and petal effects upon wetting Chem.”, Int. Ed., 2010, 49, 5942-5944.

[15] Y. Lai, C. Lin, J. Huang, H. Zhuang, L. Sun and T. Nguyen, “Markedly Controllable Adhesion of Superhydrophobic Spongelike Nanostructure TiO2 Films” Langmuir, 2008, 24, 3867-3873.

[16] Liang Zhu, Yanying Feng ∗, Xiongying Ye, Zhaoying Zhou “Tuning wettability and getting superhydrophobic surface by controlling surface roughness with well-designed microstructures”Sensors and Actuators A 130–131 (2006) 595–600

[17] Xiangman Meng, Ailin Zhou, Bo Wang . Yu Chen, Yun-Hui Tang, Hui Yan "Stable Superwetting Surface Prepared with Tilted Silicon Nanowires" Nano-Micro Lett. (2016)

[18] Sanjay K Srivastava, Dinesh Kumar, S W Schmitt, K N Sood, S H Christiansen and P K Singh "Large area fabrication of vertical silicon nanowire arrays by silver-assisted single-step chemical etching and their formation kinetics" Nanotechnology 25(17):175601 (2014)

[19] Z. Huang, N. Geyer, P. Werner, J. De Boor, and U. G¨osele,“Metal-assisted chemical etching of silicon: a review,” Advanced Materials, vol. 23, no. 2, pp. 285–308, (2011).

[20] K. Peng, A. Lu, R. Zhang, and S. T. Lee, “Motility of metal nanoparticles in silicon and induced anisotropic silicon etching,” Advanced Functional Materials, vol. 18, no. 19, pp. 3026–3035, 2008.304

[21] Stefan Weidemann, Maximilian Kockert, Dirk Wallacher, Manfred Ramsteiner, Anna Mogilatenko, Klaus Rademann, and Saskia F. Fischer "Controlled Pore Formation on Mesoporous Single Crystalline Silicon Nanowires: Threshold and Mechanisms" Journal of Nanomaterials Volume 2015, Article ID 672305,

[22] Young T 1805 Phil. Trans. 95 84; Works, edit by Peacock,1, 432

[23] A. B. D. Cassie and S. Baxter " Wettability of porous surfaces" Transactions of the Faraday Society Volume 40, 1944

[24] Robert N. Wenzel "Resistance of Solid Surfaces To Wetting By Water "Ind. Eng. Chem., 1936, 28 (8), pp 988–994

[25] C. Dorrer and J. Ruhe, " Some thoughts on superhydrophobic wetting " Soft Matter, 2009, 5, 51–61.

[26] A Egatz-Gomez, R Majithia, C Levert, KE Meissner. " Super-wetting, wafer-sized silicon nanowire surfaces with hierarchical roughness and low defects" Rsc Advances 2 (30), (2012) 11472-11480

[27] Cheng Yung Kuo and Chie Gau "Control of Superhydrophilicity and Superhydrophobicity of a Superwetting Silicon Nanowire Surface " J. Electrochem. Soc. (2010) volume 157, issue 9, K201-K205

Chapter8

Grand Conclusion

&Future Scope

8.1 Conclusions:

The whole work indicates toward good field emission property of porous silicon nanowires and its composite with rGO. Here, SiNW is synthesized at 60° C temperature. Important basic characterizations are carried out. As the etching time increases, the length of the nanowire increases and diameter decreases. Thus, SiNW 80 gives highest current density at high applied potential though the other properties like turn on field, threshold voltage or enhancement factors are not improved. In that case, SiNW 60 is the optimum one for good field emitter property. To enhance all field emission properties of SiNW 80, rGO layer is put on the SiNW 80 to make the rGO-SiNW 80 composite. As per expectation, there is a high enhancement of current density with low turn on and threshold voltage with high enhancement factor. There are many factors which may be responsible like surface roughness, enhancement of emitting edges, porosity etc. for such enhancement. Theoretical ANSYS Maxwell simulation is performed which completely agrees with experimental results. Wettability properties are measured for all the samples which correlate with the field emission characteristics. As it is observed that CA increases in rGO-SiNW_H80 composite, there is increment of surface roughness which initiates to have more emitting edges for good field emission property. Heat treated porous nanowires' wettability is compared with room temperature synthesized nanowires. There is a significant transformation from hydrophobic (room temp) to hydrophilic (heat treated). Porosity, length, sharp tip, bundling effect etc. are important factor for such changes in properties.

8.2 Future Scope:

In future hydrophobicity of silicon nanowires can be enhanced by several surface coatings. Some works are going on right now to enhance the properties of silicon nanowire. On p type silicon nanowires, n type CdS is deposited by chemical bath deposition. Several characteristics are performed. In future, these materials can be used as p-n junction. More study is needed to conclude anything.

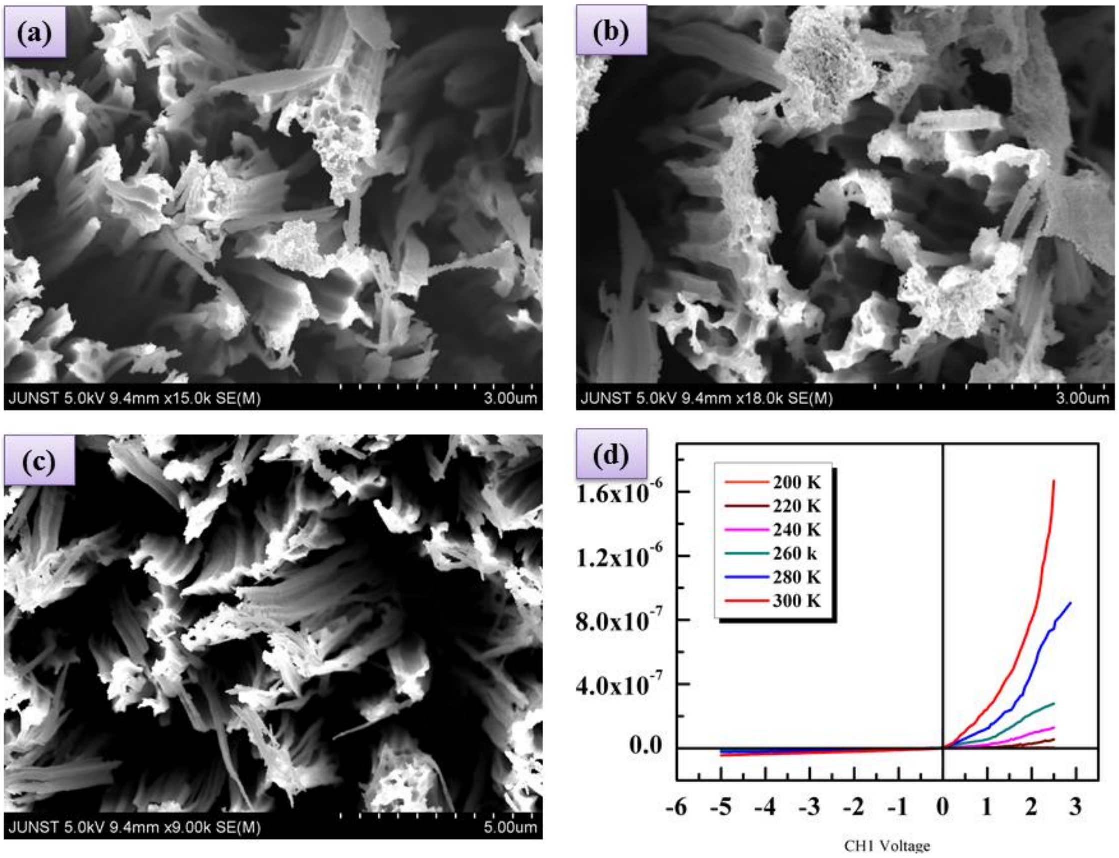

Figure : FESEM of (a)CdS-SiNW (10 min) (b) CdS-SiNW (20 min) (c) CdS-SiNW (30 min) (d) I-V property of CdS-SiNW (30 min)